UCRL-ID-122300

# Second Progress Report on Pre-Test Calculations for the Large Block Test

Kenrick H. Lee

November 15, 1995

## Abstract

The U.S. Department of Energy's (DOE) Yucca Mountain Site Characterization Project (YMP) is investigating the suitability of the Topopah Spring tuff in the thick vadose zone at Yucca Mountain, Nevada, as a host rock for permanent disposal of high-level radioactive waste. As part of the YMP, a group of field tests, called the Large Block Test (LBT), will be conducted on a large electrically heated block of Topopah Spring tuff, isolated at Fran Ridge, Nevada Test Site. The block, which will be $3 \times 3$ m in horizontal dimensions and about 4.4 m high, will be heated by electrical heaters installed in five boreholes drilled in a horizontal plane 2.75 m below the top of the block. The goals of the LBT are to gain information on the coupled thermal-mechanical-hydrological-chemical processes that will be active in the near-field environment of a repository; to provide field data for testing and calibrating models; and to help in the development of measurement systems and techniques. In this second progress report, we present results of the final set of numerical modeling calculations performed in support of the LBT design. We use a three-dimensional conduction-only model to study the thermal behavior of the system. The results include block temperatures and heat fluxes across the surfaces. The results are applied primarily to the design of guard heaters to enforce adiabatic conditions along the block walls. Conduction-only runs are adequate to estimate the thermal behavior of the system, because earlier calculations showed that heat transfer in the block is expected to be dominated by conduction. In addition, conduction-only runs can be made at substantially shorter execution times than full hydrothermal runs. We also run a two-dimensional, hydrothermal, discrete fracture model, with 200-$\mu$m vertical fractures parallel to the heaters and occurring at a uniform spacing of 30 cm. The results show the development of distinct dryout and recondensation zones. The dryout zones are thickest at the fractures and thinnest in the matrix midway between the fractures. Block temperatures are unaffected by the location of the fractures.

# 1. Introduction

The U.S. Department of Energy's (DOE) Yucca Mountain Site Characterization Project (YMP) is investigating the suitability of the Topopah Spring tuff in the thick vadose zone at Yucca Mountain, Nevada, as a host rock for permanent disposal of high-level radioactive waste. Because heat-driven fluxes of liquid water and water vapor in the near-field repository environment will affect waste package deterioration rates and the transport of radionuclides away from the packages, scientists at Lawrence Livermore National Laboratory (LLNL) and elsewhere are studying this hydrothermal flow behavior. The studies include numerical modeling (Buscheck and Nitao, 1993a, 1993b), and field and laboratory testing (Ramirez *et al.*, 1991; Lin and Daily, 1989).

Heat generated in the radioactive decay of the waste is expected to drive coupled thermal-mechanical-hydrological-chemical (TMHC) processes in the near-field repository environment. A group of field tests to be conducted on a large electrically heated block of Topopah Spring tuff, isolated at Fran Ridge, Nevada Test Site, will be used to gain information on these processes. The tests, collectively referred to as the Large Block Test (LBT), are described by Lin et al. (1994a). The LBT will also provide data for testing and calibration of models and will help in the development and evaluation of measurement systems and techniques.

This is the second progress report presenting results of ongoing numerical modeling calculations we are conducting in support of the LBT design. The first report presented some preliminary hydrothermal calculations (Lee, 1995) using the VTOUGH code developed by Nitao (1989). In this report, we use a fully three-dimensional conduction-only model to examine the thermal response of the block to heating. We also conduct a two-dimensional, hydrothermal, discrete-fracture analysis to investigate the effects of fractures on the behavior of the system. All calculations for this report were conducted using the NUFT code (Nitao, 1993). Results of the conduction-only calculations were applied primarily to the design of guard heaters that will be used to enforce adiabatic conditions along the walls of the block. Conduction-only runs are adequate for estimating the general thermal behavior of the system, because earlier calculations showed that heat transfer in the block is expected to be dominated by conduction

(Lee, 1995). In addition, conduction-only runs require substantially lower execution times than full hydrothermal runs.

The general design of the block is outlined in Sec. 2. The conduction-only model is described and the results presented in Sec. 3. A model description and results are presented for the hydrothermal discrete-fracture model in Sec. 4.

# 2. Description of the Block

A schematic of the block is shown in Fig. 1. The shaded area represents the quarter-symmetry section modeled in the conduction-only analysis. A more detailed description of the block is given by Lin et al. (1994a, 1994b). The rock surrounding the block was excavated by mechanical excavation and cutting using a rock saw. The isolated block has four vertical free faces and a horizontal upper surface. Each face has a number of layers of insulation and other materials that include the guard heater assembly. These layers are modeled as shown in Fig. 2. The floor surrounding the block is surfaced with a 15-cm-thick layer of concrete overlaying a layer of gravel, also 15 cm thick. The horizontal block dimensions are $3 \times 3$ m and the height is 4.4 m. The base of the block remains attached to the underlying rock. Five parallel heater emplacement boreholes were drilled horizontally into one block face, normal to the face, in a plane 2.75 m below the top of the block. These borehole axes are oriented in an east-west (EW) direction. The boreholes extend to a distance of 30 cm short of the opposite face, giving a borehole length of 2.70 m. The spacing between the boreholes is 60 cm, and the distance of each end borehole from the neighboring vertical wall is 30 cm. Each borehole will house a rod-type electrical heater capable of delivering at least 400 W, giving a minimum power capacity of 2000 W for the five boreholes. The first 30 cm of each borehole will not be heated, and is assumed to be plugged with rock core for these calculations. Heat will be delivered uniformly along the 2.4-m heated length. A number of additional boreholes will carry instrumentation to monitor the hydrothermal, mechanical, and chemical response of the block to thermal loading.

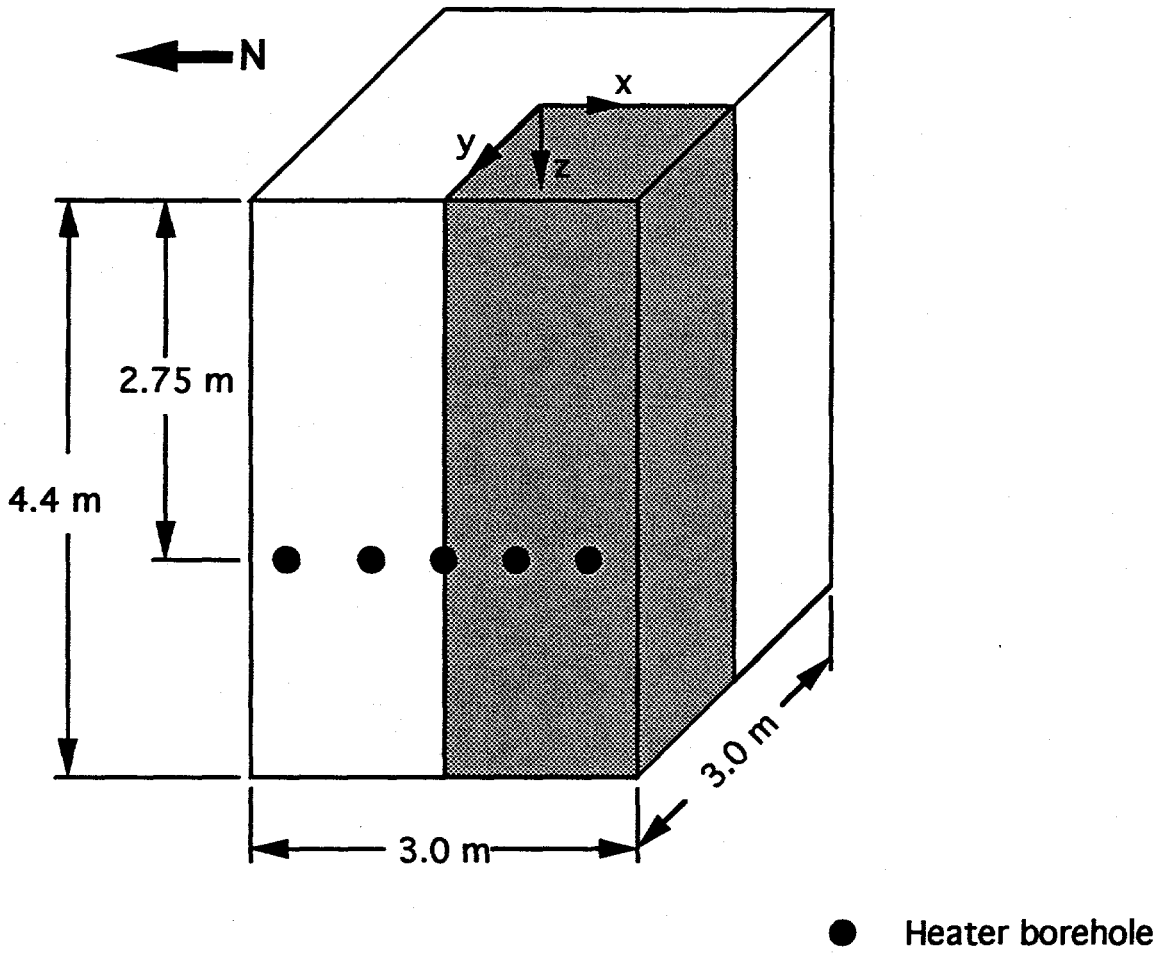


Figure 1. Schematic of Large Block. Shaded area represents quarter-symmetry section modeled in conduction-only analysis.

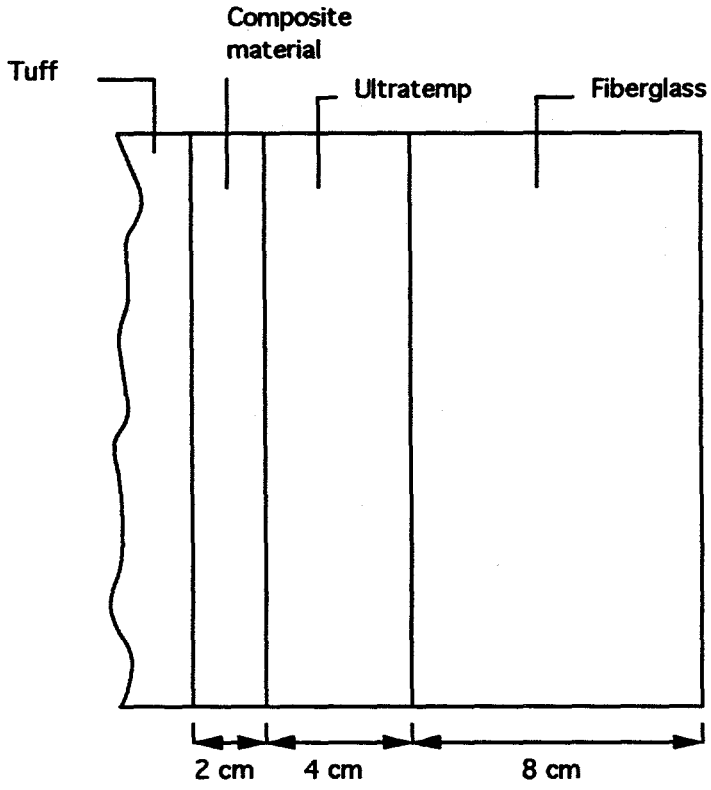


Figure 2. Insulating materials used on walls of Large Block. The composite material is made up of layers of RTV, Viton, fiberglass, and aluminum.

# 3. Three-Dimensional Conduction-only Runs

We used the NUFT code (Nitao, 1993) to conduct two three-dimensional conduction-only runs. In the first run, the block was heated without guard heaters on the walls, allowing some heat loss through the insulation. In the second run, the guard heaters were assumed to be in place, giving adiabatic conditions along the walls.

These runs provided insight into the thermal behavior of the system, at substantially shorter execution times than with runs that include fluid movement. Fluid movement by advection and diffusion were switched off to increase computational efficiency.

One of the primary purposes of these conduction-only runs was to aid in the design of the guard heaters used to enforce adiabatic vertical block faces. Potentially critical heat loss areas were identified so that guard heater plate dimensions and heat-flux sensing locations could be appropriately selected.

## 3.1. Grid Design and Input Data

A quarter-symmetry section, shown in Fig. 1, was modeled. We assume that heat is delivered uniformly along the length of each heater, and that the heater powers in the five boreholes are identical. The three heater boreholes in the symmetry model are powered to 1/4, 1/2, and 1/2 of full borehole power, respectively.

The grid is designed to give higher resolution close to and above the heater horizon and lower resolution at greater distances beneath the heaters. Fig. 3 shows the grid design for x-z planes in and near the block. Larger grid sizes at greater depths beneath the block and at greater distances to the right are not shown. Block sizes in the y-direction are similar to those in the x-direction. The modeled domain down to the base of the block is $20 \times 15 \times 31$ nodes in the x, y, and z directions, respectively. Below the base, the domain is $32 \times 26 \times 17$ nodes. Null blocks fill the voids above the level of the base. Mesh size varies from 2 cm in the heater horizon and within the insulators to 10 m close to the lower boundary. The depth of the model is 33 m.

The block is heated at a constant heater borehole temperature of 140°C. The temperature at the upper surface is fixed at 60°C. The temperature of

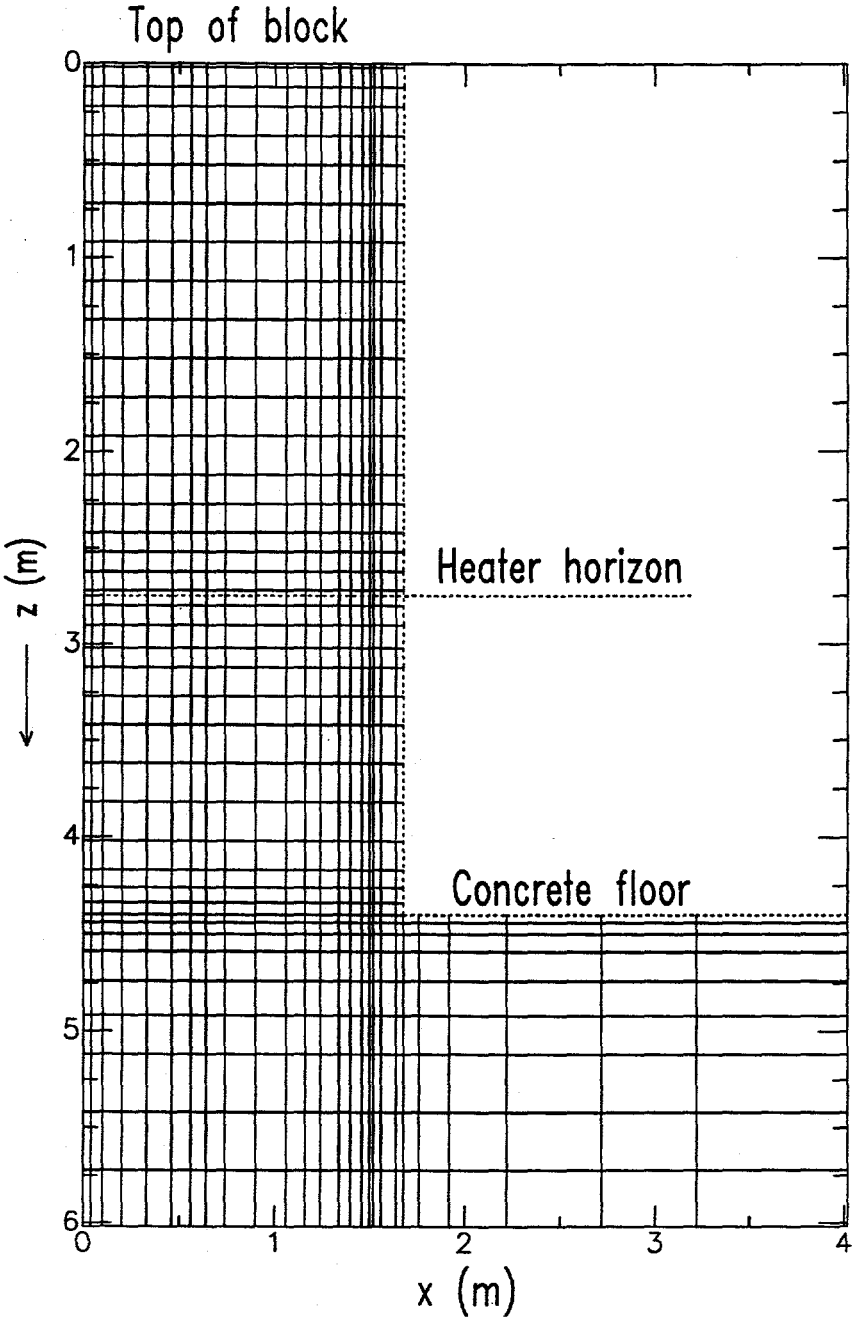


Figure 3. Grid design for x-z planes in and near the Large Block. Grid sizes in the y-direction are similar to those in the x-direction.

Table 1. Primary thermal properties of materials.

| Material | Thermal conductivity (W/m K) | Bulk density ($kg/m^3$) | Specific heat (J/kg K) |
|---|---|---|---|
| Tuff | 2.1 | 2580 | 840 |
| Ultratemp | 0.093 | 560 | 1130 |
| Fiberglass | 0.042 | 25 | 700 |
| Composite | 0.125 | 1064 | 1190 |
| Concrete | 1.70 | 2580 | 900 |
| Gravel | 1.80 | 2580 | 900 |

60°C was selected to give a realistic temperature gradient above the heater horizon. This upper boundary condition permits heat flow through the top of the block. The vertical symmetry planes are modeled as adiabatic boundaries. The insulated walls are bounded by an atmosphere layer, held at a temperature of 20°C. The lower boundary, and the right boundary below the block base, are assigned a very high specific heat, so that rock temperatures are held constant at these boundaries. All runs are made from an initial temperature of 20°C and an initial liquid saturation of 0.5.

The primary thermal parameters used are listed in Table 1. Thermal properties of the rock were obtained from the YMP Reference Information Base (1990). Thermal properties of the other materials were obtained from Lienhard (1987).

## 3.2. Heating without Guard Heaters

We first address the case where no guard heaters are used on the walls, so that the wall insulation is the only means of reducing heat loss through the walls. Fig. 4 shows heat loss fluxes across a horizontal line in the heater horizon on the walls. The fluxes shown are normal to the wall. Recall that x and y are zero along a vertical axis through the center of the block; x

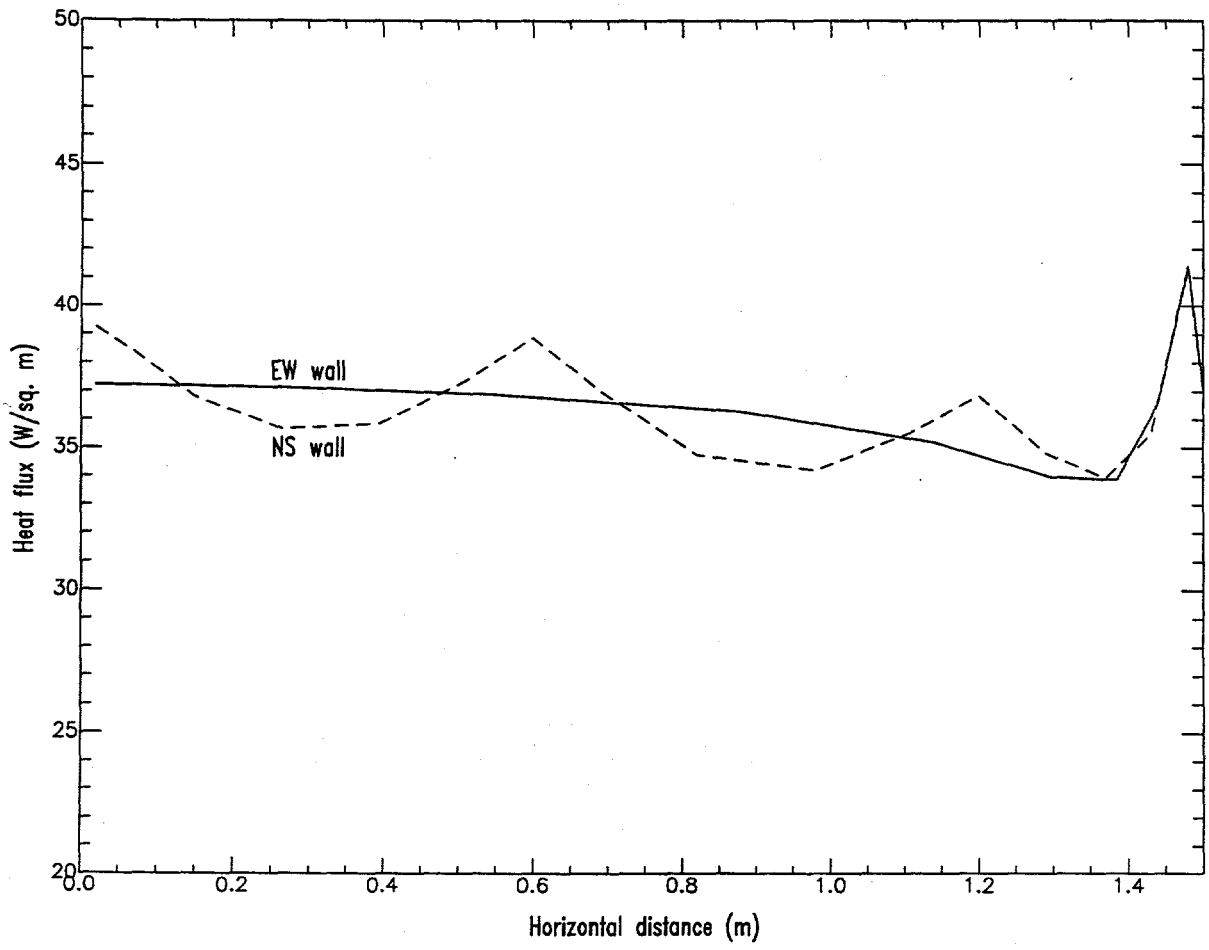


Figure 4. Heat loss fluxes through block walls, shown along horizontal lines on east-west (EW) and north-south (NS) walls in heater horizon.

is positive to the south and y positive to the west; z is zero at the top of the block and positive downward. Because the EW line runs parallel to the heaters, the fluxes along this line are more uniform, averaging about 37 $W/m^2$. There is a small drop approaching the end of the heater, and then a rise due to corner effects close to the edge of the block. Fluxes along the NS line are less uniform, averaging about the same 37 $W/m^2$, but displaying highs at the heater locations and lows midway between heaters. For both walls, the flux drops off gently going from the center toward the edge.

Fig. 5 shows heat loss fluxes across vertical lines down the EW and NS walls. The losses peak in the heater horizon, at about 37 $W/m^2$, as shown in Fig. 4. There is no substantial difference in heat loss patterns between the EW and NS walls. In addition, heat losses along vertical lines do not vary significantly with distance from the center of the wall, provided the location is more than 20 cm or so from the edge.

Fig. 6 shows heat loss fluxes along EW and NS lines along the top surface of the block. Heat losses drop off substantially going from the center to the edges of the top surface. Peak losses are about 27 $W/m^2$ at the center. The negative sign indicates that heat flow is in the negative z-direction (upward). The figure shows some heat flow into the block through the top, close to the corners. This inward flux is due to the 60°C top boundary temperature and the neighboring 20°C side boundary temperature. A negative temperature gradient is established from the top into the block in the vicinity of the corners, causing some heat movement into the block.

An analysis of the power input and losses through the various free faces highlights the need for guard heaters. With the top surface of the block held at 60°C, and the atmosphere outside the vertical insulated faces at 20°C, a steady-state heating power of 2100 W is required to maintain a heater borehole temperature of 140°C. This uniform heater temperature was achieved computationally by stating the heater borehole temperatures as a boundary condition. Integration of the heat fluxes through the free faces shows 1240 W, or 59% of the power input, lost through the insulated vertical faces. Losses through the top surface totaled 160 W, and 300 W was lost through the concrete floor, out to a distance of about 3 m.

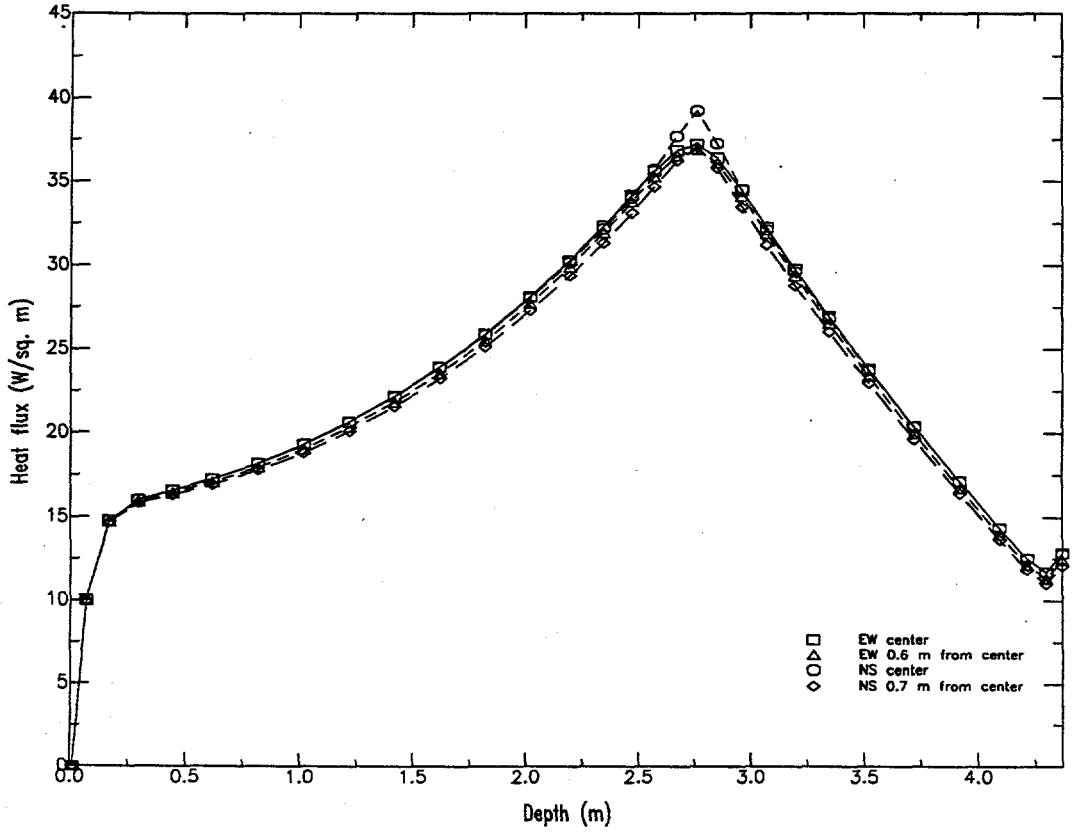


Figure 5. Heat loss through block walls, shown along vertical lines down east-west (EW) and north-south (NS) walls.

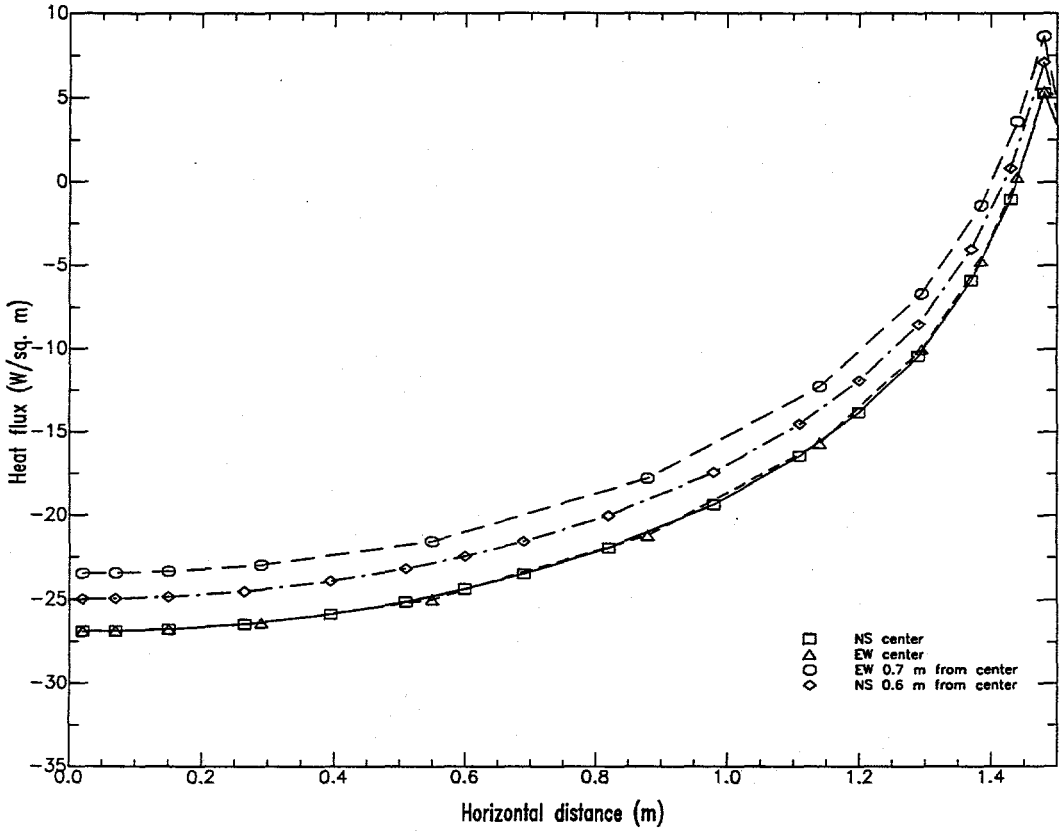


Figure 6. Heat loss through top of block, using imperfect insulators and no guard heaters. Fluxes shown along east-west (EW) and north-south (NS) lines. Negative and positive fluxes here imply heat flow out of and into the block, respectively.

### 3.3. Heating with Guard Heaters

In this section, we present results for a run in which we assume perfect adiabatic conditions along the vertical walls of the block. Again the top surface is held at 60°C and the atmosphere above the concrete floor is fixed at 20°C. As before, the heater borehole temperatures are held at 140°C. This run is intended to generate heat flux and temperature details that more closely represent those expected in the field, as opposed to the previous run which was intended mainly to aid in the design of the guard heaters.

The power required to maintain a heater borehole temperature of 140°C is reduced to a steady-state value of about 1400 W, compared to 2100 W without guard heaters. Heat fluxes through the top are shown in Fig. 7. Fluxes across horizontal lines through the center of the top surface, and 0.8 m from the center, are nearly identical at 55 W/m$^2$. The heat fluxes with guard heaters are more uniform across the top surface than without guard heaters. These fluxes are integrated to give a loss of 500 W, in contrast to 160 W lost without guard heaters. Heat is lost through the concrete floor at a rate of about 340 W.

Block temperatures are shown in Fig. 8. The one-year temperature distribution is essentially one-dimensional, having nearly uniform negative gradients directed upward and downward away from the heater horizon, except in areas close to the heater boreholes. This pattern is similar to the temperatures calculated in earlier hydrothermal runs (Lee, 1995).

## 4. Discrete Vertical Fractures

In this section we examine the effects of discrete vertical fractures striking parallel to the axes of the heater boreholes. This is the first of a series of discrete fracture runs we hope will help increase our understanding of the effects of fractures on the hydrothermal behavior of the system. We will vary the fracture orientation, aperture, and frequency, and observe the effect on the response of the system to thermal loading. We will also try to incorporate the major features of the fracture systems mapped in the field.

In this first run, we consider a fracture system made up of 200-$\mu$m aperture fractures with a uniform spacing of 30 cm. Fractures are assumed to intersect the borehole axes and pass midway between two boreholes.

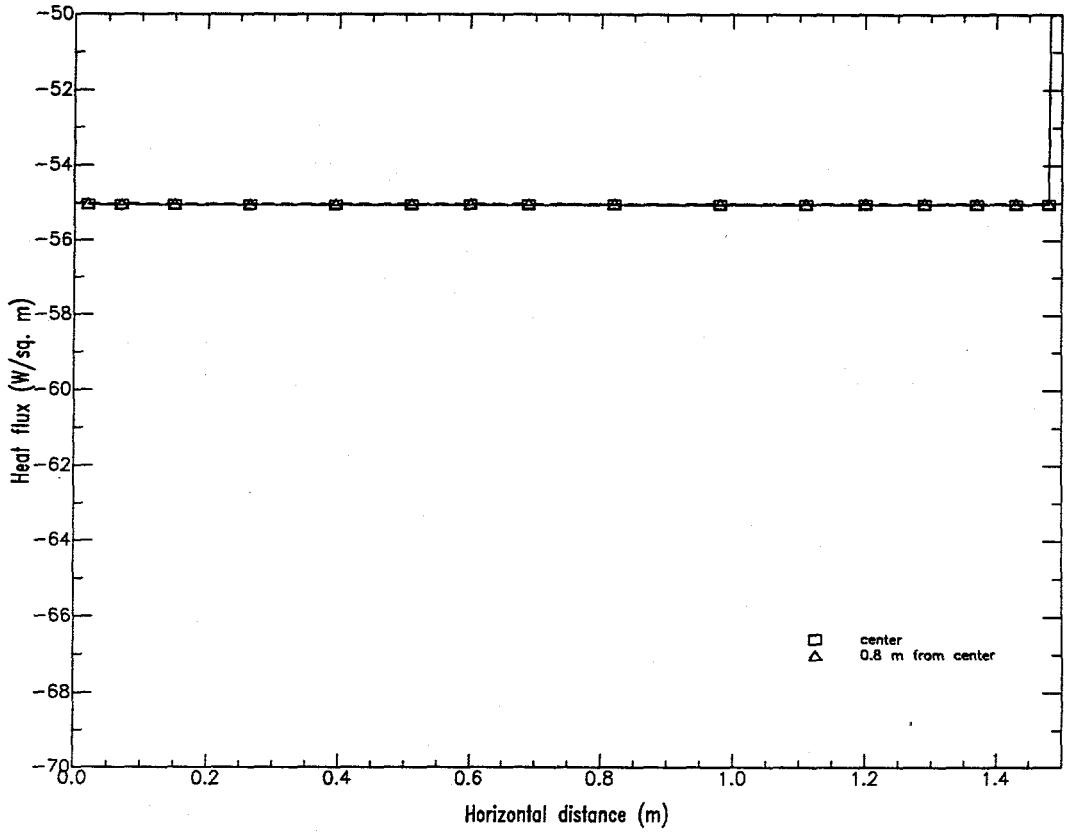


Figure 7. Heat loss through top of block, using guard heaters to enforce adiabatic walls. Negative fluxes here imply heat flow out of the block.

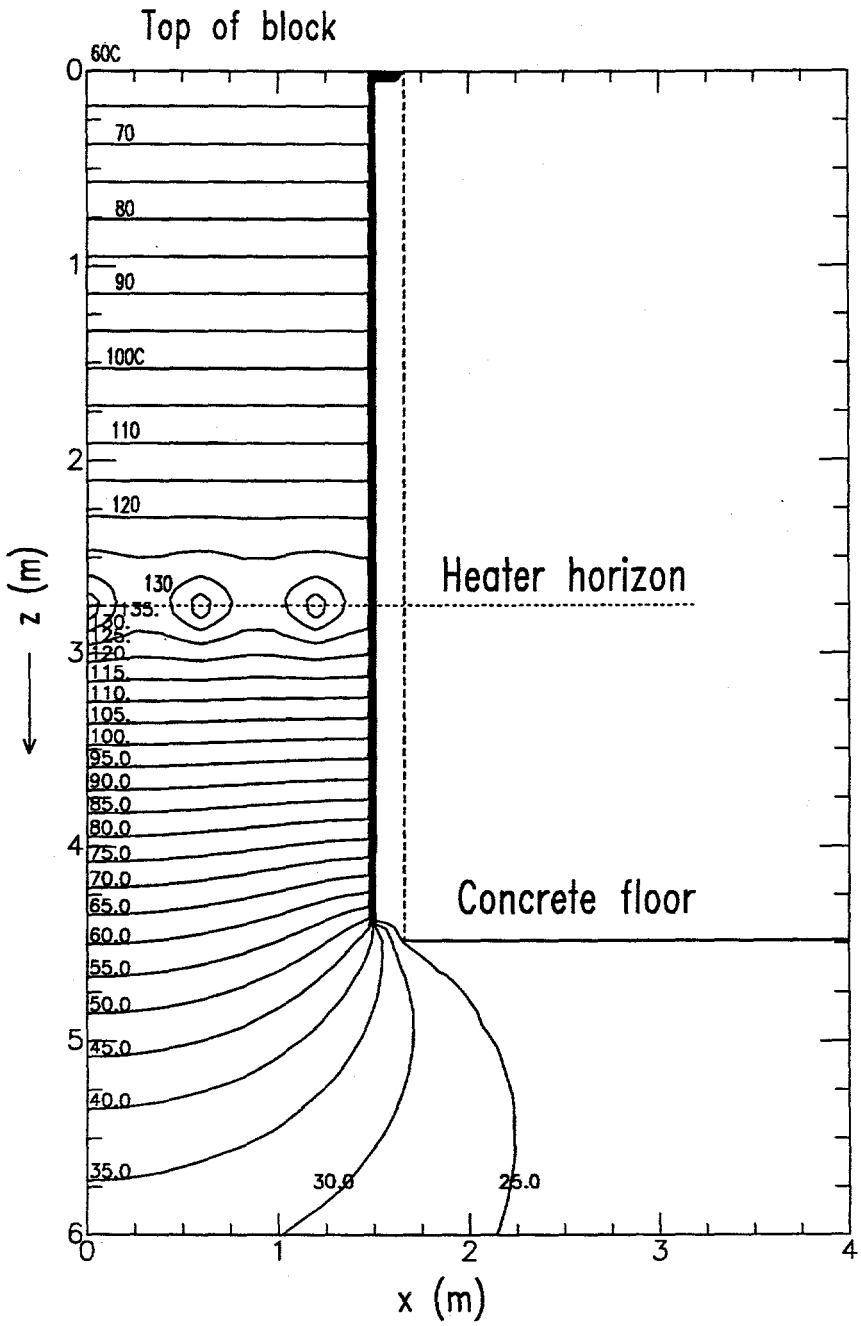


Figure 8. One-year block temperatures along an x-z plane through the center of the block. Guard heaters used to enforce adiabatic conditions along walls.

Table 2. Primary thermal and hydrologic properties of rock.

| | |
|---|---|
| Matrix specific heat | 840 J/kg°K |
| Matrix thermal conductivity (wet) | 2.10 W/m°K |
| Matrix porosity | 0.11 |
| Matrix permeability | 1.9 $\mu$darcy |
| Fracture aperture | 200 $\mu$m |
| Fracture frequency | 3.33 $m^{-1}$ |

Fig. 9 is a schematic of the block, showing the fracture system and the symmetry section modeled. The domain modeled is a 1/20 symmetry section bounded by fractures on the left and right. The power required to drive this section is equal to one quarter of the heating power contained in one borehole. The analysis is two-dimensional and ignores some small inaccuracy caused by asymmetry below the floor level of the block.

## 4.1. Grid Design and Input Data

Discretization for the symmetry section is shown in Fig. 10. Grid size varies from 100 $\mu$m at the fractures, representing half the fracture aperture, to 15 m at the bottom of the domain. The model is 68 m deep. The symmetry boundaries, at x values of 0 and 0.3 m, are no-flow adiabatic boundaries through the center of the fractures. The upper boundary represents the atmosphere, which is held at 20°C and zero liquid saturation. The lower boundary is held at the initial liquid saturation of 0.5 and initial temperature of 20°C. As before, the heaters were energized to give a heater borehole temperature of 140°C for one year.

The primary thermal and hydrologic properties of the rock matrix and fractures are given in Table 2. Properties of the rock matrix were obtained from the YMP Reference Information Base (1990).

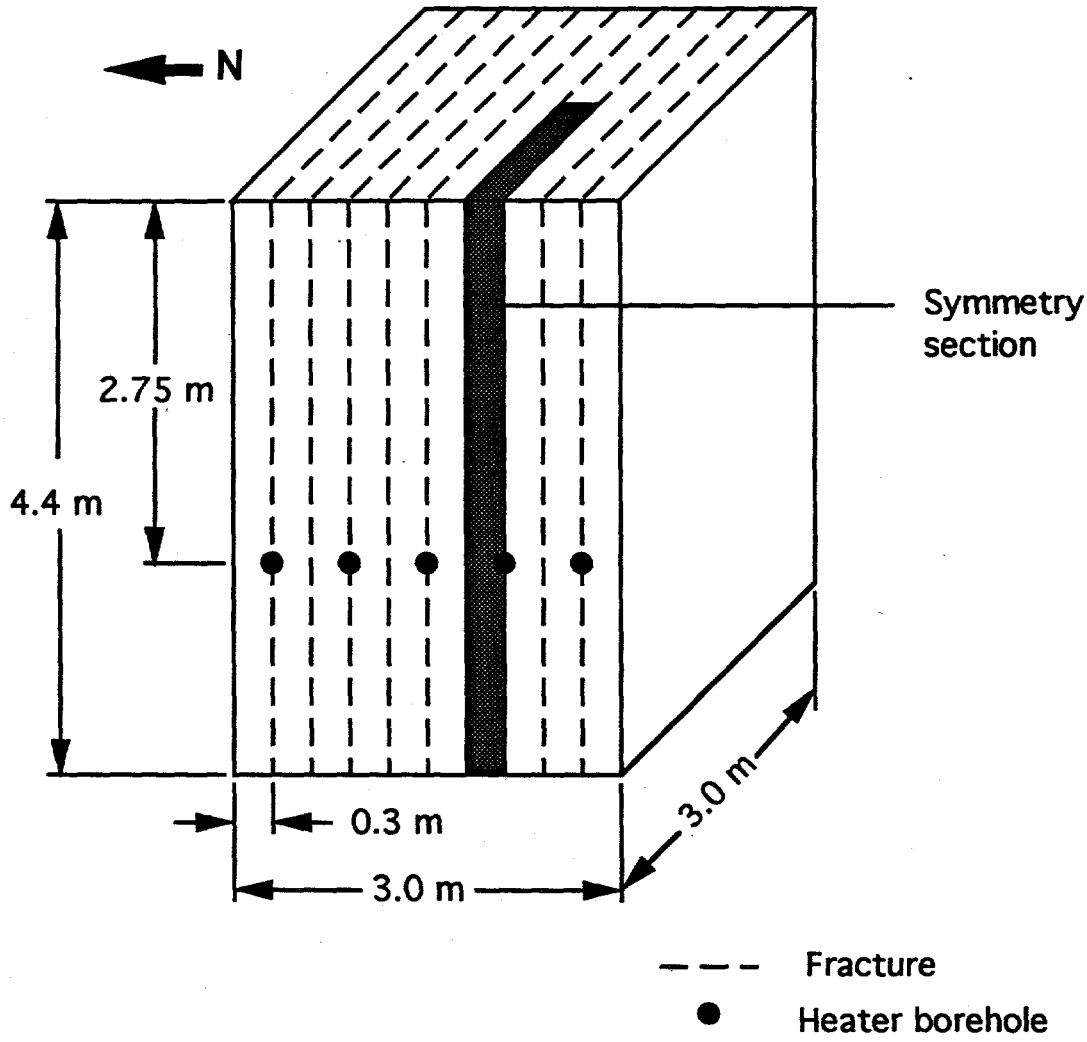


Figure 9. Schematic of Large Block showing locations of fractures and heater boreholes. The shaded area is the 1/20 symmetry section modeled.

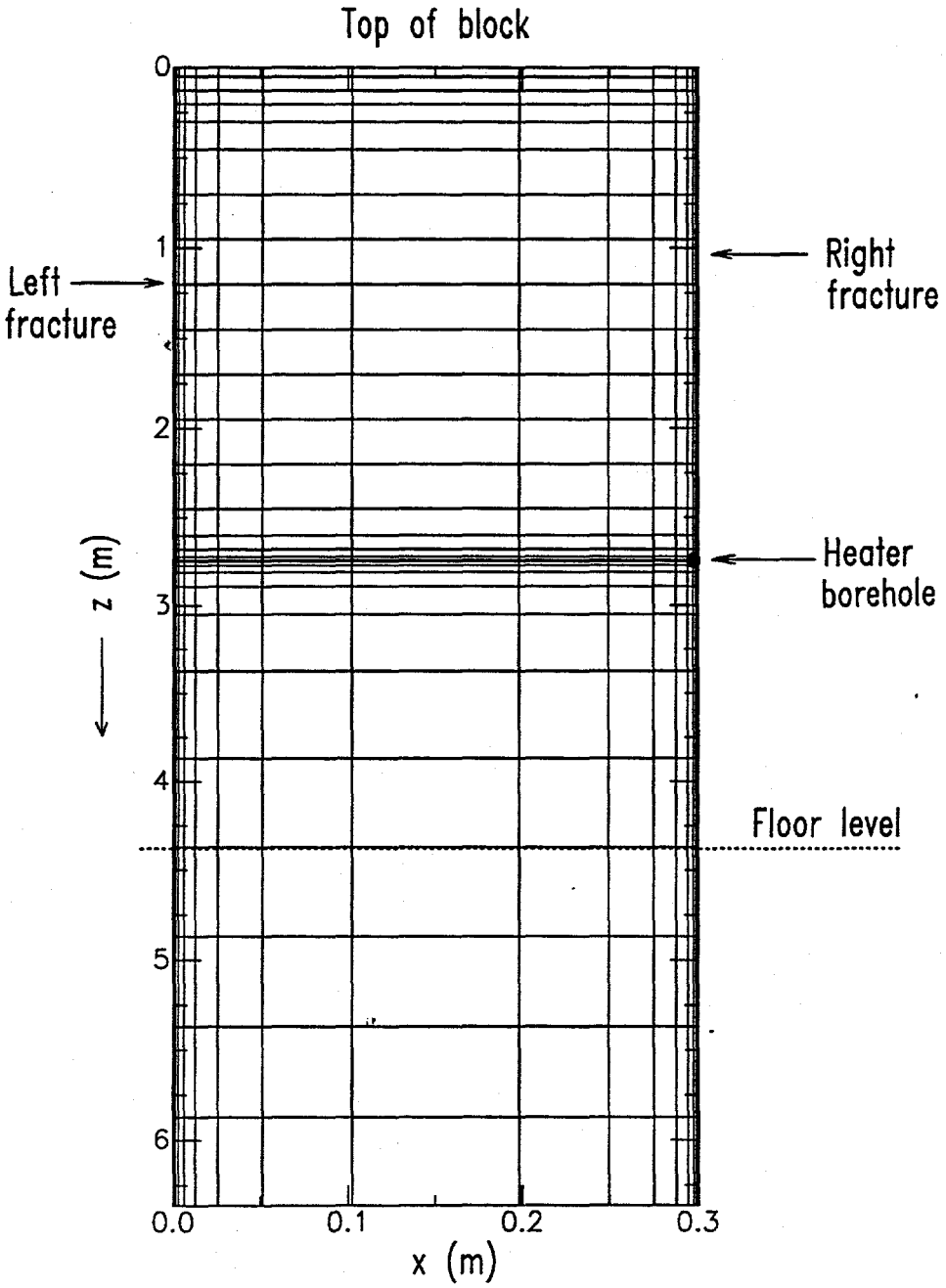


**Figure 10. Grid design for discrete-fracture run.**

## 4.2. Fracture Modeling Results

Block temperatures after one year of heating are shown in Fig. 11. The temperature distribution is essentially one-dimensional, except at locations within a few centimeters of the heater. Temperatures decrease with distance both upward and downward away from the heater horizon; gradients above the heater horizon are slightly greater than those below. The temperatures are unaffected by the locations of the fractures.

Images of liquid saturation at 50, 100, 200, and 365 days are shown in Fig. 12. Preferential drying occurs along the fractures at earlier times, starting at the heater horizon. At 50 days, dryout areas are developing along the fractures, with some penetration into the matrix evident. At 100 days, the dryout zone extends further along the fractures and deeper into the matrix. In addition, a recondensation zone is beginning to develop above the dryout zone. Note that the figure has a horizontal-to-vertical scale exaggeration of 10:1, which tends to mask the fact that extension of the dryout zone along the fractures is much more rapid than penetration into the matrix. At 200 days, distinct dryout and recondensation zones are established. The dryout zone is thickest at the two ends, where the fractures are located, and thinnest in the matrix midway between the fractures. After 365 days of heating, both the dryout and recondensation zones are even thicker, with the recondensation zone centered about 0.9 m from the top of the block.

Fig. 13 shows the one-year temperature and liquid saturation profiles along a vertical line midway between the two fractures. Again, distinct dryout and recondensation zones are evident. If the dryout zone is defined as a region with liquid saturation below half the initial value of 0.5, then the dryout zone is about 2.0 m thick here. The temperature in this zone is above boiling. A well-established recondensation zone occurs above the heater horizon, with peak liquid saturation of 0.87 at a depth of about 0.9 m. The recondensation zone below the heater horizon is smaller, having a peak liquid saturation of 0.66 at depth 5.6 m.

Images of gas pressures at 50, 100, 200, and 365 days are shown in Fig. 14. While the fractures remain at approximately barometric pressure (83 kPa at the site), the peak pressure in the system occurs within the rock matrix, in the heater horizon. The location of this peak pressure is initially

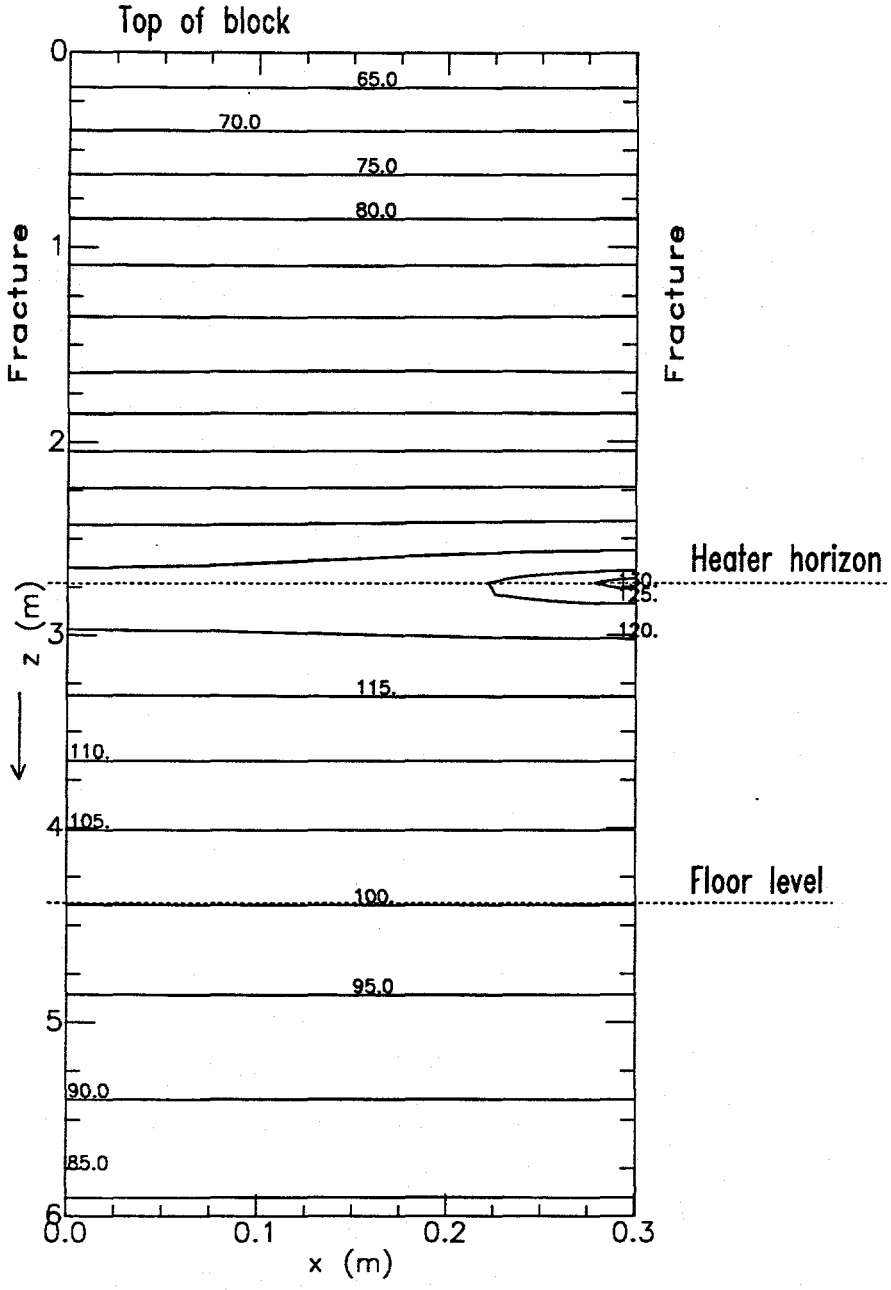


Figure 11. Block temperatures after 365 days; discrete-fracture run.

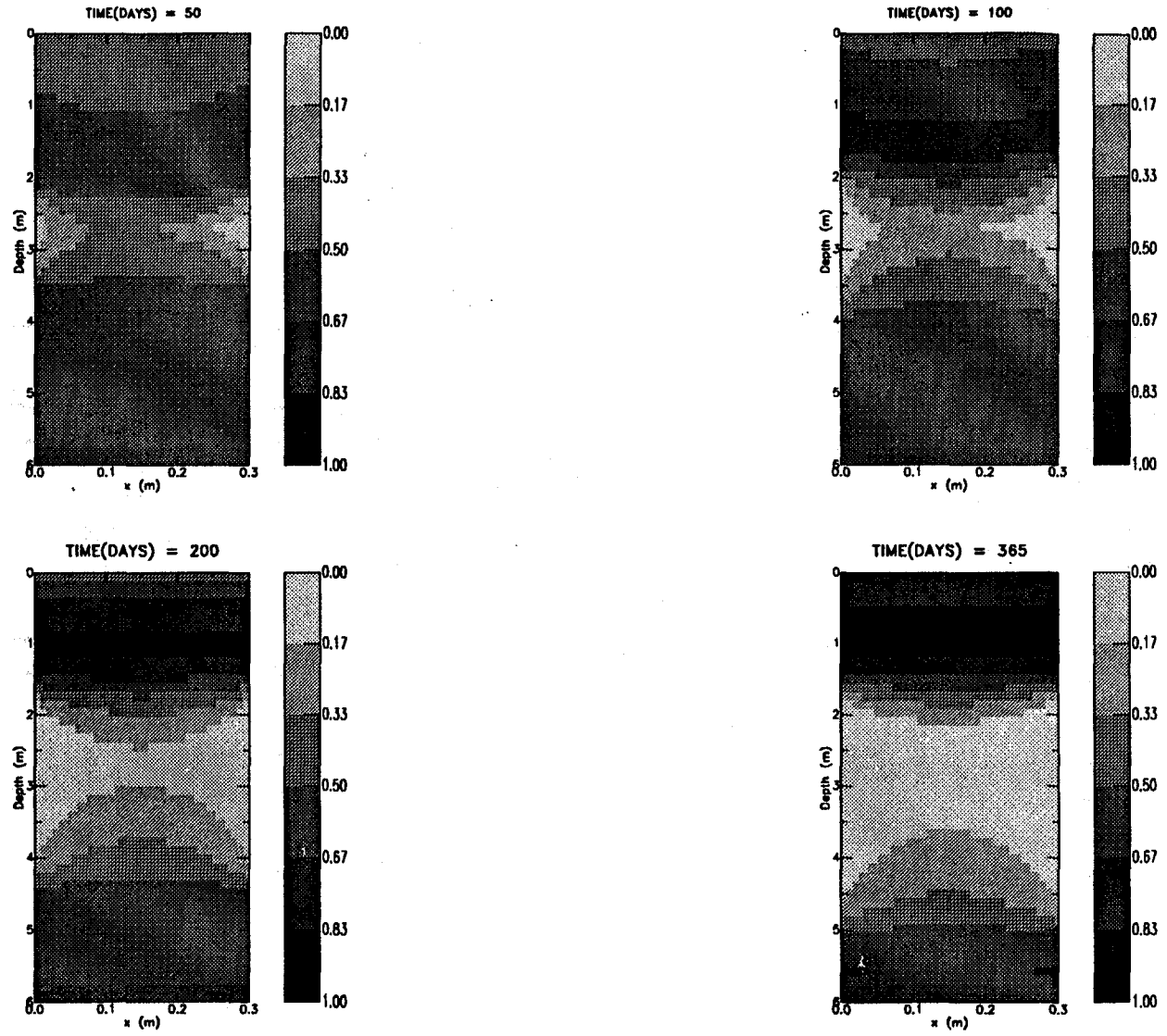


Figure 12. Images of liquid saturations for discrete fracture model. Saturations shown at (a) 50 days, (b) 100 days, (c) 200 days, and (d) 365 days.

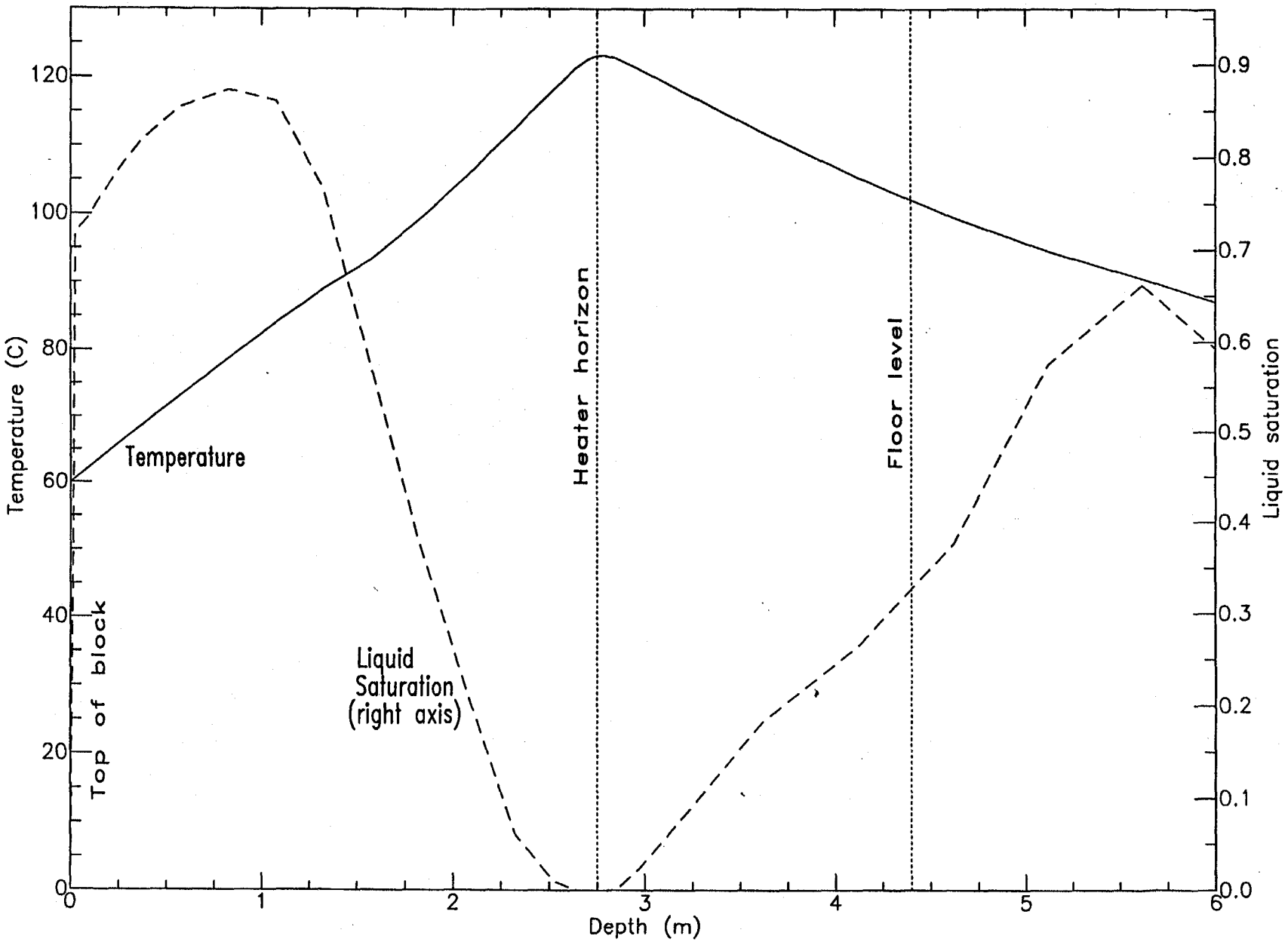


Figure 13. One-year temperature and liquid saturation profiles along vertical line through matrix, midway between fractures

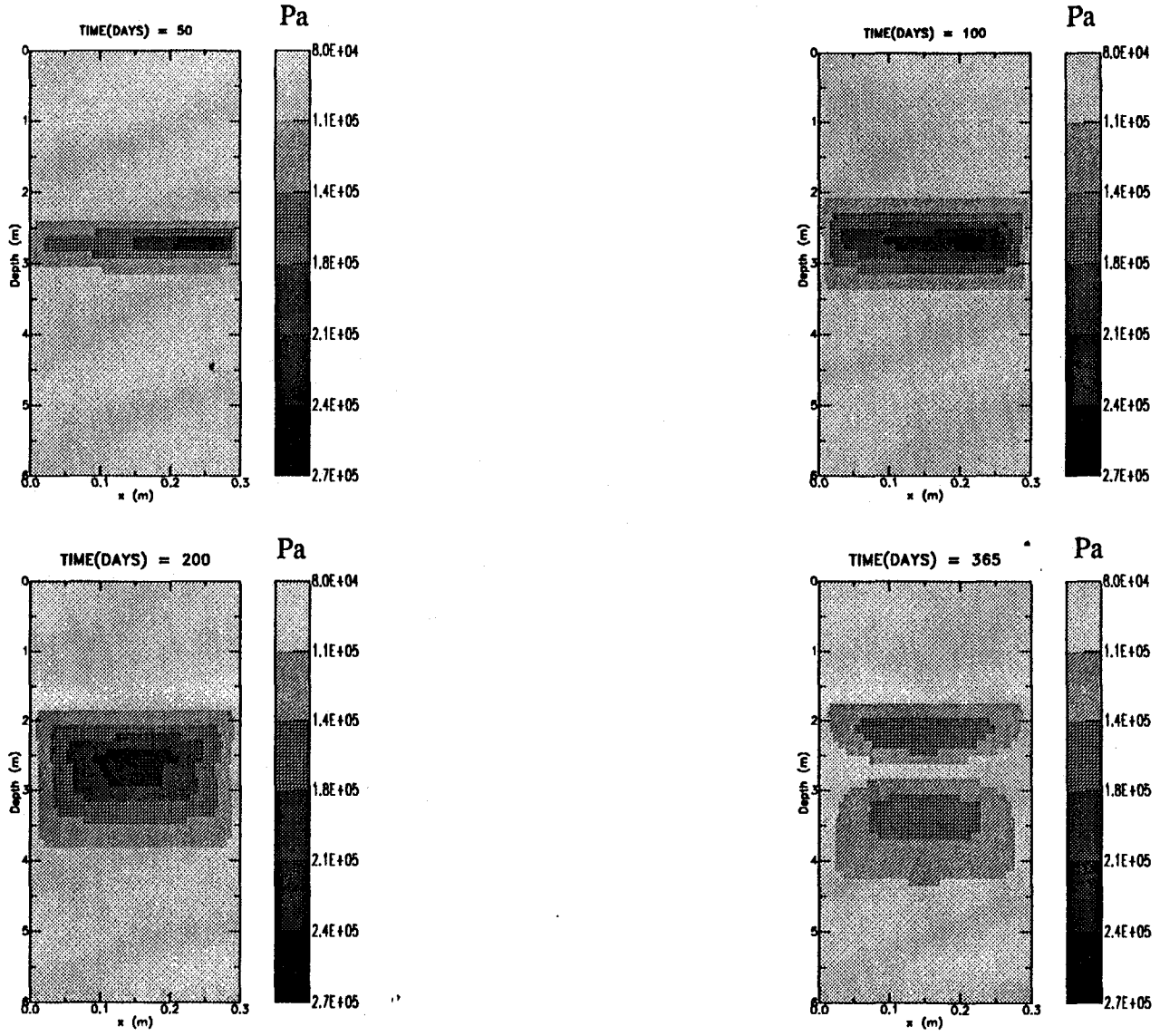


Figure 14. Images of absolute gas pressure for discrete fracture model. Pressure shown at (a) 50 days, (b) 100 days, (c) 200 days, and (d) 365 days. Barometric pressure is 82.7 kPa

close to the heater but shifts closer to the center of the matrix with time. It appears to be centered midway between the fractures at 200 days. The peak pressure decreases as the system approaches steady state.

Fig. 15 shows gas pressures along the heater horizon, from the left fracture to the right fracture, after 100 days of heating. The pressure goes from barometric pressure of 83 kPa at the fractures to a high of about 260 kPa in the matrix. This is about the highest pressure observed in the system, and is equivalent to a gage pressure of 177 kPa (26 psig).

# 5. Summary and Conclusions

In this second progress report, we have presented results of the final set of numerical modeling calculations performed in support of the LBT design. We used a three-dimensional conduction-only model to study the thermal behavior of the system. The results include the distribution of heat fluxes across the block surfaces, and are used primarily for the design of guard heaters to enforce adiabatic conditions along the block walls. We also examined a two-dimensional, hydrothermal, discrete-fracture model, with 200-$\mu$m vertical fractures parallel to the heaters with a uniform spacing of 30 cm. This is the first of a series of discrete fracture models we plan to run in our efforts to improve our understanding of the role of fractures in the hydrothermal response of the block to heating.

For the conduction-only analysis, the block was heated at a constant heater borehole temperature of 140°C, and the temperature at the upper surface was fixed at 60°C. Runs were made from an initial temperature of 20°C and an initial liquid saturation of 0.5. Two runs were made: the first assuming imperfectly insulated walls, and the second assuming that guard heaters enforce perfectly adiabatic walls. The results gave heat loss fluxes across various surfaces. Without guard heaters, the steady-state power required to heat the system was 2100 W, with 59% of the heat input lost through the insulated walls, and 8% lost through the top surface. With guard heaters, the steady-state power required was 1400 W, with 36% lost through the top surface.

For the discrete-fracture model, distinct dryout and recondensation zones were observed, both above and below the heater horizon. The dry-

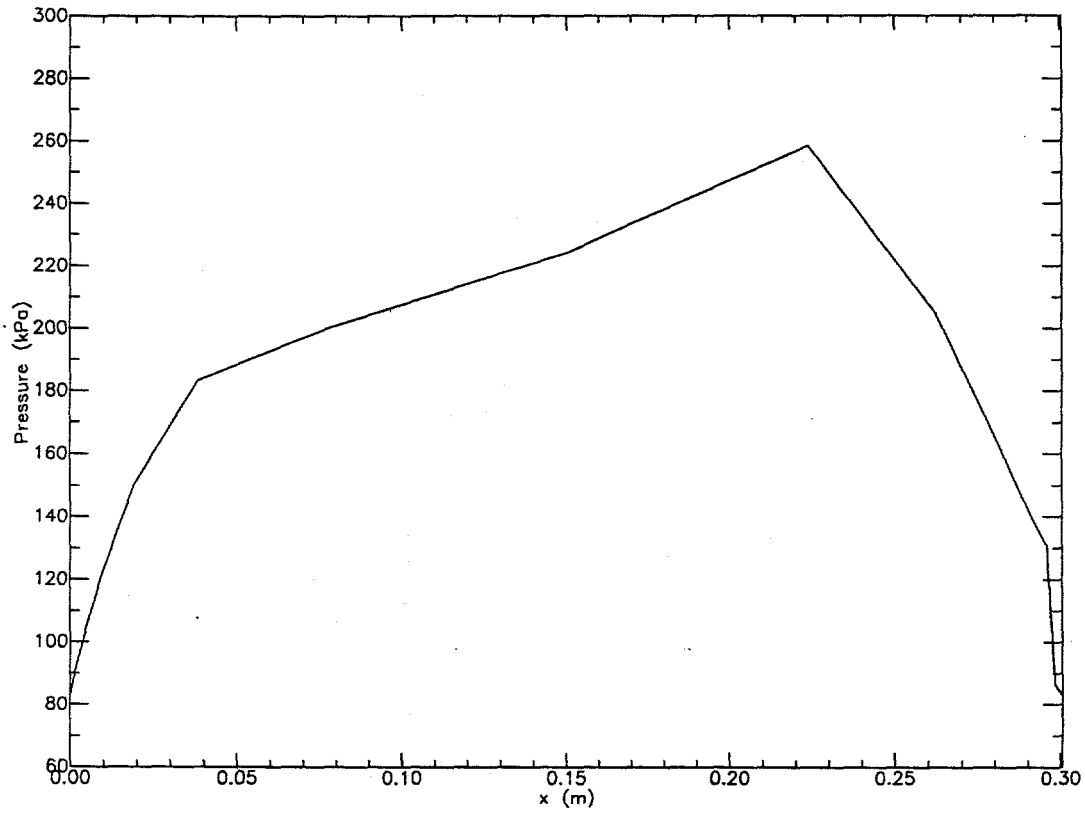


Figure 15. Absolute gas phase pressure along horizontal line from left fracture to right fracture, in heater horizon; pressures shown at 100 days.

out zones are thickest at the fractures and thinnest in the matrix midway between the fractures. Block temperatures seem unaffected by the location of the fractures. The peak gage pressure in the system was about 177 kPa (26 psig), located in the matrix at the heater horizon.

# References

Buscheck, T.A., and J.J. Nitao, "The Analysis of Repository-Heat-Driven Hydrothermal Flow at Yucca Mountain," American Nuclear Society, *Proceedings, Fourth International High-Level Radioactive Waste Management Conference*, Las Vegas, NV, April 1993. Also, UCRL-JC-112444, Lawrence Livermore National Laboratory, Livermore, CA (1993a). (NNA.930315.0009)

Buscheck, T.A., and J.J. Nitao, "Repository-Heat-Driven Hydrothermal Flow at Yucca Mountain, Part I: Modeling and Analysis," *Nuclear Technology*, Vol. 104, No. 3, pp. 418–448 (1993b). (NNA.940427.0095)

Lee, K.H., "Progress Report on Pre-Test Calculations for the Large Block Test," UCRL-ID-118699, Lawrence Livermore National Laboratory, Livermore, CA (1995).

Lienhard, J.H., *A Heat Transfer Textbook*, 2nd ed., Prentice-Hall, Inc., New Jersey (1987).

Lin W. and W. Daily, "Laboratory Study of Fracture Healing in Topopah Spring Tuff – Implications for Near Field Hydrology," *Proceedings of the Topical Meeting on Nuclear Waste Isolation in the Unsaturated Zone*, Focus '89, American Nuclear Society, La Grange Park, IL (1989). (NNA.900711.0241).

Lin, W., D.G. Wilder, J.A. Blink, S.C. Blair, T.A. Buscheck, D.A. Chesnut, W.E. Glassley, K.H. Lee, and J.J. Roberts, "The Testing of Thermal-Mechanical-Hydrological-Chemical Processes Using a Large Block," UCRL-JC-114776, Lawrence Livermore National Laboratory, Livermore, CA (1994a). (RA)

Lin, W., D.G. Wilder, J.A. Blink, S.C. Blair, T.A. Buscheck, R.S. Glass, W.E. Glassley, K. Lee, R.D. McCright, M.W. Owens, and J.J. Roberts, "A Large Block Heater Test for High Level Nuclear Waste Management," UCRL-JC-116431, Lawrence Livermore National Laboratory, Livermore, CA (1994b). (RA)

Nitao, J.J., "V-TOUGH – An Enhanced Version of the TOUGH Code for the Thermal and Hydrologic Simulation of Large-Scale Problems in Nuclear Waste Isolation," UCID-21954, Lawrence Livermore National Laboratory, Livermore, CA (1989). (RA)

Nitao, J.J., "The NUFT Code for Modeling Nonisothermal, Multiphase, Multicomponent Flow and Transport in Porous Media," AGU EOS, Vol. 74, No. 3, p 313, 1993 (presented at the 1993 Fall AGU Conference).

Ramirez, A.L., T.A. Buscheck, R. Carlson, W. Daily, K.H. Lee, W. Lin, N. Mao, T.S. Ueng, H. Wang, and D. Watwood, "Prototype Engineered Barrier System Field Test (PEBSFT), Final Report," UCRL-ID-106159, Lawrence Livermore National Laboratory, Livermore, CA (1991). (RA)

"Yucca Mountain Project Reference Information Base," YMP/CC-0002 (Version 04.002), Nevada Operations Office, U.S. Department of Energy (1990). (NNA.910129.0066)

Lastly we examine the least squares polynomial which has demonstrated the most promise of any preconditioner implemented so far. The results plotted in Figure 18 show that for this method there are substantial differences on how the preconditioner works at different frequencies. At 0.9 kHz, the minimum convergence time occurs when 9 terms are employed in the polynomial, at 7.2 kHz when 3 to 6 terms are employed, and finally at 56 kHz when 2 to 3 terms are used. The maximum time savings over simple Jacobi scaling in each of these three cases is 24%, 18% and 13% respectively. From these results it appears that this preconditioner works better at low frequencies. We believe that this observation may be a function of how the coefficients of the polynomial are chosen. Remember from an earlier section that these are determined according to the distribution of eigenvalues along the real axis. However, because our system is not positive definite there will exist imaginary eigenvalues. It is possible that the real eigenvalue approximation works better at lower frequencies than at higher, and thus to get better performance, the polynomial preconditioner needs to be redesigned such that these imaginary values are taken into consideration.

## CONCLUSIONS AND DISCUSSION

In this chapter we have presented a scheme to solve for the frequency domain electromagnetic response of a 3-D earth over a wide band of frequencies using massively parallel computers. The problems associated with porting the serial version of the scheme to a parallel machine have been outlined, and a variety of comparisons have been demonstrated to prove the validity of the code. Implementing the code on the 1840 processor Intel Paragon has demonstrated a decrease in computing time of over two orders of magnitude when compared to a high end IBM workstation and a similar magnitude increase in the maximum model size that can be simulated. In addition a maximum theoretical flop rate of 14.9 Gflops has been established. Finally we have demonstrated the use of different Krylov solvers and preconditioners and found the QMR scheme coupled with a least squares polynomial and simple Jacobi scaling to be the most efficient yet stable method of solution that we have available.

Currently we are using the scheme in a variety of projects, for example to assist in the design of geophysical instruments (Pellerin et al, 1995) as well as simulating airborne EM surveys (Alumbaugh and Newman, 1995; Newman and Alumbaugh, 1994). The simulations that we are running for these projects would have been impossible prior to the parallel implementation due to the size of the models and/or the number of frequencies and sources involved. We believe, however, that there is still much research to be done with regards to the implementation of this type of scheme. The most notable location for improvement is in the area of preconditioners. Techniques being considered are multigrid preconditioners, and methods to separately treat the real and imaginary components of the matrix system. A thorough study of the grid stretching

parameters at frequencies lower than 1 MHz also needs to be undertaken. This type of study will hopefully yield either an analytical or empirical method of choosing them based on the frequency, conductivity of the medium, etc., similar to the scheme employed at higher frequencies. A method to accelerate the convergence for very low frequency simulations where channeling currents dominate needs to be developed in order to simulate natural field measurements as well as extend the frequency band down below 100 Hz; Smith (1992) has found that a static correction can be incorporated to accommodate this. Finally, methods of dealing with the air-earth interface need to be more closely examined. We have found that this interface tremendously complicates the numerical problem, especially when electric dipole sources are employed on the surface.

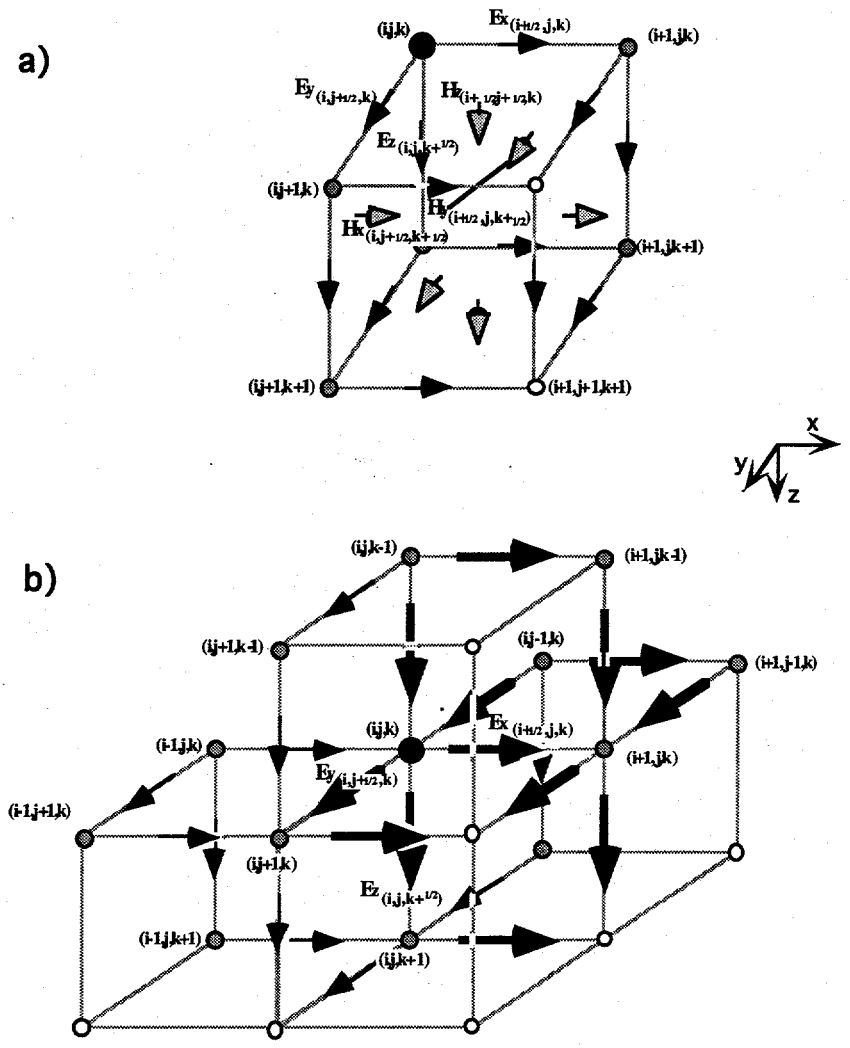


Figure 1 - a) The staggered grid for the coupled Maxwell's equations (after Yee, 1966). The electric field is sampled at the center of the cell edges, and the magnetic fields at the center of the cell faces. Node (i,j,k) is the large dark circle in the upper-back-left hand corner of cell (i,j,k), and has the six unknown electric and magnetic fields illustrated assigned to it. Cell (i,j,k) has a conductivity $\sigma_{i,j,k}$, a dielectric permitivity $\varepsilon_{i,j,k}$, and magnetic permeability $\mu_{i,j,k}$ assigned to it. b) The staggered grid for the Helmholtz equation for the electric fields. The dark circle at the center represents node (i,j,k) which has the three hi-lighted components of the electric field assigned to it. The large arrows represent the 13 unknown electric field values needed to form the equation for Ex at node (i,j,k), with the other arrows representing the additional fields needed to form the equations for Ey and Ez. The gray circles represent nodal points to which unknown electric field values are assigned that are needed to complete the three equations at node (i,j,k); the open circles represent nodal points from which no information is needed for these equations.

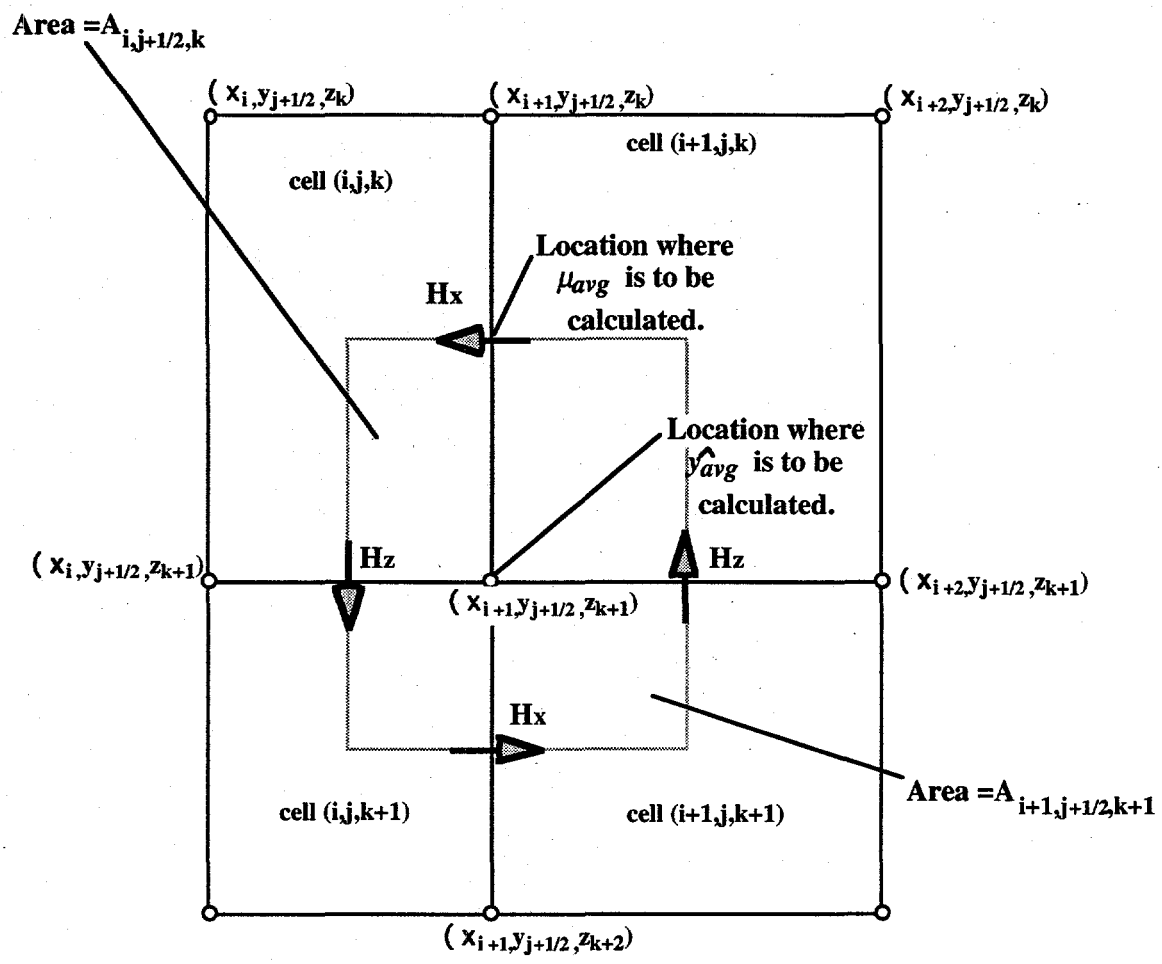


Figure 2 - Illustration to demonstrate how the average admittivity is calculated halfway along a cell edge in the y direction, and the average magnetic permeability is calculated at the center of the cell face.

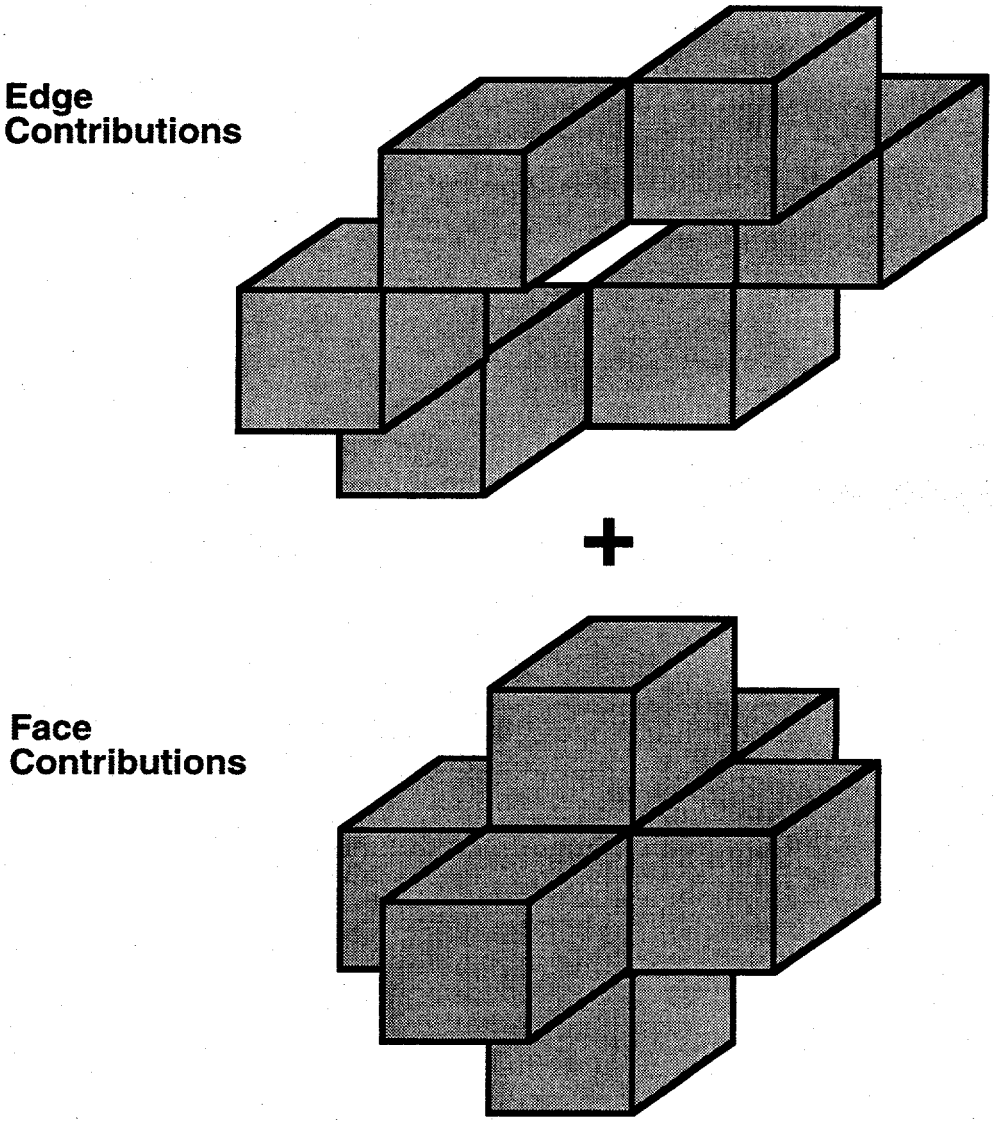


Figure 3 - The processor communication stencil that provides for proper message passing in the solution phase of the program. Each cube represents a neighboring processor with which a processor located at the center of the "face contributions" cluster would need to exchange information through message passing.

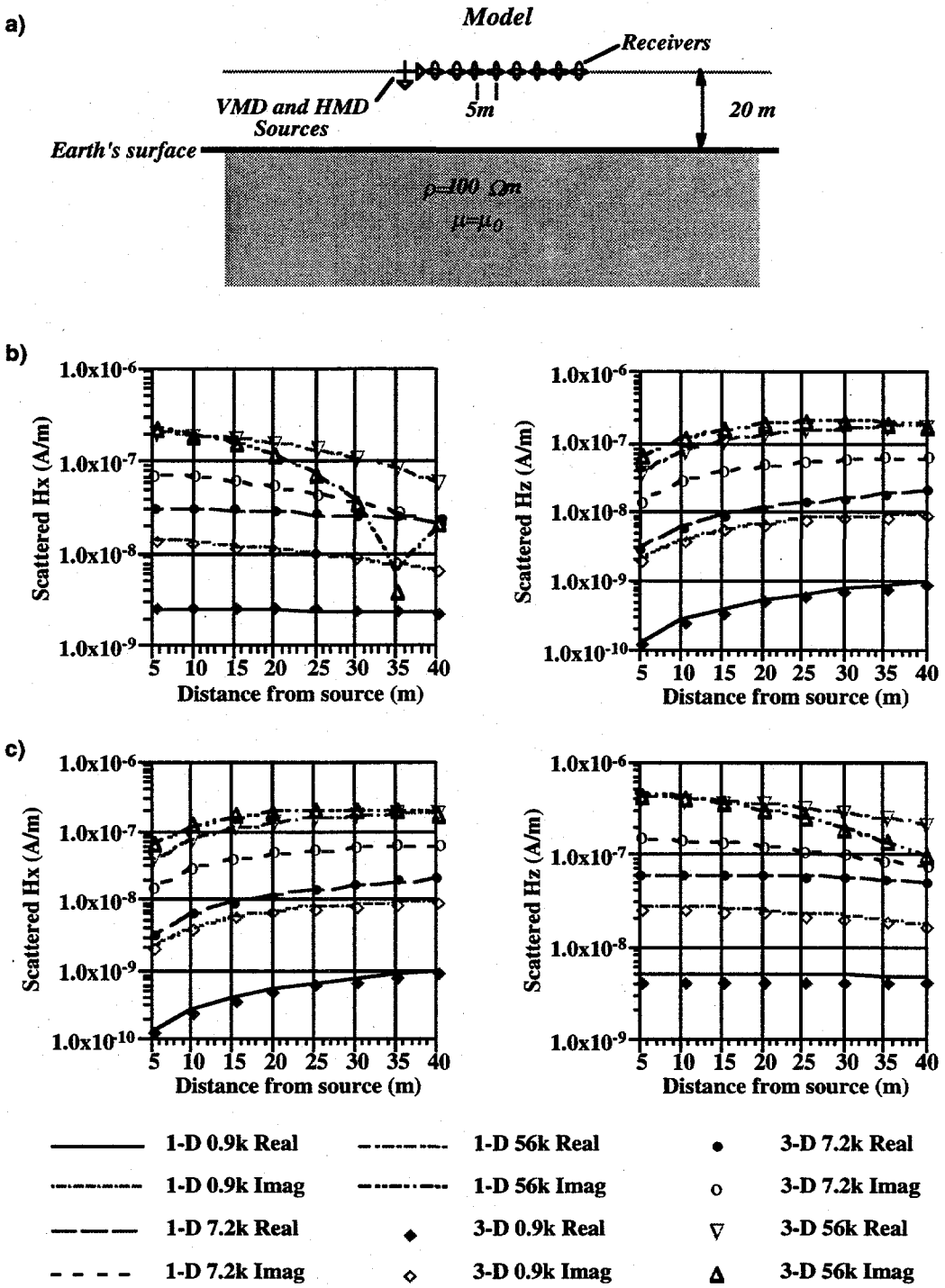


Figure 4 - a) Airborne simulation with sources and receivers above a non-magnetically permeable halfspace. The three frequencies employed are 0.9 kHz, 7.2 kHz, and 56 kHz. The comparisons are between the 3-D finite difference scheme and Lee's 1-D solution. b) Horizontal and vertical magnetic field results for a HMD source. c) Horizontal and vertical magnetic field results for a VMD source.

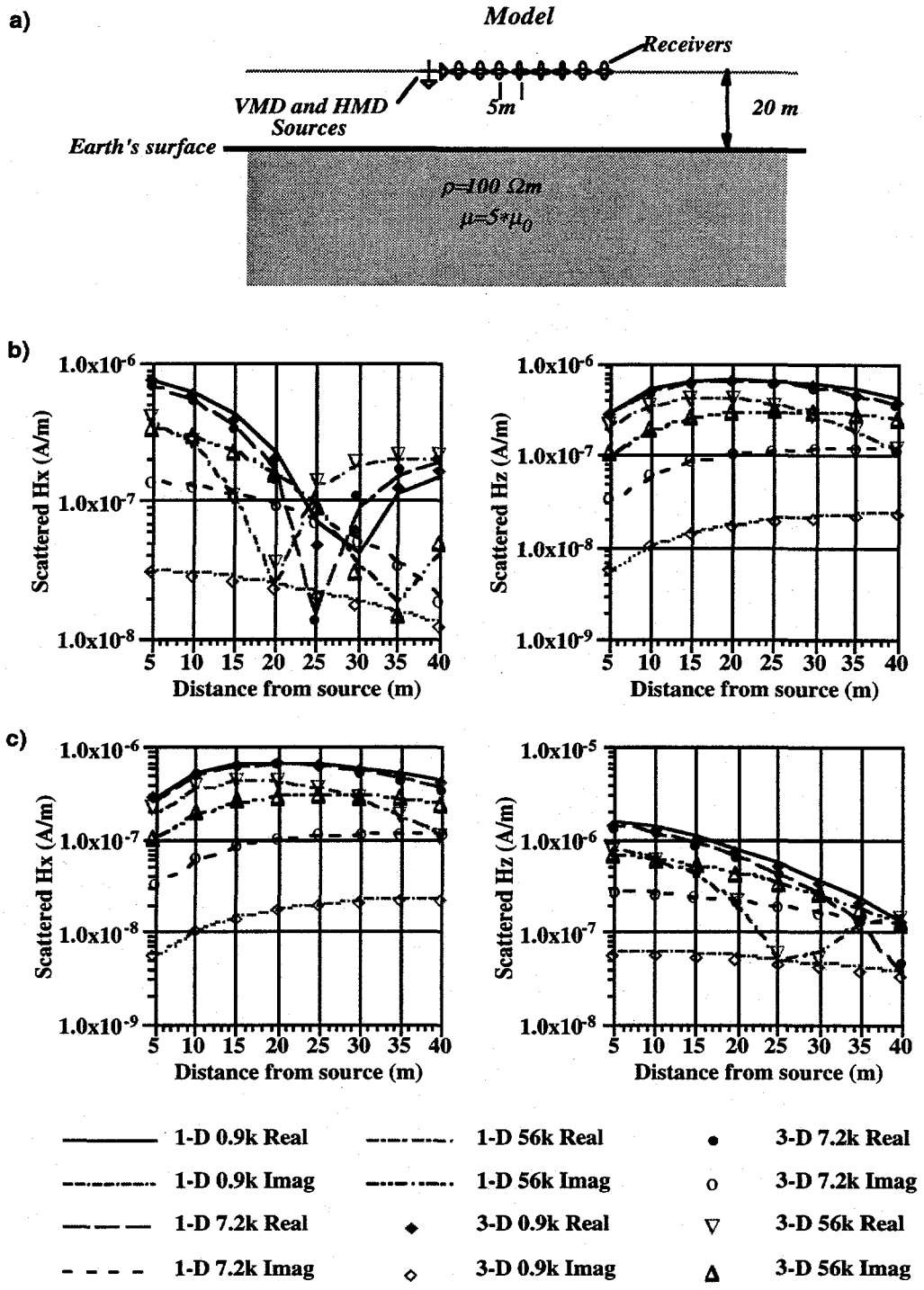


Figure 5 - a) Airborne simulation with sources and receivers above a magnetically permeable halfspace. The three frequencies employed are 0.9 kHz, 7.2 kHz, and 56 kHz. The comparisons are between the 3-D finite difference scheme and Lee's 1-D solution. b) Horizontal and vertical magnetic field results for a HMD source. c) Horizontal and vertical magnetic field results for a VMD source.

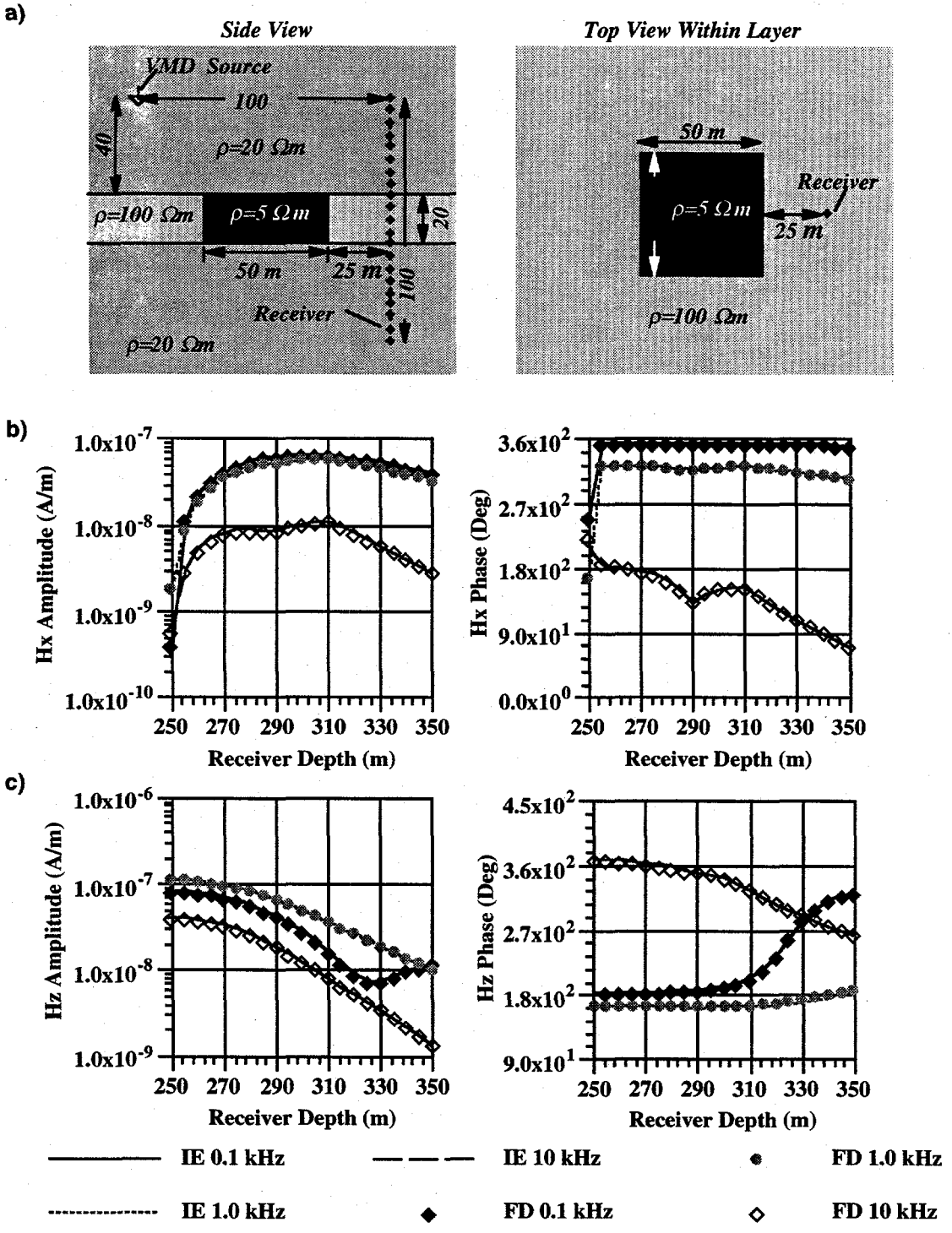


Figure 6 - a) Crosswell model with VMD source located 40m above the resistive layer. The receiver depths range from 250 m to 350 m, and the frequencies employed are 0.1 kHz, 1 kHz and 10 kHz. The comparisons are between the 3-D finite difference scheme and the integral equation solution of Newman et al. (1986). b) Horizontal magnetic field results. c) Vertical magnetic field results.

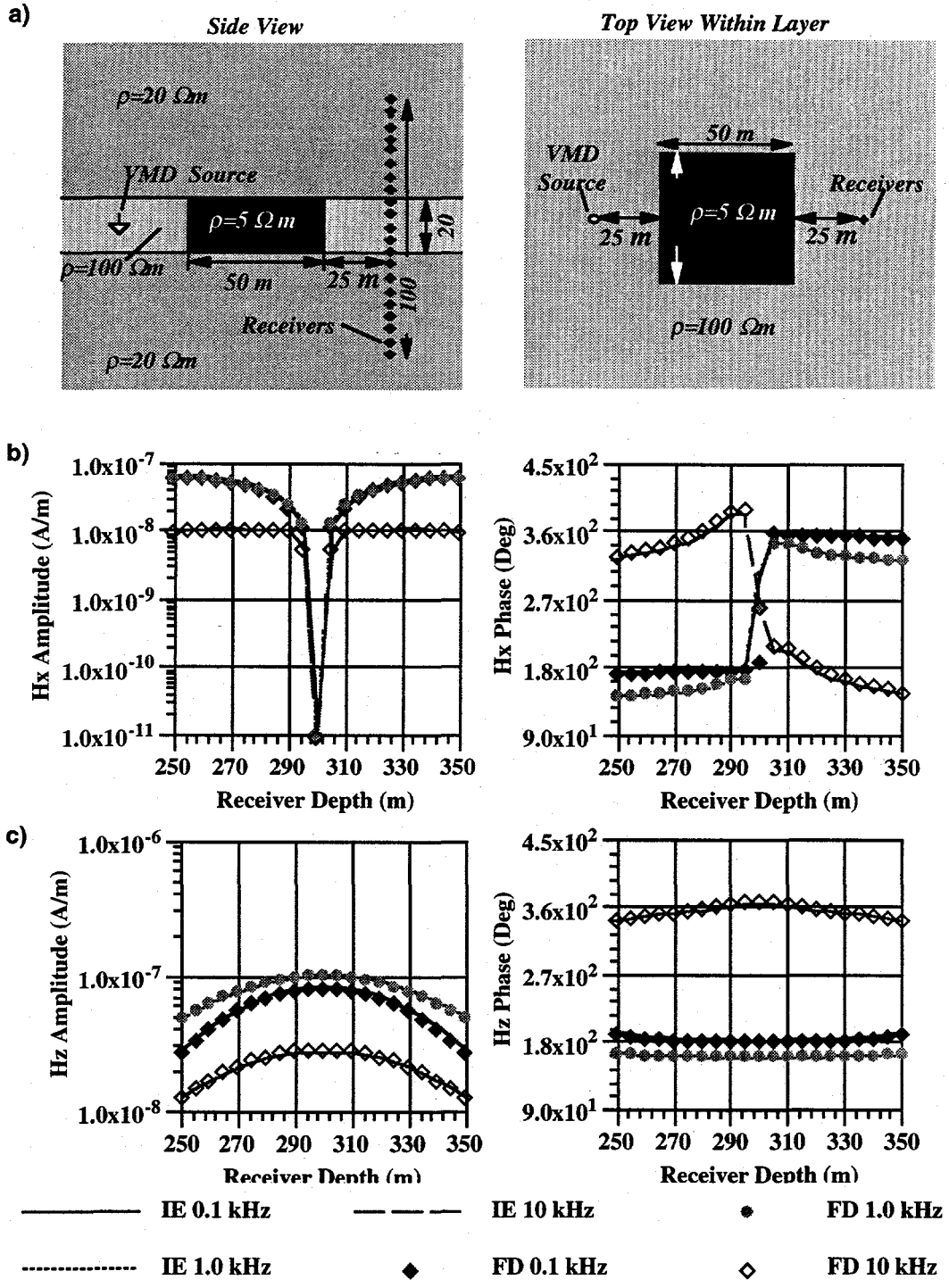


Figure 7 - a) Crosswell model with VMD source located within the resistive layer. The receiver depths range from 250 m to 350 m, and the frequencies employed are 0.1 kHz, 1 kHz and 10 kHz. The comparisons are between the 3-D finite difference scheme and the integral equation solution of Newman et al. (1986). b) Horizontal magnetic field results. c) Vertical magnetic field results.

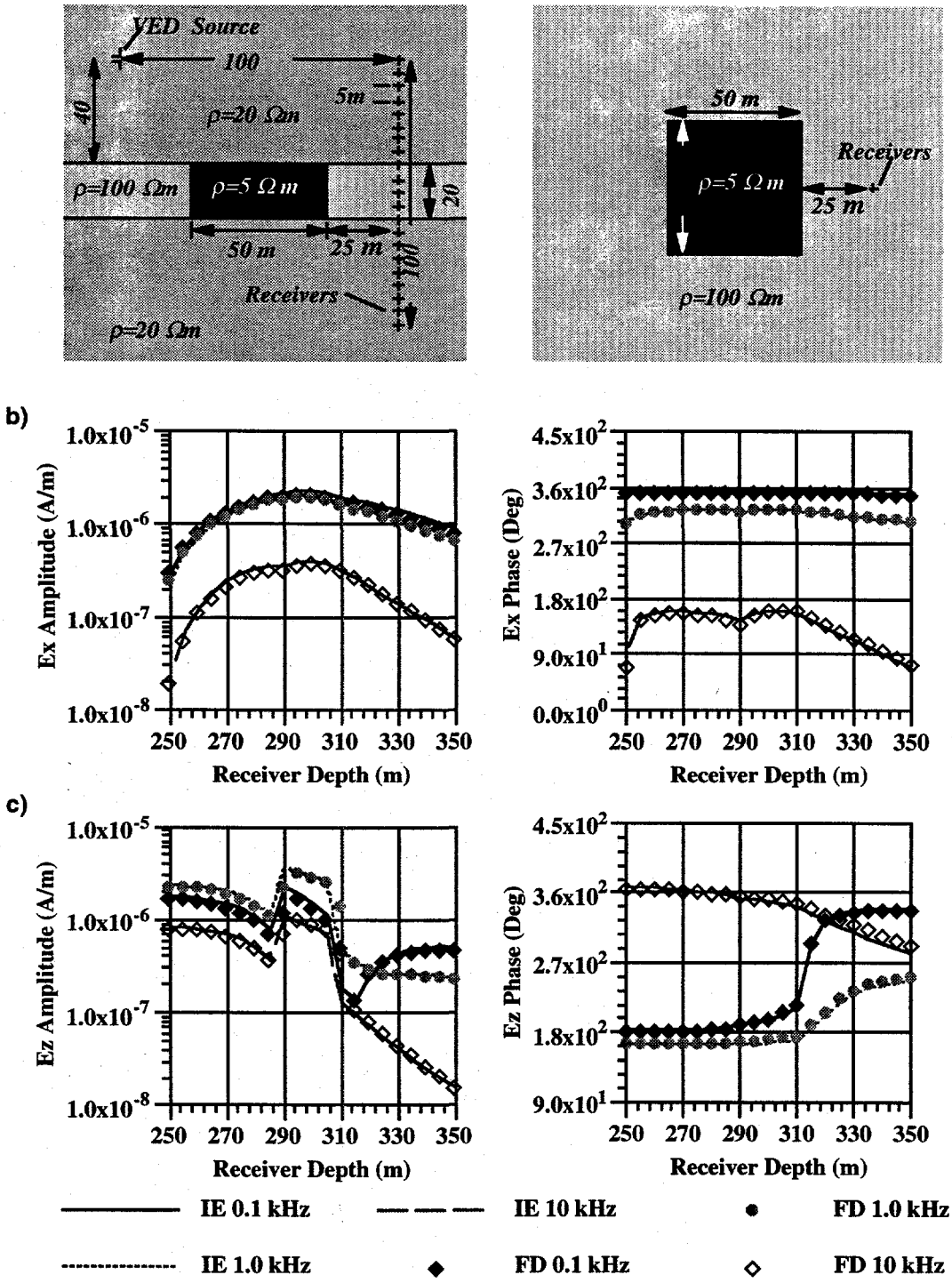


Figure 8 - a) Crosswell model with VED source located 40m above the resistive layer. The receiver depths range from 250 m to 350 m, and the frequencies employed are 0.1 kHz, 1 kHz and 10 kHz. The comparisons are between the 3-D finite difference scheme and the integral equation solution of Newman et al. (1986). b) Horizontal electric field results. c) Vertical electric field results.

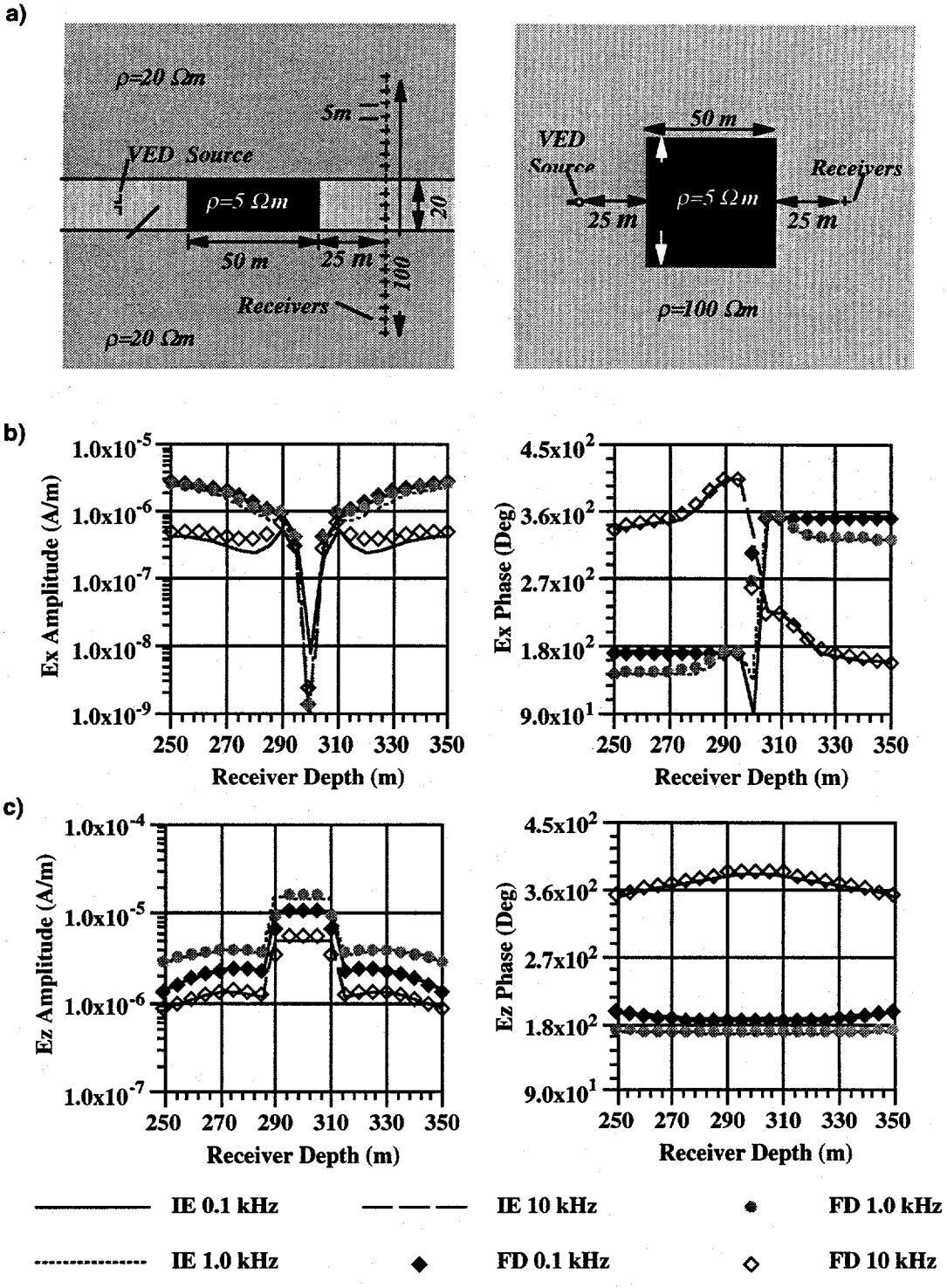


Figure 9 - a) Crosswell model with VED source located within the resistive layer. The receiver depths range from 250 m to 350 m, and the frequencies employed are 0.1 kHz, 1 kHz and 10 kHz. The comparisons are between the 3-D finite difference scheme and the integral equation solution of Newman et al. (1986). b) Horizontal electric field results. c) Vertical electric field results.

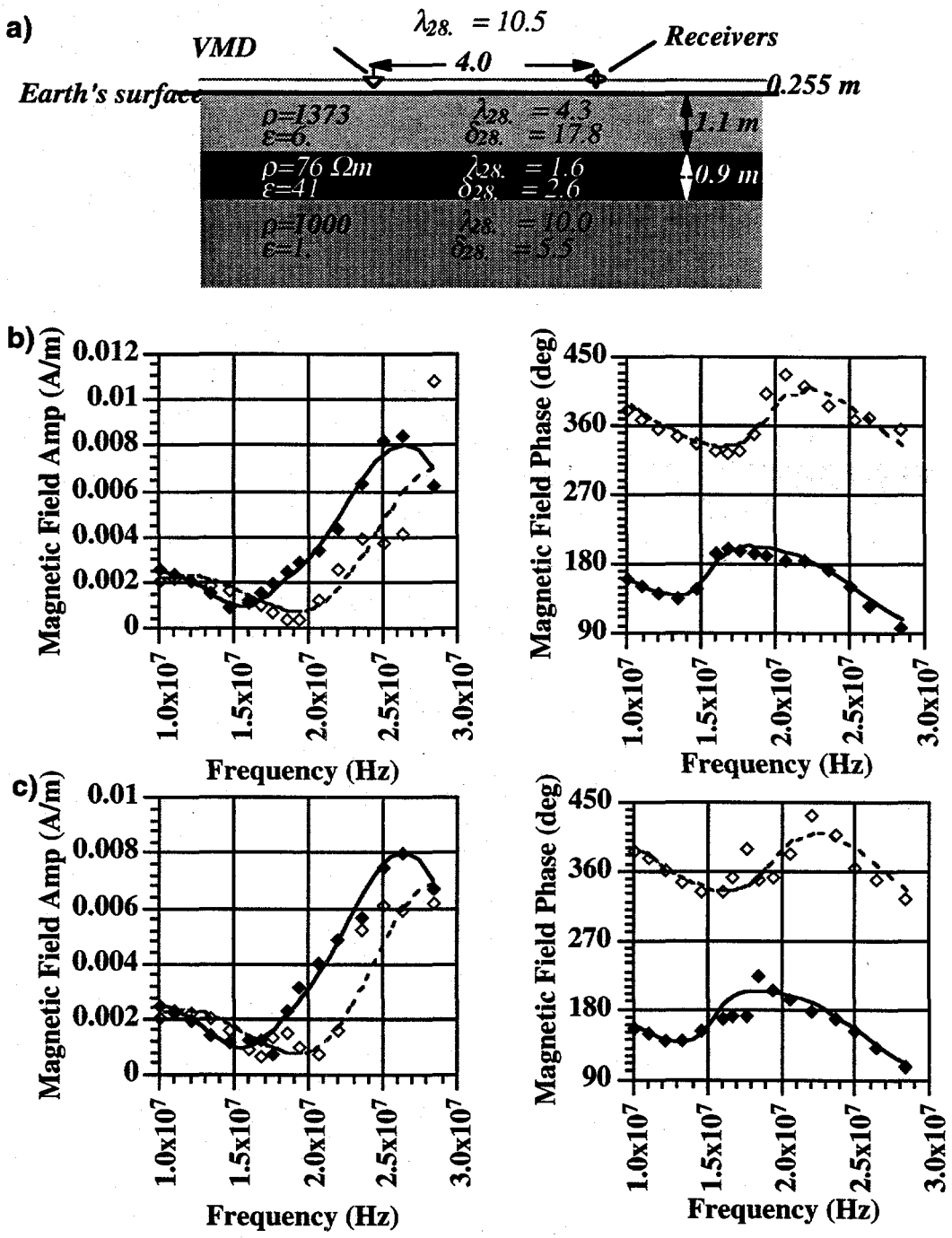


Figure 10 - a) Colorado School of Mines 1-D model. The magnetic permeability in all three layers has been set to that of free space. Unless otherwise noted a 120 x 120 x 120 cell mesh was employed with a maximum cell dimension of 0.15m. The comparisons are between the 3-D finite difference scheme (symbols) and Lee's 1-D solution (lines). b) Horizontal and vertical magnetic field results obtained with no grid stretching. c) Horizontal and vertical magnetic field results obtained with real grid stretching (a = 1.0,b = 0.0) for 25 cells along each boundary.

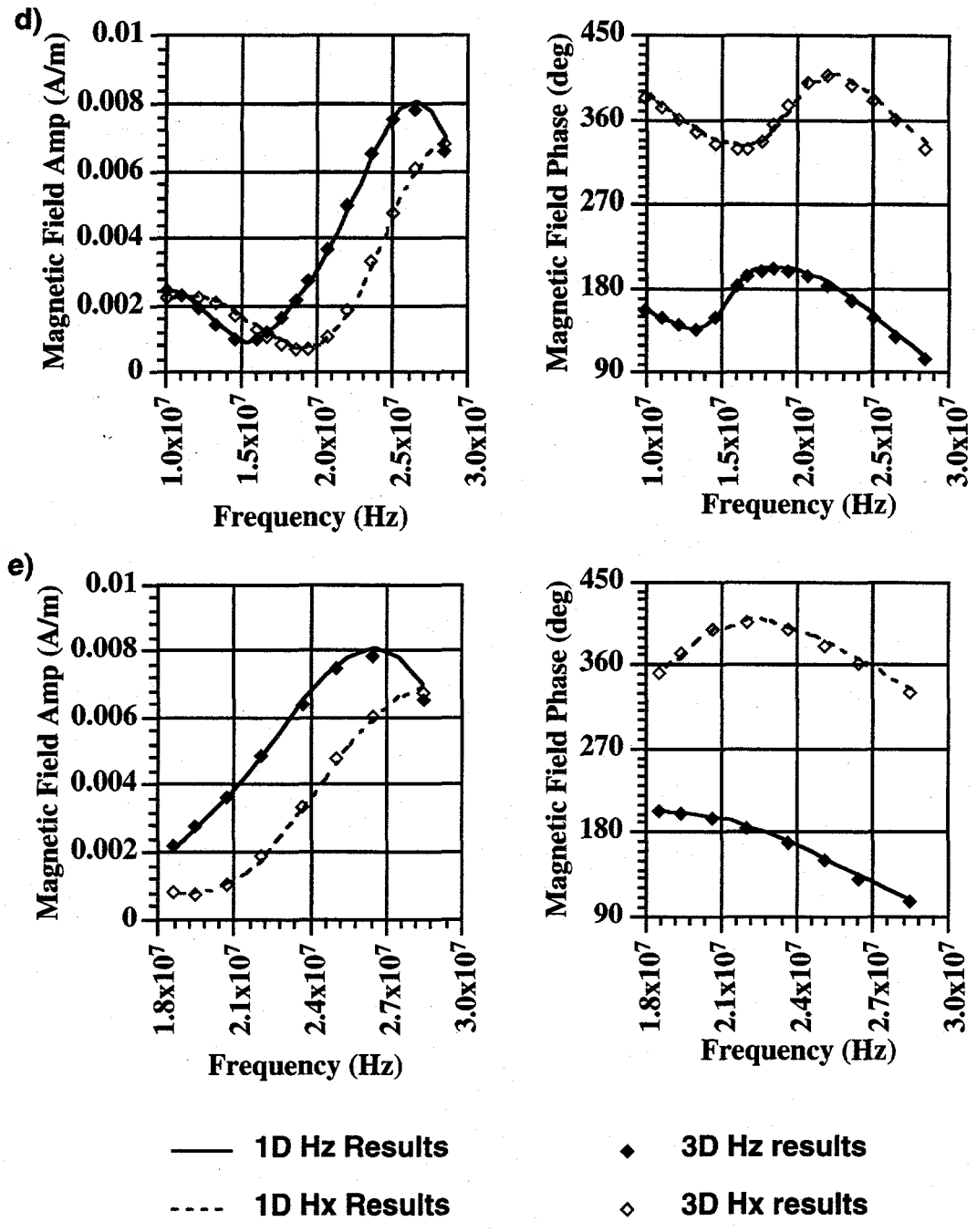


Figure 10 (cont.) d) Horizontal and vertical magnetic field results obtained with complex grid stretching (a = 0.0,b = -0.6) for 25 cells along each boundary. e) Horizontal and vertical magnetic field results obtained on a 72 x 72 x 72 cell mesh with increased complex grid stretching (a = 0.0,b = -2.0) for 10 cells along each boundary.

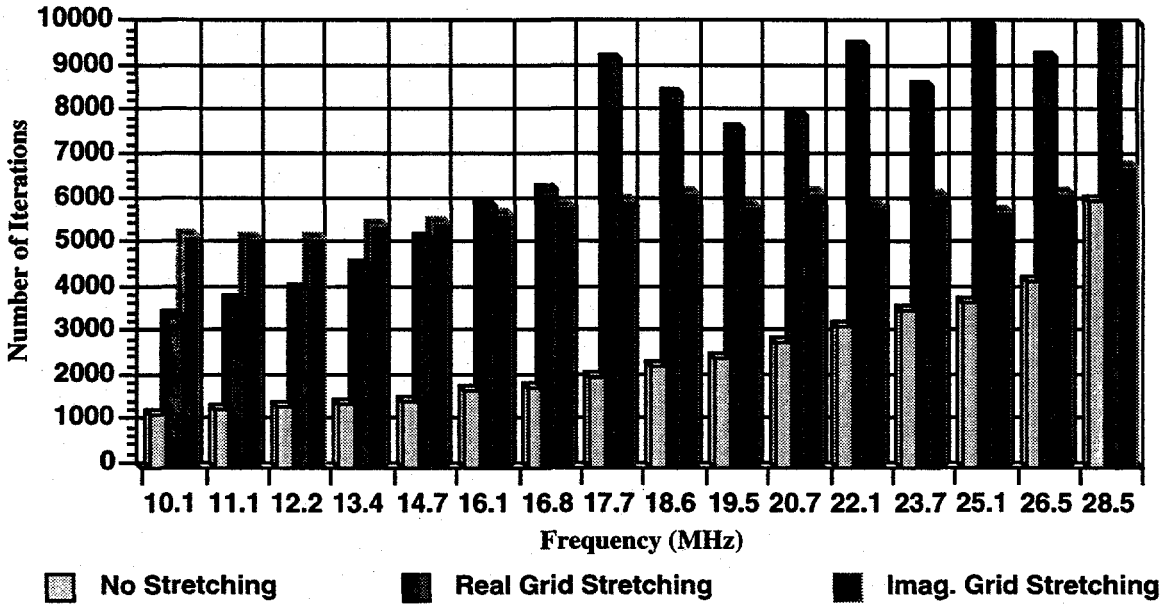


Figure 11 - The solution times of the QMR method for different frequencies and the different grid stretching parameters employed for Figures 10b through 10d.

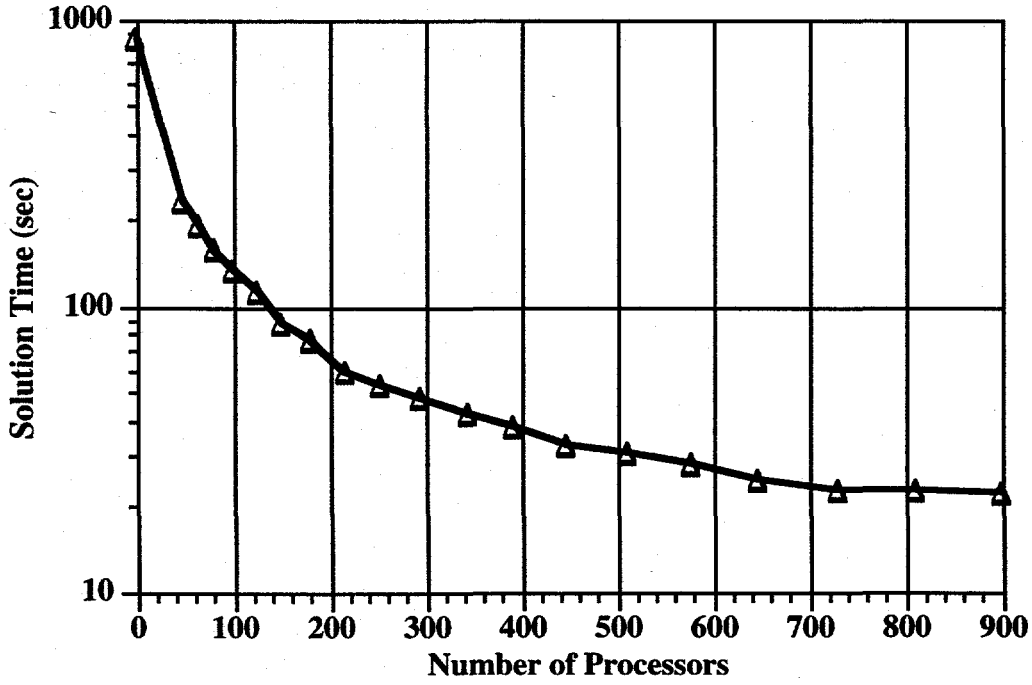


Figure 12 - The solution time versus the number of processors employed on the Intel Paragon for the 7.2 kHz HMD simulation in Figure 4. Note: the result for one processor is for an IBM RS6000-590 workstation.

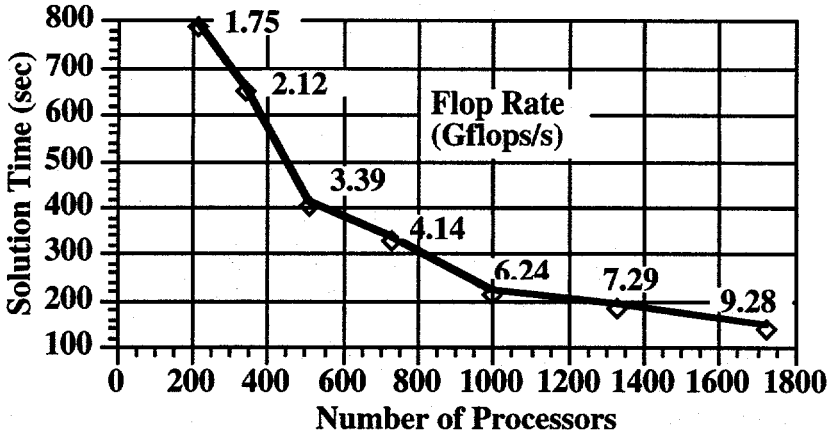


Figure 13 - The solution time and flop rate versus the number of processors employed on the Intel Paragon for the 10.1 MHz simulation plotted in Figure 10d.

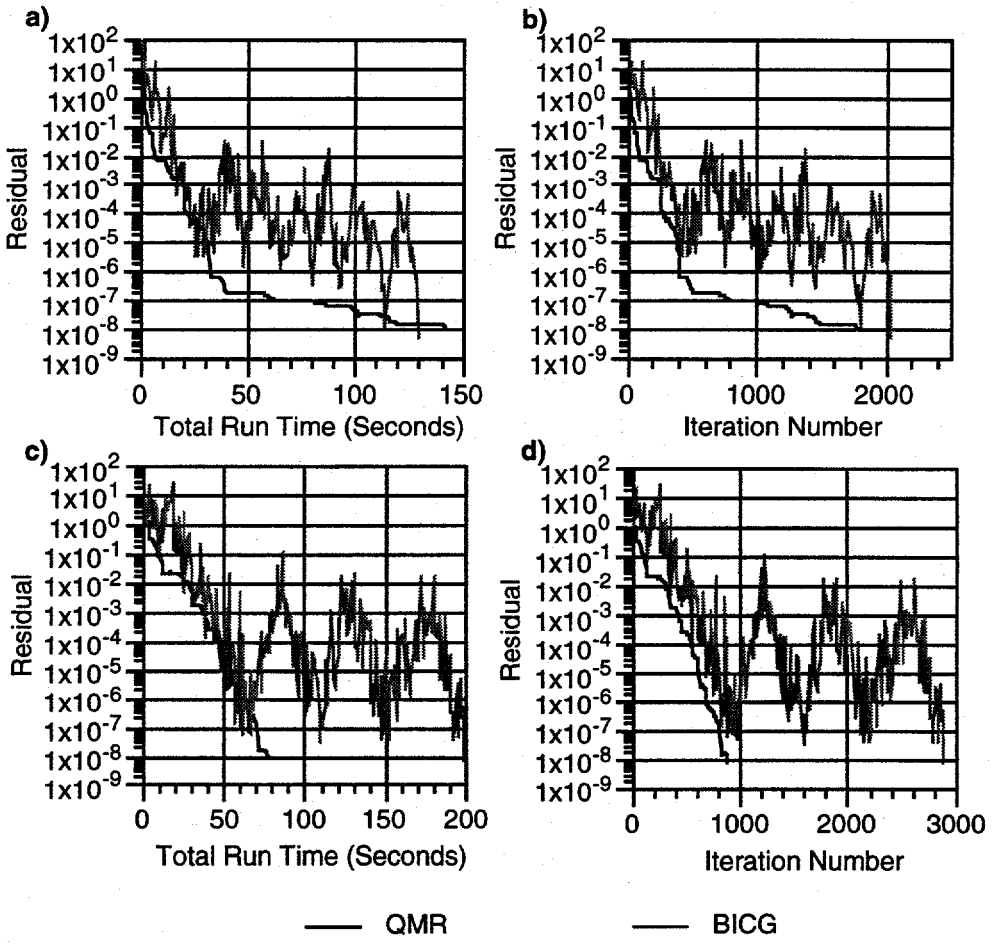


Figure 14 - Convergence of the BICG and QMR methods for the HMD simulation in Figure 4. a) Normalized residual versus run time for 56 kHz simulation. b) Normalized residual versus iteration number for 56 kHz simulation. c) Normalized residual versus run time for 7.2 kHz simulation. b) Normalized residual versus iteration number for 7.2 kHz simulation.

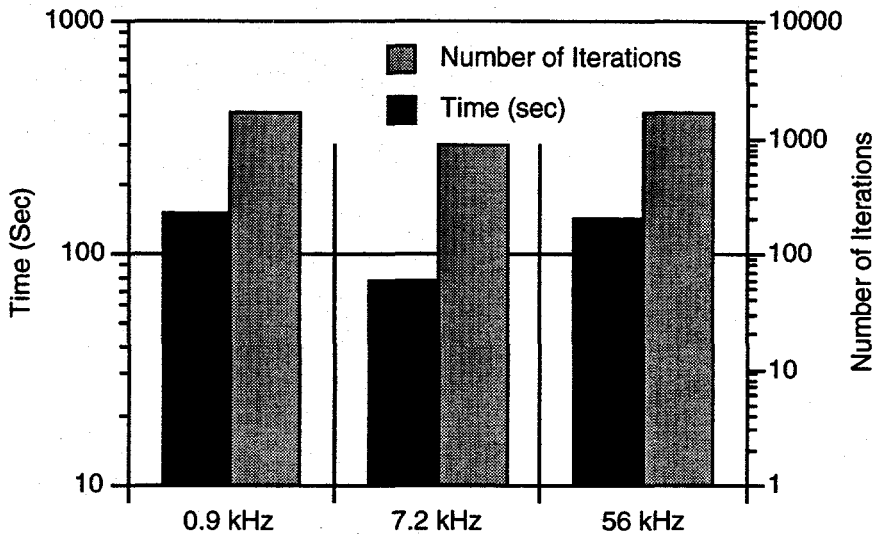


Figure 15 - Time of convergence, and number of iterations needed for convergence of the HMD simulation in Figure 4 for all three frequencies using the QMR solver with Jacobi scaling.

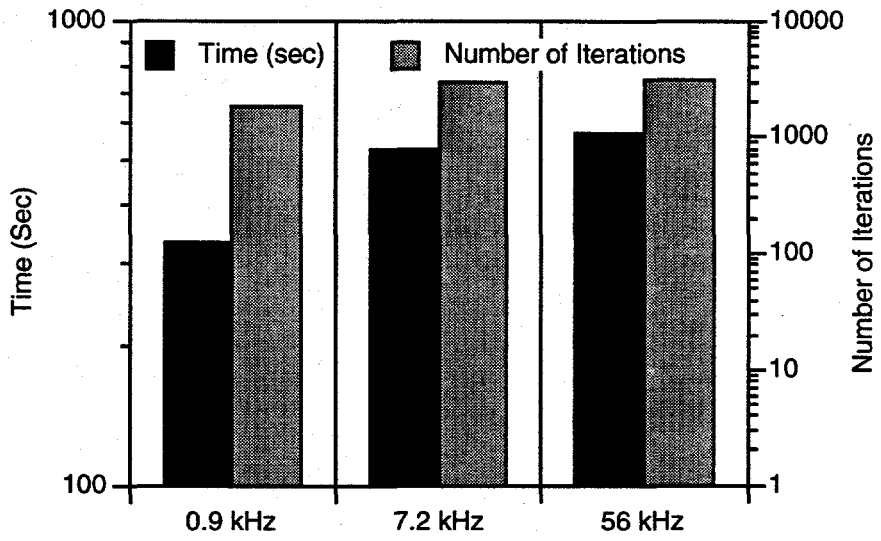


Figure 16 - Time of convergence, and number of iterations needed for convergence of the HMD simulation in Figure 4 for all three frequencies using the QMR solver with Block Jacobi preconditioning.

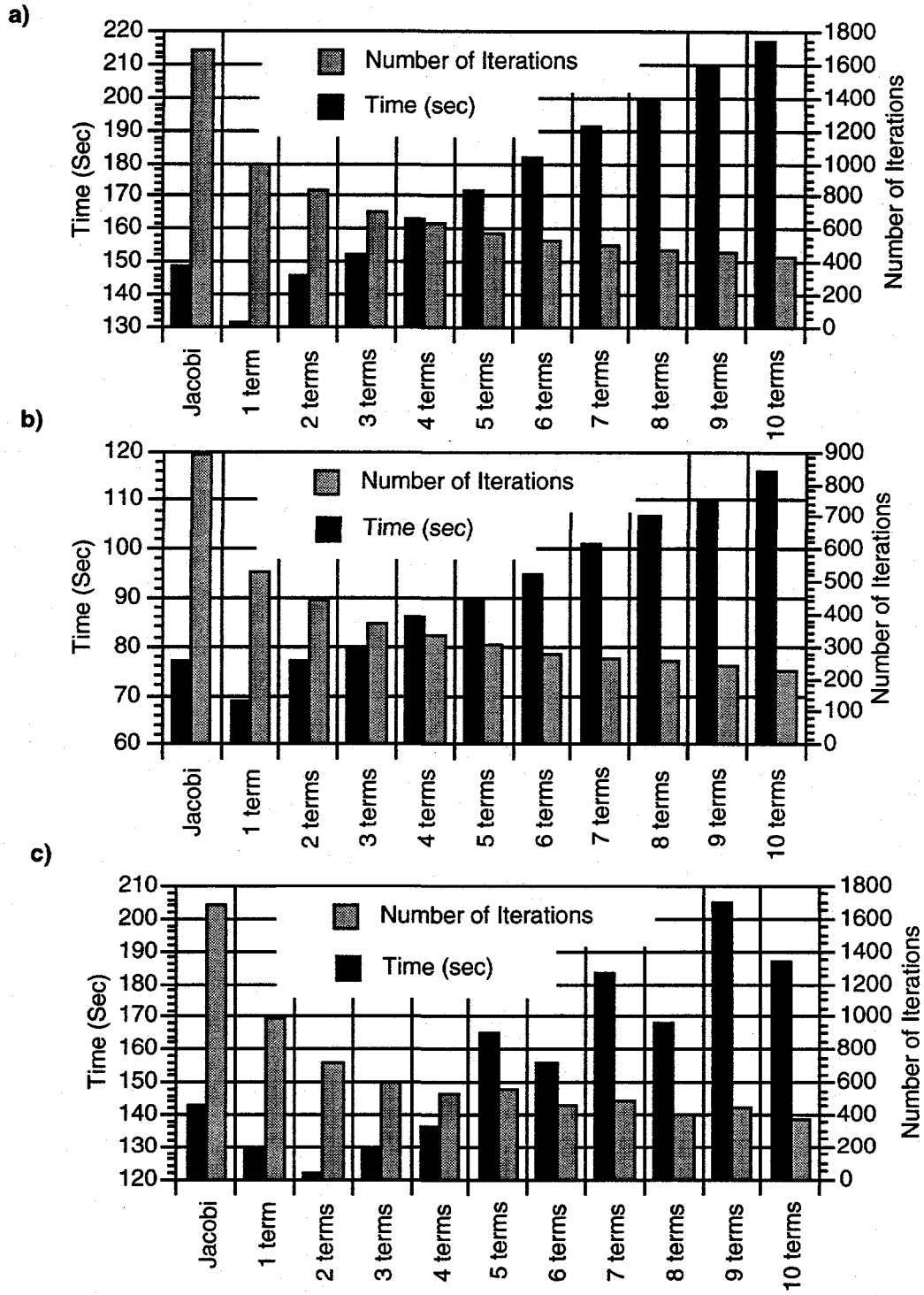


Figure 17 - Time of convergence, and number of iterations needed for convergence of the HMD simulation in Figure 4 using the QMR solver with Neumann polynomial preconditioning. The results are plotted as a function of the number of terms employed in the polynomial with the first entry representing simple Jacobi scaling. a) 0.9 kHz. b) 7.2 kHz. c) 56 kHz.

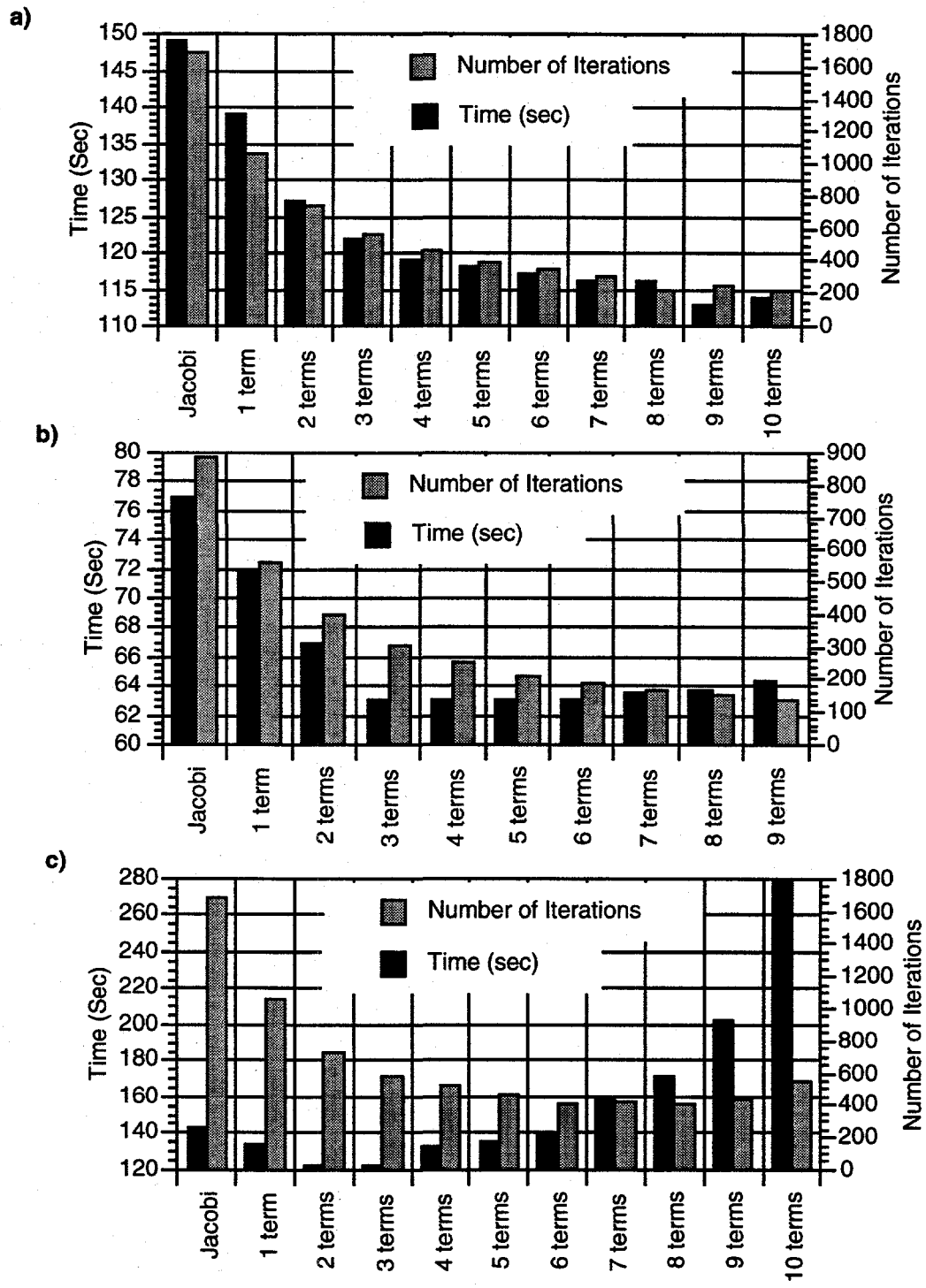


Figure 18 - Time of convergence, and number of iterations needed for convergence of the HMD simulation in Figure 4 using the QMR solver with least squares polynomial preconditioning. The results are plotted as a function of the number of terms employed in the polynomial with the first entry representing simple Jacobi scaling. a) 0.9 kHz. b) 7.2 kHz. c) 56 kHz.

# CHAPTER III

## 3-D MASSIVELY PARALLEL ELECTROMAGNETIC INVERSION -- THEORY

To this point, a complete solution to the 3-D inverse problem has been hindered by insufficient computing resources. Realistic 3-D reconstructions require tens of thousands of unknown electrical parameters to be estimated. This demand coupled with forward modeling overhead, where up to several million field unknowns may need to be calculated to determine model sensitivities and predicted data, make the solution of the 3-D inverse problem non trivial. Attempts to circumvent this difficulty have included the use of quasi-linear approximations in both the forward as well as the inverse modeling (cf. Torres-Verdin and Habashy, 1995 and 1994, Habashy et al., 1995, Zhandnov and Fang, 1995a) and the use of approximate model sensitivities (Farquharson and Oldenburg, 1995). Unfortunately even these approaches suffer when the number of parameters being estimated exceeds several thousand. Only with the advent of massively parallel (MP) computers can a realistic attack to the problem be proposed.

Even with an MP platform one must be careful when implementing a solution to the inverse problem. Foremost is to avoid directly inverting large matrix systems that are either sparse or full. Rigorous modeling of 3-D EM fields can be carried out efficiently using staggered finite differences, which produces a sparse linear system. On an MP platform this system, if properly preconditioned, can be quickly solved using iterative Krylov subspace methods (refer to Chapter II for examples). On the other hand, the solution of the least-squares inverse problem requires dealing with a full linear system. However, since this system satisfies the normal equations it can also be efficiently solved iteratively with conjugate gradient (CG) methods. Mackie and Madden (1993) and Zhang et al. (1995) used this approach to attack the 3-D magnetotelluric (MT) and direct current (DC) inverse problems, respectively, on scalar platforms. Here we will apply the approach to the 3-D EM inverse problem for frequency-domain dipolar source fields, where the source strengths and locations are known. Because the controlled source EM problem is far more computationally demanding than both the DC problem due to its vector nature, and the MT problem due to the sheer number of source fields to be considered (upwards of several hundred), an MP platform is a necessity. As will be demonstrated below such a platform allows large models to be reconstructed, which are not underparameterized, in a reasonable amount of time.

A key consideration in developing any inverse solution is efficient computation of model sensitivities. Because we will solve the inverse problem from an underdetermined point of view, we can efficiently carry out calculations involving model sensitivities using reciprocity, which is known as the adjoint solution to the problem. The use of reciprocity, where the receivers act as sources, can be used to limit forward modeling to the number of the transmitter and receiver positions at a given frequency. The traditional approach requires the number of forward solves to be equal to the number of parameters used in the inverse. When the number of parameters far exceeds the number of transmitters and receivers, the adjoint approach is obviously most efficient (cf. McGillivray and Oldenburg, 1990). In fact using the adjoint approach coupled with the CG solution of the normal equations one can even avoid forming individual components of the model sensitivity matrix, hence resulting in a significant savings of computational memory.

In this chapter we present the theory behind the 3-D inversion scheme, including how the scheme must be modified to run on a parallel computer. Next synthetic data generated by an integral equation code will be inverted. This provides an independent check on the solution as the data are produced by a code that is very different in nature from the finite difference code used in the inversion routine and are thus prone to different numerical errors.

## THE INVERSE SOLUTION

### Regularized Least Squares

As already mentioned the parameterization used in the 3-D inverse solution will be kept sufficiently fine because we are interested in reconstructions that do not under parameterize the earth. This forces the 3-D inverse problem to be underdetermined, which makes it unstable and ill posed. Reliable estimates of the model parameters ($\mathbf{m}$) may be possible if the least squares inversion is stabilized with regularization (Tikhonov and Arsenin, 1977). Regularization removes solutions that are too rough by imposing an additional constraint on the data fit. Reconstructions are required to be smoothed versions of the earth's electrical properties at the expense of an increase in the error between the measured and predicted data.

Linearizing about a given earth model, $\mathbf{m}^{(i)}$, at a given iteration $i$, the following functional can provide smooth reconstructions if it is minimized with respect to the model parameters, $\mathbf{m}$, which can include both the electrical conductivity and dielectric permittivity:

$$S = [(\mathbf{D}((\mathbf{d}-\mathbf{d}^{p(i)})-\mathbf{A}^{p(i)}(\mathbf{m}-\mathbf{m}^{(i)})))^t(\mathbf{D}((\mathbf{d}-\mathbf{d}^{p(i)})-\mathbf{A}^{p(i)}(\mathbf{m}-\mathbf{m}^{(i)}))) - \chi^2] + \lambda(\mathbf{Wm})^t(\mathbf{Wm}). \quad (20)$$

The terms in equation (20) that control how well the data are fit by the model are as follows: 1) the observed data, represented by the vector **d**, 2) the predicted data arising from the reference model $\mathbf{m}^{(i)}$ denoted by $\mathbf{d}^{p(i)}$, 3) a data weighting matrix **D**, which is diagonal and consists of the reciprocal of the data standard deviations, the reciprocal of the data amplitude or in some instances an identity matrix if data weighting is unwarranted, 4) the Jacobian or model sensitivities matrix given by $\mathbf{A}^{p(i)}$ and 5) $\chi^2$ the estimated square-error in the observed data. In addition **t** represents the transpose operator instead of the Hermitian operator because the data, predicted data, data weighting matrix and the Jacobian matrix have been split into real and imaginary parts, where we assume the model parameters, **m**, to be always real valued. The parameters that control model smoothness are 1) the regularization matrix **W**, which consists of a finite difference approximation to the Laplacian ($\nabla^2$) operator and is sparse and 2) the tradeoff parameter $\lambda$, which is used to control the amount of model smoothness in the reconstruction. Its selection requires special care if the inverse solution is to provide acceptable results. Selecting tradeoff parameters that are too small can produce models that are physically unreasonable; although the models produce superior data fits they are unreasonably rough. Selecting tradeoff parameters that are too large produce highly smoothed models, however these models show poor dependence on the data. We shall defer further discussion of this parameter until we discuss the iterative nature of equation (20).

Minimization of equation (20) with respect to **m** yields the model update,

$$\mathbf{m} = [(\mathbf{DA}^{p(i)})^t(\mathbf{DA}^{p(i)}) + \lambda(\mathbf{W})^t(\mathbf{W})]^{-1}(\mathbf{DA}^{p(i)})^t(\mathbf{D}\delta\mathbf{d}^{(i)}) \quad (21)$$

with

$$\delta\mathbf{d}^{(i)} = (\mathbf{d} - \mathbf{d}^{p(i)} + \mathbf{A}^{p(i)}\mathbf{m}^{(i)}). \quad (22)$$

Because negative values of **m** are an admissible solution arising from equation (21), it is advisable that before minimizing equation (20) it should be reformulated so one can invert for the natural logarithm of the parameters instead of the parameters themselves (Appendix D). This

causes the imaged properties to be always positive which is a physical requirement. By using a log parameterization, it is also possible to incorporate a lower bound positivity constraint in the inverse solution.

**Derivation of the Jacobian Matrix Elements**

Deriving a computationally efficient form of the Jacobian matrix elements is critical for a robust inverse solution, since calculation and manipulation of these elements is the bottleneck within the inversion. To derive these elements consider a single predicted data point, $d_j$, defined for a given transmitter-receiver pair as

$$d_j = d^b_j + \mathbf{g}_j^t \mathbf{E}_s. \tag{23}$$

In this equation $d^b_j$ is a field arising from some specified whole space or layered half space background model at location j and $\mathbf{E}_s$ is the scattered electric field vector arising due to 3-D changes within this background. $\mathbf{E}_s$ has dimension of NTx1 and is determined from the finite difference forward solver, (discussed in Chapter II), where NT represents the number of field unknowns. The vector $\mathbf{g}_j^t$ is an interpolator vector for the jth measurement point and is of dimension 1xNT. This vector will interpolate fields on a staggered grid to the measurement point and can also be used to numerically approximate magnetic field measurements through the curl of the electric field. With this definition an element of the Jacobian matrix is written as

$$\partial d_j/\partial m_k = \mathbf{g}_j^t \, \partial \mathbf{E}_s/\partial m_k. \tag{24}$$

From the forward problem the scattered electric fields are determined from the linear system,

$$\mathbf{K}\mathbf{E}_s = \mathbf{s}, \tag{25}$$

where $\mathbf{K}$ is the sparse finite-difference stiffness matrix with 13 non-zero entries per row and depends linearly on the electrical parameters we desire to estimate. Because the forward problem is formulated for the scattered fields, the source vector, s, for a given transmitter also depends linearly on the model parameters. It is related to the difference between the model parameters

and the background model, weighted by the background electric field, $\mathbf{E}^b$; refer to Chapter II for the details. Thus differentiating equation (25) with respect to $m_k$ yields,

$$\partial \mathbf{E}_s/\partial m_k = \mathbf{K}^{-1}(\partial \mathbf{s}/\partial m_k - \partial \mathbf{K}/\partial m_k \mathbf{E}_s), \tag{26}$$

and an element of the Jacobian matrix in complex form can be written as

$$\partial d_j/\partial m_k = \mathbf{g}_j^t \mathbf{K}^{-1}(\partial \mathbf{s}/\partial m_k - \partial \mathbf{K}/\partial m_k \mathbf{E}_s). \tag{27}$$

**Model Step via Conjugate Gradients**

As the number of unknowns increases beyond several thousand, using direct matrix inversion to compute the updated model, **m**, in equation (21) is not feasible, even with an MP platform. Instead we opt for an iterative solution. Since equation (20) satisfies the normal equations, the conjugate gradient method of Hestenes and Stiefel (1952) can be used to get the solution. This method offers a benefit over direct inversion in two ways: 1) following Mackie and Madden (1993) and Zhang et al., (1995) it is possible to avoid explicitly forming the Jacobian Matrix, $\mathbf{A}^{p(i)}$ and its transpose altogether, thus saving considerable computer storage, and 2) as the number of unknowns, n, increases the solution for direct inverse goes as $n^3$ compared to $n^2$ with the iterative approach. Finally, it is much easier to implement a CG routine on a parallel platform when compared to a full matrix inversion.

In the conjugate gradient method all one needs is one matrix-vector multiply per relaxation step. However, because the matrix given by this operation is $[(\mathbf{DA}^{p(i)})^t (\mathbf{DA}^{p(i)}) + \lambda(\mathbf{W})^t(\mathbf{W})]$, there are several other matrix-vector multiplies to be considered. First, the matrix product of $(\mathbf{DA}^{p(i)})^t$ with $\mathbf{DA}^{p(i)}$, requires two matrix-vector multiplies. In addition the regularization-matrix product with its transpose requires two more matrix-vector multiplies. Since the latter matrix-vector multiplies are easy to implement and compute, no further elaboration will be given to them until the MP implementation of the 3-D inverse.

For the Jacobian matrix-vector multiplies, $\mathbf{DA}^{p(i)}$ and $(\mathbf{DA}^{p(i)})^t$, we have

$$\mathbf{y} = \mathbf{DA}^{p(i)}\mathbf{u} \tag{28}$$

and

$$\mathbf{z} = (\mathbf{DA}^{p(i)})^t \mathbf{y}, \tag{29}$$

where **u** is an arbitrary real vector, known as a CG search direction vector. The vectors **y** and **z** are also assumed to be real in the above expressions. We now determine compact and computationally efficient forms for the two matrix vector multiplies. These forms will also be used to treat the matrix-vector multiplies given in equations (21) and (22), i.e. $\mathbf{A}^{p(i)}\mathbf{m}^{(i)}$ and $(\mathbf{DA}^{p(i)})^t (\mathbf{D}\delta\mathbf{d}^{(i)})$, which are needed to initialize the CG solver at each iteration of the inversion. For compact expressions, let the vector **y** in equation (29), the observed and predicted data, as well as the data weighting matrix be redefined as complex. Using the results from Appendix E and equation (28), we have for the jth element of the first matrix vector multiply

$$y_j = \text{Cmplx}\Big(\text{Re}\Big(\mathbf{g}_j^t \mathbf{K}^{-1} \sum_{k=1}^{M} u_k(\partial \mathbf{s}/\partial m_k - \partial \mathbf{K}/\partial m_k \mathbf{E}_s)\Big)\text{Re}(D_{jj}),$$

$$\text{Im}\Big(\mathbf{g}_j^t \mathbf{K}^{-1} \sum_{k=1}^{M} u_k(\partial \mathbf{s}/\partial m_k - \partial \mathbf{K}/\partial m_k \mathbf{E}_s)\Big)\text{Im}(D_{jj})\Big), \tag{30}$$

where M is the total number of parameters to be estimated and $D_{jj}$ is the jth diagonal entry of the matrix **D**. $\mathbf{E}_s$ here denotes the scattered electric field arising from a given transmitter at a specific frequency used to determine the model sensitivities and predicted data at location j. Using the same approach one can also show that for the second matrix-vector multiply

$$z_k = \text{Re}\Big(\sum_{j=1}^{N} \text{Cmplx}(\text{Re}(D_{jj})\,\text{Re}(y_j), \text{Im}(D_{jj})\,\text{Im}(y_j))^* \mathbf{g}_i^t \mathbf{K}^{-1} (\partial \mathbf{s}/\partial m_k - \partial \mathbf{K}/\partial m_k \mathbf{E}_s)\Big), \tag{31}$$

where N is the number of complex data points used in the inversion and the symbol '*' stands for complex conjugation. Note that even though the summation in equation (31) is over all the data points, parts of the sum could be over different transmitters and/or frequencies, hence $\mathbf{E}_s$ will change. Lastly, the derivatives $\partial \mathbf{s}/\partial m_k$ and $\partial \mathbf{K}/\partial m_k$ in equations (30) and (31) are rapid to

compute analytically; it is shown in Appendix F that the vector $\partial s/\partial m_k$ and matrix $\partial \mathbf{K}/\partial m_k$ each have 12 non-zero entries when $m_k$ represents either the conductivity or permittivity.

In addition to the forward solves necessary to determine $\mathbf{E}_s$ for each source, the matrix-vector multiplies in equations (30) and (31) require solving a series of forward problems corresponding to the total number of unique data measurements locations, where

$$\mathbf{v}_j^t = \mathbf{g}_j^t \mathbf{K}^{-1}, \tag{32}$$

or since $\mathbf{K}^t = \mathbf{K}$ (refer to Chapter II),

$$\mathbf{K}\mathbf{v}_j = \mathbf{g}_j \tag{33}$$

(note: The fact that $\mathbf{K}$ is symmetric is simply a statement of reciprocity). A unique measurement location comprises the measurement of a specific field component made at a site. Thus the total number of forward solves needed for each model update is given by $N_{tx} + N_{rx}$, where $N_{tx}$ and $N_{rx}$ are the total number of transmitters and unique receiver positions used in the inversion.

Handling the Jacobian matrix-vector multiplies in this manner is much more efficient then attempting to explicitly solve equation (26) and using the results to form the matrix-vector multiplies. For example if we are estimating over 30,000 parameters, this would require 30,000 separate forward solves which is impractical. On the other hand because the amount of data used in the inversion is limited, we anticipate no more than several thousand forward solves per model update. Limiting the number of forward solves has also been recommended by McGillivray and Oldenburg (1990) and Oldenburg (1990) because of its efficiency and has been used by Park (1983), Mackie and Madden (1993) and Zhang et al. (1995) in their constructions of the inverse solution.

**An Iterative Solution and Selecting the Tradeoff Parameter**

Because of the computational cost of using an exact forward solution in the inversion we do not have the luxury of slowly reducing the tradeoff parameter or determining an optimal tradeoff parameter at a given iteration to insure against arbitrarily rough models. However, experience indicates that smooth models can be produced with the strategy we are now going

to discuss.

We initiate an inversion assuming an initial background model, where we compute the predicted data for all transmitter locations. At the first iteration we use our scheme to efficiently determine the matrix-vector multiplies in the CG algorithm and determine the model update via equation (21). This model is determined once the tradeoff parameter, $\lambda$, is selected. To assure a smoothed solution at the first iteration, we select the tradeoff parameter as

$$\lambda = \text{Max Row Sum}(\mathbf{DA}^{p(i)} [\mathbf{DA}^{p(i)}]^t)/2^{(i-1)}, \tag{34}$$

where i=1 for the first iteration. We have selected this method of choosing $\lambda$ because it is an estimate of the largest eigenvalue of the non-regularized least squares system matrix. Thus weighting $(\mathbf{W})^t(\mathbf{W})$ by this amount allows only the largest eigenvalues to influence the solution. The maximum row sum is easy to compute and follows from equations (28) and (29) with $\mathbf{u}$ selected to be the unit vector.

To digress for the moment, we note that the CG method is designed for linear systems that are symmetric positive definite. While the normal equations in equation (21) are symmetric, both $(\mathbf{DA}^{p(i)})^t (\mathbf{DA}^{p(i)})$ and $(\mathbf{W})^t(\mathbf{W})$ posses a zero eigenvalue. Thus it appears that the matrix describing the normal equations may be semi-definite. However when $(\mathbf{DA}^{p(i)})^t (\mathbf{DA}^{p(i)})$ and $(\mathbf{W})^t(\mathbf{W})$ are summed as $(\mathbf{DA}^{p(i)})^t (\mathbf{DA}^{p(i)}) + \lambda(\mathbf{W})^t(\mathbf{W})$, experience shows the CG algorithm converges provided the tradeoff parameter is reasonably selected. One must avoid selecting $\lambda$ too large such that non zero elements of $(\mathbf{W})^t(\mathbf{W})$ are much greater than the corresponding elements of $(\mathbf{DA}^{p(i)})^t (\mathbf{DA}^{p(i)})$ as this will cause a degradation of the convergence rate within the CG algorithm.

We proceed to the next iteration if the data error (sum of square errors) is above $\chi^2$. If this is true the model is linearized again about the new model $\mathbf{m}$, new predicted data and electric fields are computed from the updated background model, and the new model update determined with the tradeoff parameter specified with equation (34). In general we have found that for the first few iterations this method of selecting the tradeoff parameter reduces the error by about a factor of 2. The iterative procedure, just outlined, is continued until the data error matches $\chi^2$, convergence of the data error occurs, or a pre specified number of iterations has taken place.

Even with this procedure, it is possible to drive the tradeoff parameter down too quickly,

especially when one attempts to fit the data to an unrealistic noise level or uses an excessive number of iterations. However, it has been our experience that if the tradeoff parameter is not relaxed sufficiently the inversion can stall out far above the estimated noise level in the data. Our solution to this difficulty is to have a good estimate of the data noise, and monitor the tradeoff parameter and squared error in the inversion. If excessive model structure is being incorporated into the image, or if the inversion is over fitting the data, we stop the inversion and relaunch it using an acceptable reconstruction and tradeoff parameter at some previous iteration. After this restart, the tradeoff parameter is kept fixed for the rest of the inversion. In addition, we may change the data weighting scheme if it is decided that bad data are weighted too large or good data too little. While this strategy is somewhat subjective, it has yielded acceptable results.

At each iteration we restrict the number of relaxation steps in the CG routine since only a modest number of steps are sufficient to produce an accurate model update, especially during the early stages of the scheme (Zhang et al., 1995). For the first and second iterations, 20 and 40 relaxation steps are used, respectively. Subsequent iterations use 60 steps.

## MASSIVELY PARALLEL IMPLEMENTATION

EM inversion in 3-D can easily require the solution of at least several hundred forward solves per iteration. In Chapter II we demonstrate how these forward solves can be efficiently computed on an MP machine, where each solve could constitute over five million field unknowns. A significant portion of the storage required to preform the inversion is taken up by the electric field solution vectors produced by these solves and are needed to complete matrix-vector multiplies in the CG routine. Fortunately on the 1840 node Intel Paragon at Sandia National Laboratories it is possible to execute and store all solves without writing to disk; the Paragon has approximately 30 Gbytes of accessible memory.

As determined in Chapter II, the most efficient use of the processors is to divide the problem as close to an equal number of unknowns for which to solve. Because each processor needs only to make calculations for a subset of the forward and inverse problems, and because the processors are making their calculations in parallel, the solution time is reduced by a factor which is approximately equal to the number of processors employed.

The parallelization of the inverse problem is achieved by assigning a given number of

processors in each direction of the forward modeling domain (nx in x, ny in y and nz in z). Hence the number of processors dedicated to the problem is determined by nx*ny*nz. The actual estimation of the earth's electrical properties is carried out on the same sets of processors dedicated to the forward problem, with all the processors sharing the same data, but storing different parts of the inversion and forward modeling domain. However, it is possible that some of the processors may not contain portions of the inversion domain and thus will be idle during the CG solve. The reason for this is that cells outside the inversion domain are necessary to keep the boundary of the forward modeling domain at distance (Figure 19). We desire parameter estimates that are not adversely affected by grid truncation errors in the forward modeling.

We now need to address the manner in which the model is input into the parallel machine. The input could constitute a starting model needed to launch the inverse or a restart model in the event of a system crash or if excessive model structure was being incorporated in the inversion. To accomplish this input, we have decomposed the data into two different sets, a global data set and a local data set as in Chapter II.

Communication or message passing amongst the processors will be needed to complete calculations in the inverse problem as well as for the forward problem. Communication amongst processors consists of both the global and local variety. Global communication will be required to treat the five dot products within a generic CG routine and an additional one in equation (30). On the other hand, calculations involving the matrix-vector multiplies require local communication.

Within the inversion three types of local communication will be needed. The first will involve communication of electric field values on processor boundaries such that matrix-vector products in equations (30) and (31) can be completed. This communication will occur before the CG routine is called for efficiency. The second type of communication will involve matrix-vector products of the CG search direction vectors with the regularization matrix times its transpose. This occurs within the CG routine at every relaxation step because 1) we have explicitly formulated the regularization matrix and 2) the CG vectors are constantly updated. The final type of communication occurs after exiting the CG routine. Electrical properties of cells along processor boundaries must be communicated with neighboring processors for proper averaging of electrical properties at cell edges; these averages are needed in subsequent forward-model calculations. After this message passing, calculations with the forward solver can proceed with

the next iteration, given the convergence criteria outlined above.

To deduce the communication pattern of the first type, consider eight nodes located at the corners of a cell whose properties we wish to estimate (Figure 20). Consider the simplest case where each processor is in charge of only one node and cell. For example, node (i,j,k) has the cell in Figure 20 assigned to it as well as the three components of the electric field at (i+½,j,k), (i,j+½,k,) and (i,j,k+½). To complete its calculations, the processor that owns this node and cell also needs the electric fields on the cell edges assigned to other nodes on different processors. These processors will thus need to supply the field components. Furthermore the processor that owns the node (i,j,k) may also have to send its electric field components to nodes on other processors. For example, node (i-1,j,k) will require the y component of electric field assigned to node (i,j,k).

The pattern for the second type of communication can be obtained from Figure 21. The stencil shows the required coupling between the center cell and its neighbors arising from the Laplacian operator, as applied in the regularization matrix-vector multiplies. Again consider the case where each processor contains only a single cell. To complete its local version of the matrix-vector multiply, the center processor needs components of the CG search direction vector which are assigned to the other cells and hence processors. In addition to this, the processor holding the center cell will also be required to send components to the neighboring processors so that they can complete their corresponding computations.

From Figure 22 the final communication pattern can be inferred. Consider the computation of the average electrical properties at cell edges (i+½,j,k), (i,j+½,k) and (i,j,k+½), which are assigned to node (i,j,k). The electrical properties of the four cells that form each edge will be needed and the computation at these positions will be carried out on the processor that holds the solid cell also assigned to node (i,j,k); additional cells that are required are indicated by the dashed outlines. Let us now consider that each node, cell, and its associated electrical properties belong to a different processor. Since the dashed cells belong to different processors, their electrical properties need to be passed to the processor (indicated by solid cell) that will compute the averages. In addition this processor will be required to send its electrical properties. Consider computing average electrical properties at location (i+½,j+1,k). Since this computation is carried out on a different processor, the electrical properties assigned to the solid cell in Figure 22 will be needed.

The local communication pattern for the inverse problem can now be summarized in Figure 23, where each cube represents a different processor with subsets of nodes and cells assigned to it. For the matrix-vector multiplies involving the Jacobian matrix and its transpose, communication consists along the faces of processors as well as along edges. Specifically information is passed from the central processor (marked by the heavy outline) to those neighbors that are dashed in Figure 23. Likewise those neighboring processors with solid boundaries pass information to the central processor. Local communication for multiplies with the regularization matrix and its transpose involve only communication along processor faces in Figure 23, where all the processors send the required elements of the CG vectors to the central processor as well as receive from it. Finally, the communication needed for averaging electrical properties of the cells at adjacent processor boundaries is an opposite sense compared with the communication of the Jacobian matrix vector multiplies. Those face and edge processors marked with a dashed outline send to the central processor, while those that are solid receive information from it. To provide for the required message passing we have chosen as in Chapter II to employ Massage Passing Interface (MPI, Skjellum et al., 1993), instead of using machine specific commands.

As previously mentioned the solution time will decrease with the number of processors employed. This is demonstrated in Figure 24 for an example described in Chapter IV of this report. A significant speed up is observed starting from eighty processors for a single iteration of the inverse algorithm. However as the number of processors continue to increase inter-processor communication becomes more of a factor, resulting in an asymptotic behavior in the solution time with increasing number of processors. Here the amount of message passing will eventually limit the speed at which the computation can proceed. Put simply, increased message passing implies more time communicating and less time computing. Thus optimal use of the machine may entail running the example in Figure 24 using 200 processors and launching several of such jobs simultaneously. On the other hand, if turn around time is an issue, then one would want to operate near the far right end of the curve.

## SYNTHETIC EXAMPLE

Figure 25 shows two different perspectives of a model used to test the 3-D inverse. The data from this model were generated from the integral equation solution of Newman et al. (1986)

and provides a stronger check on the inversion scheme than using data generated by the staggered finite difference code; using data generated with the same forward code as embedded in the inverse will be prone to the same numerical errors and thus will not be fully independent. The test model consists of a 0.2 S/m cube, 50 m on a side, residing in a 0.005 S/m background. Eight wells surround the target, with 15 vertical magnetic dipole (VMD) transmitters at 10 m intervals straddling the target. The vertical magnetic fields were calculated in all other wells at 10 m intervals, excluding the transmitter well. Because the frequency of excitation used in this test is only 20 KHz, the dielectric properties of the target and host are not important in the simulation and only the conductivity properties need be estimated; the magnetic permeability is assumed constant throughout the model and set to that of free space. Gaussian noise equal to two percent of the data amplitude was added to the data set. The data were then weighted by this percentage before inversion. In total, the data consist of 12 600 transmitter-receiver pairs.

The inversion domain consists of 29 791 cells, but only 13 824 cells are shown in the interwell region in Figures 25 and 26; cells outside this region are used to keep the boundary of the inversion domain at distance so as to not affect the conductivity estimates within the interwell region. The inversion, which was launched assuming a 0.005 S/m whole space, has recovered fairly well the location and geometry of the cube, but a smeared version of its conductivity within the cube boundary; the estimates vary from 0.1 to 1.0 S/m. The conductivity estimates of the background range as low as 0.0016 S/m. It has been our experience that improved resolution of the background and cube can be obtained by tightening the lower bound positivity constraint. In this example, the conductivity estimates were restricted to be greater than 0.001 S/m.

Eleven iterations were needed to obtain this reconstruction, where the reduction in relative error against iteration count is illustrated in Figure 27. Assuming Gaussian noise with zero mean, the inversion is assumed to have converged when the relative error approaches the value of one. Because the final error level is still above one in Figure 27 this might suggest that more information could be extracted from the data. However, we ascribe the final error level to originate from bias in the data. These data were produced from a forward modeling algorithm that is different from the one used in the inverse. Finally the processing time needed to produce the image in Figure 26 was approximately 24 hours on the Paragon, with 512 processors utilized.

## DISCUSSION

The MP inversion scheme we have presented has been demonstrated on a data set that would be impossible to invert on scalar workstation platforms due to memory and processor speeds (refer to Chapter IV for additional examples). An important question to ask is what is the largest model the MP inversion can handle? Certainly the maximum model size (both forward and inverse) will be related to the number of transmitters and receivers specified in the data set because this will determine the number of electric field vectors, $\mathbf{E}_s$, that need to be computed and stored. Given the maximum memory on the Intel Paragon of 16 Mbytes per processor, and considering a problem divided amongst 1728 processors (this corresponds to 12 processors assigned along each coordinate direction), Table 2 illustrates a range of problem sizes that can be effectively handled. If $120^3$ nodes are used to describe the forward and inverse modeling domain, the number of transmitters and receivers that can be used is 700. To increase the number of transmitters and receivers it appears necessary to reduce the number of nodes.

| **Problem Size(Nodes):** | $\mathbf{120^3}$ | $\mathbf{96^3}$ | $\mathbf{72^3}$ |
|---|---|---|---|
| **#Tx's and Rx's:** | **700** | **1300** | **3000** |

Table 2. Maximum problem size that can be treated by the Intel Paragon assuming 1728 processors. Problem size is determined by the number of nodes or cells used in the forward modeling and inversion and the number of transmitters (Tx's) and unique receivers (Rx's) specifying a data set. Each Tx and Rx position is for a unique frequency.

One way to increase the size of inverse problems that can be tackled is to skeletonize the inversion domain, but retain the same parameterization level in the forward modeling domain. The key idea here is to reduce the storage of the electric field vectors needed in the inverse. For a given source, the electric field and predicted data are computed at the parameterization level specified in the forward modeling. The electric field is then interpolated to the skeletonized grid corresponding to the inverse and stored in memory. Hence the forward modeling accuracy is still retained in the inverse. Note that the coarser grid can still produce smooth images since it can

involve tens of thousands to hundreds of thousands of cells.

The skeletonized electric field vectors allow for the number of transmitters and receivers to increase dramatically. Consider a problem where the inversion grid is eight times coarser than the forward modeling grid. If $120^3$ nodes are used in the forward calculations, the skeletonized inversion grid, which still comprises 216 000 cells, allows for the number of transmitters and receivers to increase from 700 to over 3000.

## CONCLUSIONS

A 3-D EM inversion code has been successfully implemented and tested on an MP platform. Reasonable, overnight to full day processing times have been obtained. Because of the MP platform, reconstructions have been produced that do not underparameterize the earth; these are reconstructions that involve tens of thousands of cells. Since the 3-D MP inverse also includes rigorous 3-D forward modeling for computing model sensitivities and predicted data, it is our hope that this solution will also serve as an accuracy benchmark on approximate inverse methods now being implemented on workstation platforms (cf. Torres-Verdin and Habashy, 1995 and 1994; Zhandnov and Fang, 1995a; Habashy et al., 1995; Farquharson and Oldenburg, 1995).

In this chapter, we have presented the theory and demonstrated the 3-D inversion capability on synthetic data. Because the ultimate goal of any inversion scheme is to use it to image field data, in Chapter IV we demonstrate how this scheme can be used to design a 3-D crosswell survey and invert a crosswell data set collected at the Richmond field station north of Berkeley California. Images before and after the injection of a salt water plume will be compared to determine the location of the injected plume. In addition, we will also show how the scheme can be employed to analyze the reliability of the images as well as the accuracy and errors in the data.

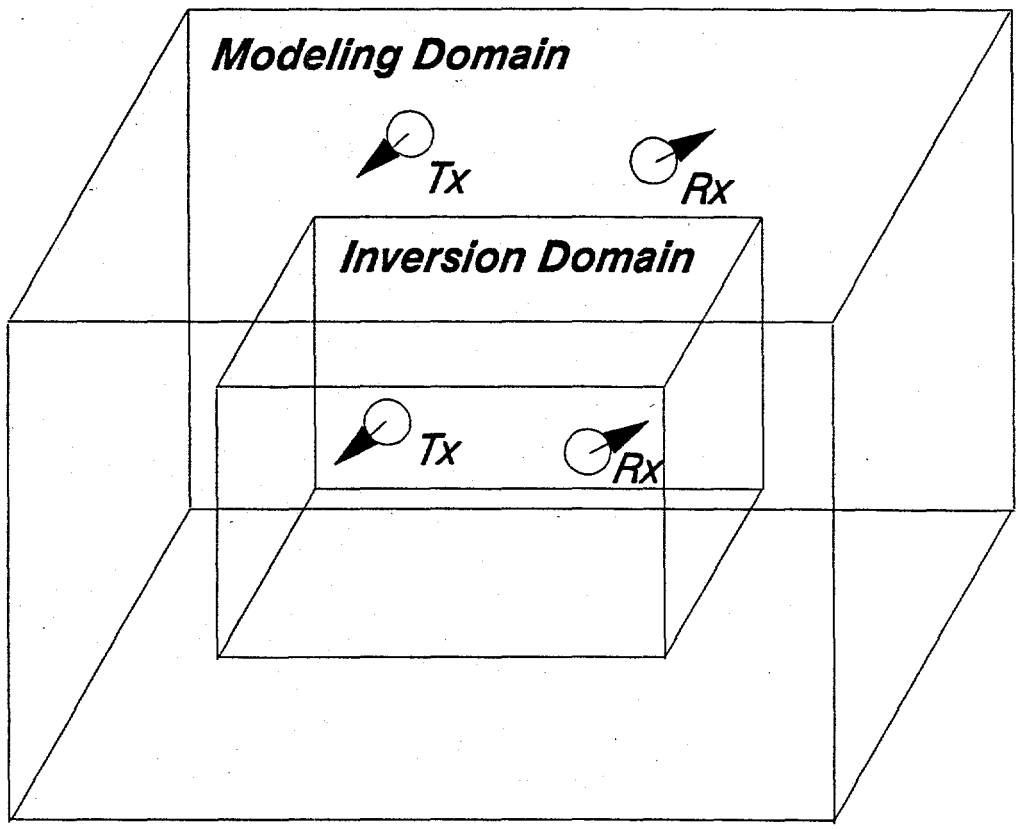


Figure 19. The inversion domain is a subset of the forward modeling domain because of forward-modeling errors near grid boundaries. Transmitters and receivers can be placed either inside or outside the inversion domain. External transmitters and receivers could correspond to surface or airborne configurations, while internal sources and receivers could correspond to cross-well configurations.

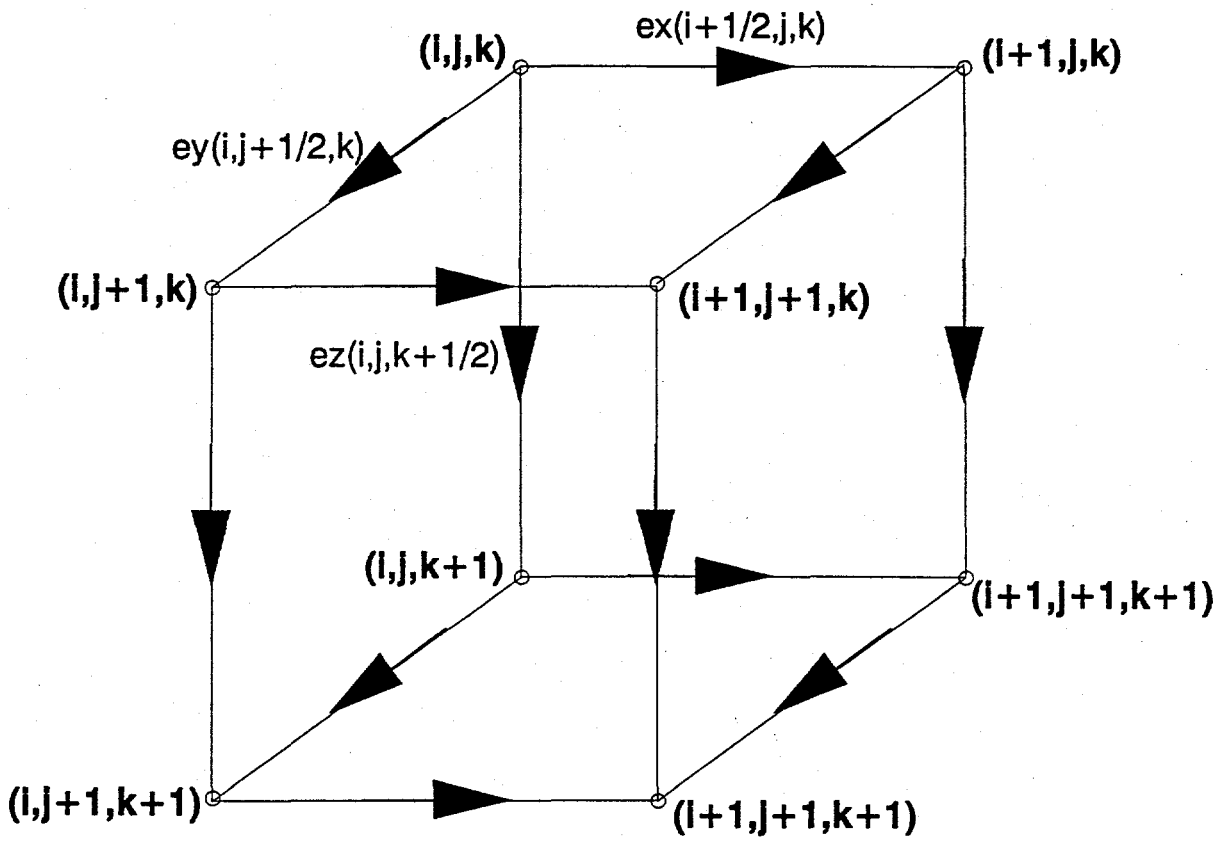


Figure 20. The electric field stencil needed to complete the Jacobian matrix-vector multiplies in the inverse for a single cell. Node (i,j,k) has the cell and the x, y and z electric field components assigned at (i+½,j,k), (i,j+½,k) and (i,j,k+½), respectively. Assignment of other electric field components to other nodes as shown in the figure follows analogously. Using results for the single cell, a processor map can be developed to carry out the required local communication amongst the processors.

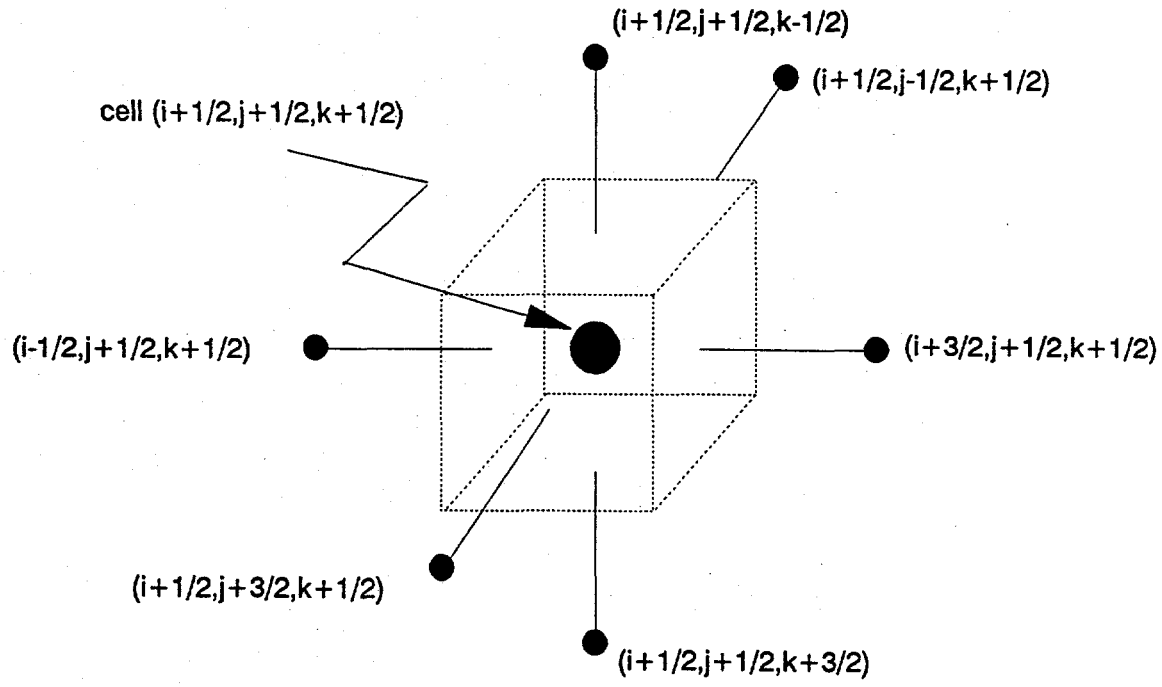


Figure 21. The stencil needed to complete local regularization matrix-vector multiples in the CG routine. Using results for the single cell assigned to a single processor, a processor map can be developed to carry out the required local communication amongst processors.

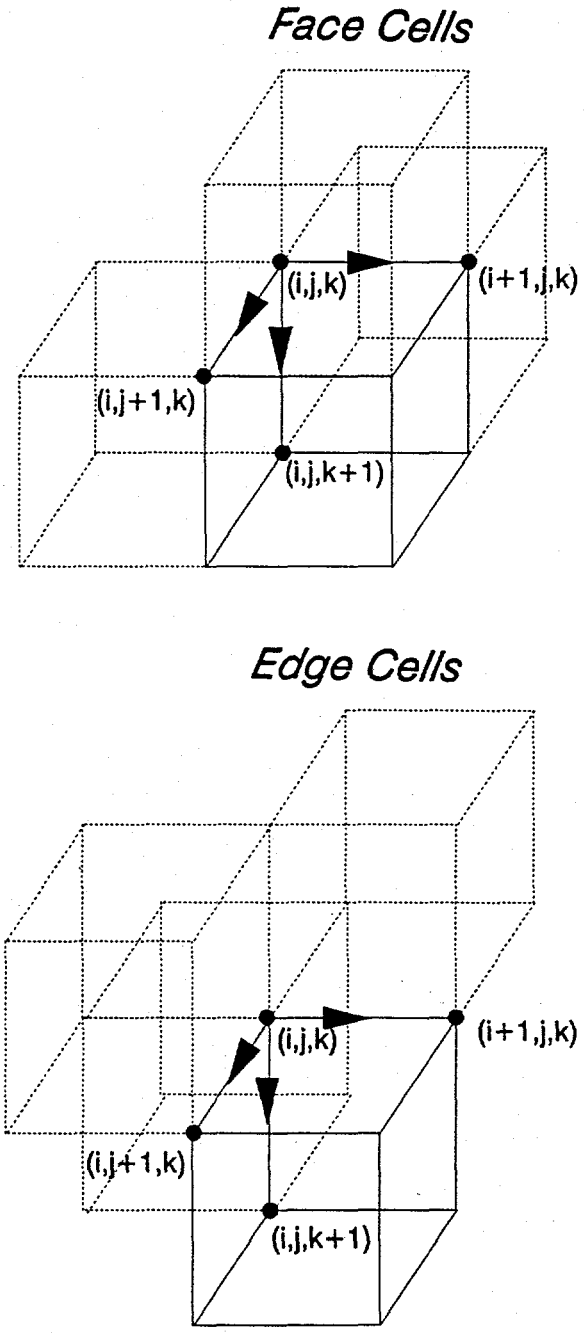


Figure 22. The different cells needed to compute average electrical properties at edges (i+½,j,k), (i,j+½,k) and (i,j,k+½). These edges, as well as the solid cell are assigned to node (i,j,k). The additional face and edge cells needed to compute average electrical properties are indicated by the dashed outlines. Using results for the single processor and cell, a processor map can be developed to carry out the required local communication amongst processors, necessary for subsequent forward model calculations.

*Face Communication*

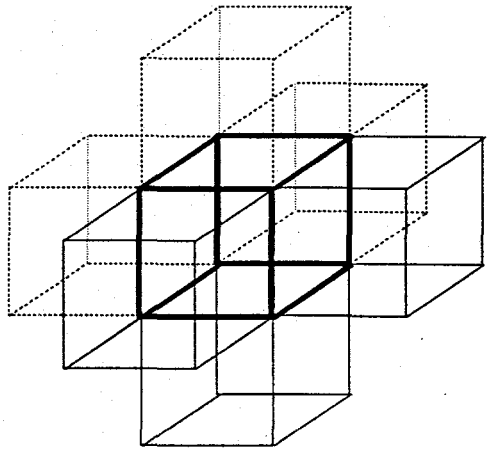

*Edge Communication*

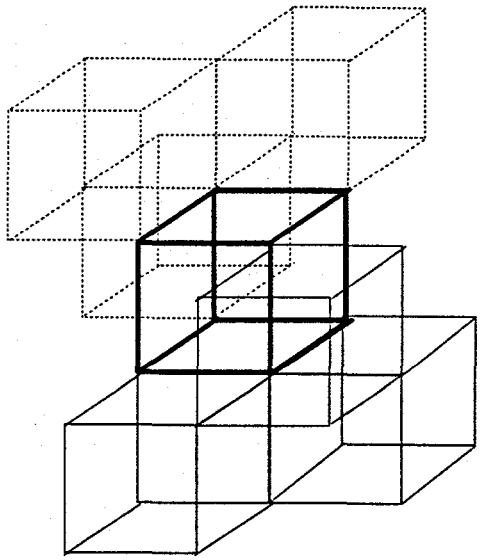

Figure 23. Local processor communication scheme used in the 3-D MP inverse. The solid cube depicts the central processor that is sending and receiving from its neighbors. Both face and edge communication patterns are indicated.

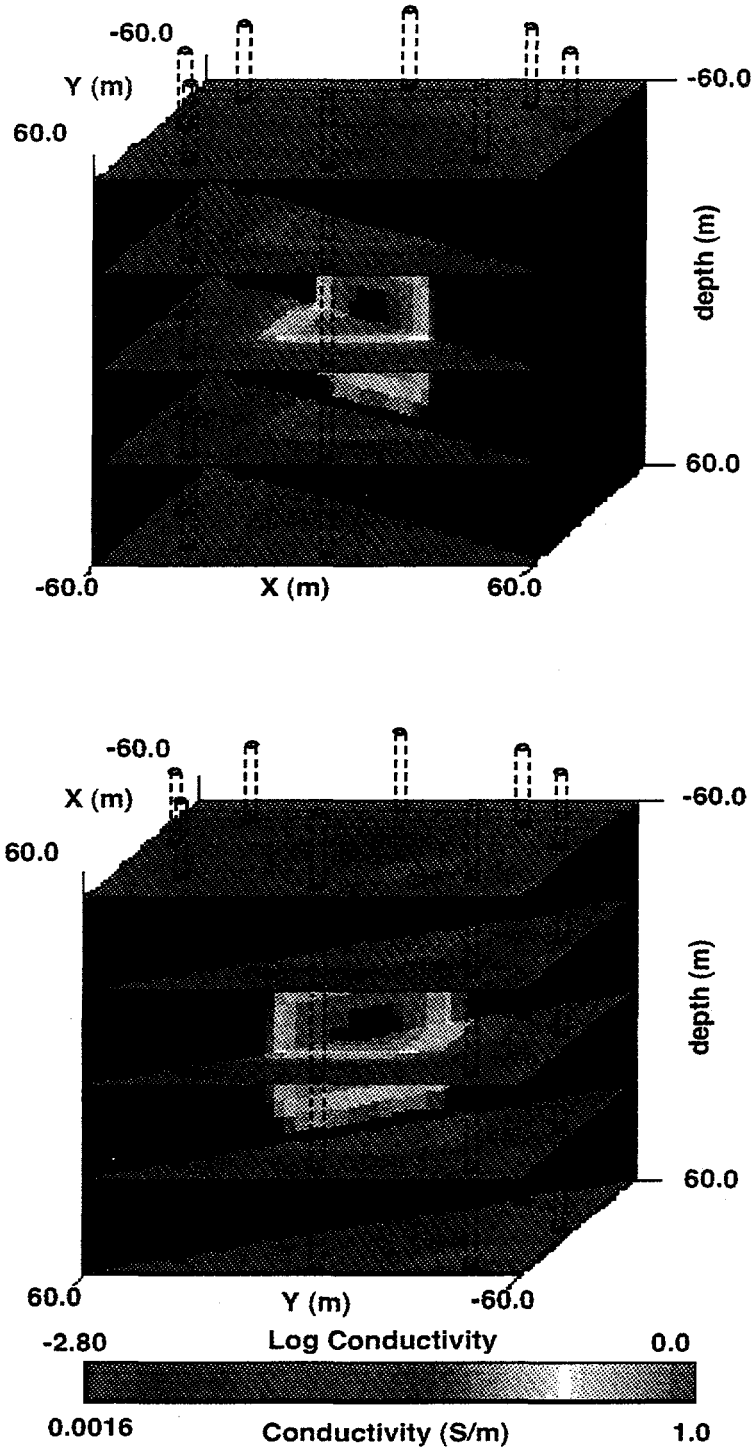


Figure 26. Reconstructed conductivity for the synthetic example illustrated in Figure 25. The wellbores used in the simulation are also indicated.

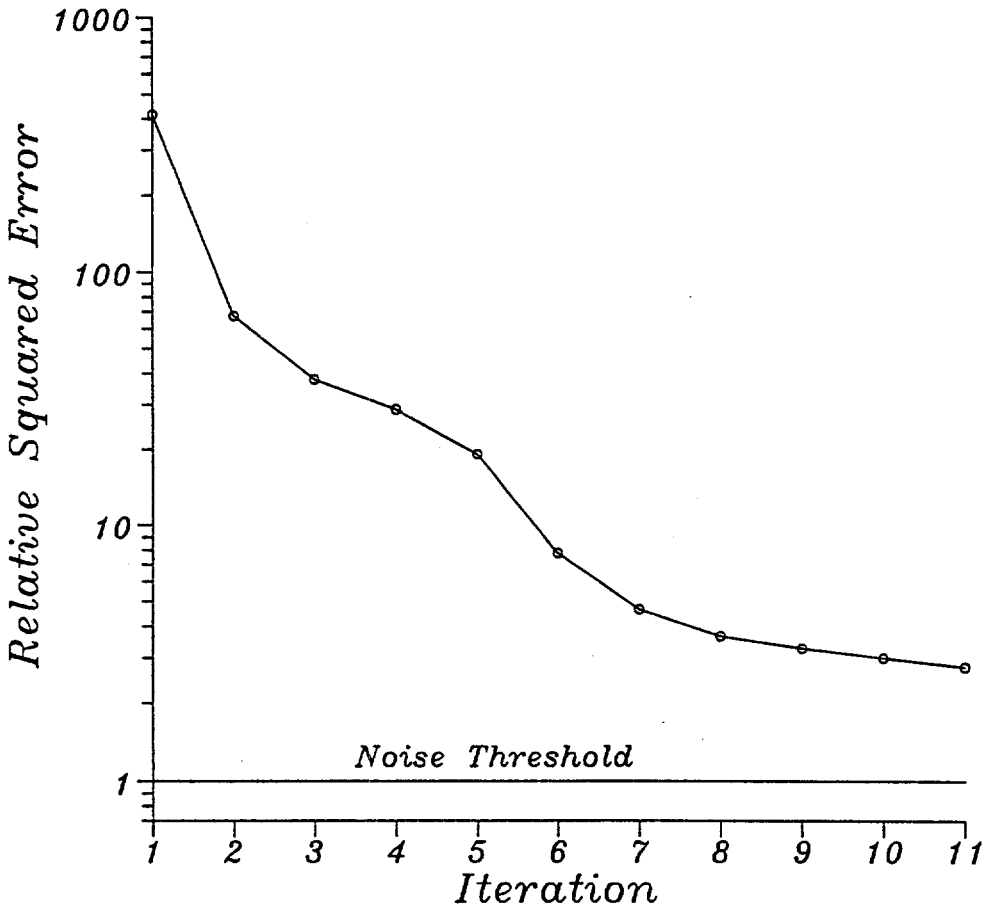


Figure 27. Sum of squared error plotted against iteration number for the 0.2 S/m test body shown in Figure 25. The squared error has been normalized by the variance of the noise.

# CHAPTER IV

## ANALYSIS OF A 3-D CROSS WELL EM EXPERIMENT

Although synthetic examples such as the one presented in the last chapter illustrate the theoretical accuracy and limitations of a geophysical inversion algorithm, the real test of a scheme's usefulness, versatility and robustness comes when data collected at a field site are inverted to produce an image of the subsurface. In general the characteristics of the noise are much different than the Gaussian noise assumed in synthetic tests and the data tend to be more sparsely sampled due to survey time constraints than one would like. In addition with certain types of surveys, such as a crosswell EM survey, the unknown accuracy of the source and receiver locations may provide additional sources of error.

To illustrate the benefits provided by the full 3-D inversion code, as well as how these problems affect the images, we have inverted a crosswell data set that was collected to monitor the injection of a volume of salt water at depth. The versatility of the scheme is demonstrated by not only producing 3-D images of the subsurface, but by also employing it for pre-imaging experimental design and resolution analysis, as well as post-imaging error analysis. In addition, the benefits of the massively parallel computer platform is demonstrated by the quick turn around time for the images as well as the number of imaging experiments that can be accomplished within a given time period.

## THE RICHMOND FIELD STATION EXPERIMENT

The University of California's Richmond Field Station has been the location of a series of salt water injection monitoring experiments since 1988, the purpose of which have been to simulate both an enhanced oil recovery water flood as well as the injection of a contaminants and/or tracers into an aquifer. The site contains several monitoring wells (Figure 28) as deep as 80 m which show the geology to consist of unconsolidated alluvium to depths of 30 to 35 m overlying a basement of sandstone and shale. The alluvium consists of muds and silts interbedded with layers of sand and gravel and well logs show this upper section to have conductivities ranging from 0.2 to 0.02 S/m. The basement tends to be more resistive with conductivities as low as 0.001 S/m. In addition the logs indicate that an unconformity of some type exists in the basement between the Inj and NW wells. This unconformity is likely due to either steeply tilting stratigraphy or a fault.

Although more thorough descriptions of the experiment can be found in Alumbaugh and Morrison (1995) and Wilt et al. (1995a), for completeness a brief description is given here. In May of 1992, crosswell electromagnetic measurements were made by placing a vertical magnetic dipole (VMD) source operating at 18.5 kHz in the central well, and making vertical magnetic field measurements in the four surrounding wells (Figure 28) using the system described by Wilt et al.

(1995a). The measurements were made at 5m receiver intervals from 5m to 60m depth which yields 11 receiver positions per well. A similar range of source depths was employed using a sampling interval of 0.5m.

After this baseline set of measurements had been completed, 50 000 gallons of 1 S/m salt water was injected into a gravel aquifer at 30 m depth through the center well in Figure 28. A second set of measurements were then completed using the same parameters as in the baseline survey. In addition, post-injection repeat data sets were collected between the injector and the NW well, and the injector and the SW well at a time interval from the original surveys of one week and two weeks, respectively. The purpose of these repeat measurements was to better quantify the noise characteristics of the data. The experiment ended in June of 1992 prior to pumping out the salt water.

The purpose of this particular experiment was to analyze how well the plume location could be determined through crosswell EM tomography. Alumbaugh and Morrison (1995a), Liu et al. (1995) and Wilt et al. (1995a) all employ EM inversion schemes that assume a 2-D cylindrical geometry in which the geology is symmetric about the borehole containing the source. In all three cases the plume was clearly shown to be migrating in a northerly direction. In addition, Newman (1995) employs a 2.5D geometry in his inversion scheme which yields similar conclusions for the data collected between the injector and the NW well. These conclusions all agree with surface-to-borehole dc resistivity measurements made by Bevc and Morrison (1992).

Although these images were very successful in mapping the general migration route of the plume, questions still remain about the 3-D shape of the plume. In addition, as demonstrated by Alumbaugh and Morrison (1995a), assuming a 2-D geometry can impose artifacts in the images if the geology does not fit the 2-D assumption. Thus to better describe the shape of the plume as well as more accurately resolve the geology, a 3-D inversion scheme is needed.

## EXPERIMENT DESIGN AND RESOLUTION ANALYSIS

One of the critical questions when trying to image geologic structure is what acquisition parameters are needed to adequately resolve structures in the subsurface? If the data have already been collected then the question becomes given the survey acquisition parameters, what resolution can we expect to achieve from the data? Thus before inverting the Richmond Field Station data we shall employ the 3D inverse to try and answer these questions. However, because the experiment actually took place before these simulations could be conducted, the focus here will be to predict how well the plume and assumed electrical structure of the site can be recovered, and what improvements could be made to the survey configuration to improve the resolution.

Figure 29 shows the synthetic model employed in this simulation. Horizontal slices of the electrical conductivity from the zero to 60 m depth illustrate conductive sediments overlying

resistive basement. The finer structural features that we are trying to resolve include the conductive salt water plume at 30m depth within a thin (4m thick) aquifer, a vertical contact between resistive units within the basement, and a thin (4m thick) conductive channel at 22m depth within the overburden at the location of the SE well. The basement contact and the channel have been included in the model using information from the northeast and southeast well logs. A source sampling interval of 2.5 m was employed from 5m to 60m depth as will be employed when imaging the data, and a receiver sampling of 5m was used as in the experiment. This yields a total of 924 data points. The synthetic results were calculated using the finite difference code described in Chapter II. (Note: we have not included the air-earth interface in this example. The exclusion of this boundary is discussed in more detail in the next section.)

Because all data contain some type of error, a necessity for producing accurate images through data inversion is to estimate the quality of the noise. To do this we have analyzed the two repeated sets of data taken after the injection. Wilt et al. (1995a) present the average errors for these repeat data to be 2.2% in amplitude and 0.8 degrees in phase, and 3.3% in amplitude and 1.1 degrees in phase for the INJ-NW and INJ-SW repeats, respectively. A more rigorous way to analyze the noise is to look at the mean and standard deviation of the errors as a function of common source-receiver offset. As shown in Figure 30, this type of analysis shows the repeatability noise to decrease at the same rate as the signal amplitude for shorter offsets, and then become approximately constant for longer offsets. This implies that at these larger offsets the noise as a percentage of the data is going to be much larger than at the shorter offsets. The noise model that we have employed here is based on this analysis and assumes random Gaussian noise with a standard deviation equal to 2% of the magnetic field for amplitudes greater than $1x10^{-6}$ A/m, and a standard deviation equal to $2x10^{-8}$A/m when the field drops below this value. The data were then weighted within the inversion scheme with this noise distribution, which effectively downweights the longer offset data.

The image resulting from the simulation is given in Figure 31, and in Figure 32 we have plotted the average residual error as a function of the iteration number. Notice that the residual decreases smoothly and flattens out as it approaches the estimated noise level. The forward and inversion domains consist of 46x46x54 and 42x42x50 cells, respectively, and thus a total of 88 200 cells were used to estimate the electrical conductivity. However for compactness only 34 000 cells within the region of interest are shown in Figure 31. To run this using 512 processors of the Intel Paragon took approximately 6 hours, or 1/2 hour per iteration where the inversion was launched assuming a whole space of 0.033S/m.

Figure 31 shows that we have recovered the general geology of conductive sediments overlying resistive basement as well as the location of the plume remarkably well. However, notice that the sharp edges of the plume have not been recovered; this is to be expected from a scheme that imposes smoothness constraints on the solution. In addition notice that neither the

channel structure, the aquifer nor the contact within the basement are imaged very well. We feel that the former is caused by too large of a receiver sampling interval in the vertical direction. We have deduced this because the plume and the channel are both 4m thick. However the source sampling interval within the plume is 2.5m, while the receiver sampling interval within the channel is 5m. The plume is recovered by the finer sampling interval while the channel is not. Thus the receiver sampling interval needs to be decreased in order to recover finer structures.

The inability to resolve the aquifer may also be attributed to insufficient receiver sampling. However the aquifer is a resistive target of fairly low contrast with respect to the background when compared to the conductive targets. Thus because cross well EM is an inductive method, the aquifer may not be generating enough of a scattered response to be resolved.

With regards to the basement contact, we believe that the resolution can be improved if a higher frequency is employed. This is based on the fact that the basement structure is fairly resistive such that there is only 1/2 skin depth of attenuation between the wells compared to 1.5 to 2 skin depths attenuation in the conductive sediments. As demonstrated by Alumbaugh and Morrison (1995b), greater attenuation implies greater resolution. Because an increase in frequency implies an increase in attenuation, a higher frequency should provide better resolution.

However, part of the problem in accurately recovering the basement structure, especially the formation of the relatively conductive artifact near the source well in Figure 31, can be rectified by employing more complete data coverage around the imaging region. This is illustrated in Figure 33 where we have simulated and imaged a data set that includes four additional receiver wells between the four original wells. This example took 7 hours to run using the same number of processors as above. Notice that the artifact near the central well has disappeared, and that the contact though distorted is better defined. In addition there is a minor improvement in locating the position of the channel as well as the conductivity distribution within the plume. However notice that the general shape of the plume has not been altered. Thus, although we may have problems with the Richmond data in imaging structures finer than the source and receiver sampling intervals and fully recovering the basement structure, we should be able to accurately locate the position of the plume which was the primary objective of this experiment.

## ELECTRICAL RECONSTRUCTIONS OF THE FIELD DATA

Initially the data were weighted using the same noise estimates as used for the synthetic examples in the previous section. Unfortunately, the normalized residual error refused to converge when this noise model was employed, which indicates that we were giving to much weight to poor quality data. Thus we chose to weight the data by two percent of the maximum amplitude for each source relative to all the receivers in a given observation well. This type of weighting puts more emphasis on short offset positions compared to the long ones; because the data quality tends to be

better when the source and receiver are close together, this gives greater weighting to good data. This weighting scheme was found to allow the inversion to converge.

A second major difference between the Richmond data and the simulations above is that the measurements at Richmond were made in the presence of the air-earth interface. Because the inclusion of a half space interface is computationally more demanding, employing this as a background model could cause the inversion scheme to run much slower. To determine if we needed to employ a half-space rather than whole-space within the inversion, a synthetic data set was calculated for the model in Figure 29 which contained this boundary, and then this data inverted assuming a whole space. It was demonstrated that the half-space effects rapidly decreased with increasing depth and thus it was determined that we could launch the inversion assuming a 0.033S/m conductive whole-space.

The image resulting from the pre-injection data is given in Figure 34, the post-injection data in Figure 35, and the average residuals for the inversions in Figure 36. These each took approximately 4 hours to run using 512 processors of the Paragon. Both images clearly show the conductive overburden as well as the resistive basement. In addition, the plume is evident in the post injection image (Figure 35) at 30 m depth to the north of the injector well. To emphasize the plume we can subtract the pre-injection image from the post-injection as illustrated in Figure 37. Although the plume is evident from 26 to 32 m depth which corresponds to the injection interval, the thickness is not evident here because we have only included selected depth slices.

Conductive zones also appear within the overburden in Figures 34 and 35 between the receiver wells where there is no data coverage. Because these did not appear in the synthetic example (Figure 31) one would tend to imply that these zones represent structure. One alternate suggestion is that the different weighting scheme used to invert the data has somehow caused less sensitivity to these regions resulting in artifacts. To rule this out we inverted the synthetic data employing the same data weighting scheme as employed in this section and found no generation of these phenomena. A second more plausible explaination is that these are artifacts caused by inaccurate knowledge of the source and receiver locations. To demonstrate how this idea was developed, we next examine the residual errors between the measured and predicted data for each individual source-receiver combination.

## ERROR ANALYSIS

Alumbaugh and Morrison (1995b) show that by plotting the residual error as a function of source and receiver position, one can determine if there exists a non-random bias either in the data or in assumptions made within the imaging scheme. In that particular example they show how large biases in the residuals and artifacts in the images can result if a 2-D model geometry is employed within the inversion for imaging data generated in a 3-D media. Here we can be fairly

confident that because we are using a full 3-D model geometry this type of bias will not exist. Thus any non-random component of the residual that does appear is more likely to be due to errors in the data collection process.

Before presenting the residual errors between the Richmond field data and the predicted data of the final images, it is instructive to investigate the residuals from the resolution analysis section. Here the plotted values are simply the difference between the measured and predicted data normalized by the weighting. Figure 38 shows the residuals for the image in Figure 31 when the receiver is in the NW well. Notice the random pattern which indicates there is no bias in the data. This is to be expected because the noise that was added is random in nature. However, as illustrated in Figure 39 this is not the case for the post-injection data collected in the Richmond experiment. (The pre-injection data residuals demonstrate almost and identical response and are not shown here.) The residual gradually increases with increasing source and receiver depth such that the largest errors are observed when both sensors are located in the basement. Further, the southeast well has the largest residuals, which can be as large as 10. Because the data weighting was 2% of the maximum amplitude, this normalized value is equivalent to 20% amplitude error. Note that the residuals in the imaginary component of the data are always less than corresponding real component. This is expected because 1) the high resistivity of the basement coupled with the fairly low frequency ensures that the measurements were made in the quasi-static field so that the real part of the field is much larger than the imaginary and 2) the weighting was based on data amplitude rather than the real and imaginary components separately.

The clustering of large residual values in the basement indicates that the data are some how biased as the source and receiver get deeper into the earth. One possible source of this error could be a deviation in the wells from the assumed vertical orientation. Numerical experiments with a two layered-earth model (conductive overburden and resistive basement) showed that a similar bias can be produced if the predicted data are calculated assuming the wells are straight but the measurements are made in boreholes that are deviated. A deviation as little as 1/2 to 2 m at the bottom of the wells was found to produce errors on the same order of magnitude as those observed.

To further test this idea, the data employed in the resolution analysis portion of this chapter were again run through the inversion scheme assuming two different scenarios: (1) the bottom of the observation wells were assumed to be deviated in towards the injector well and (2) the bottom of the wells were assumed to be deviated outward away from the injector. This was accomplished by taking the synthetic data that were calculated assuming vertical wells and altering the horizontal locations of the receivers with depth in the inversion. Specifically the inward or outward receiver deviations at each depth were calculated by assuming zero horizontal offset at the surface and linearly varying it downward such that at 60m depth the horizontal offset was 2 m for the southeast

well, 0.2 m for the southwest well and 1 m for the northeast and northwest wells. These values were selected based on the size of the data residuals observed in the field experiment. Here the data weighting scheme employed was identical to that used in the inversion of the field data.

The data residuals for the two scenarios are illustrated in Figures 40 and 41, while the resulting images are given in Figures 42 and 43. The residual plots show a bias along the diagonal near the bottom of the wells which in general is very similar to those of the data. In addition notice that if the receivers are assumed to be closer to the source than is actually occurring, the residuals are positive along the diagonal. If the reverse is true the residuals are negative. Thus we can crudely determine the errors in positioning of the receivers with respect to the transmitter. However, because the injector well could also be deviated we can not determine the exact location of the sensors with this analysis. Finally, the electrical reconstructions for the two scenarios in Figures 42 and 43 clearly show the presence of artifacts resulting from the sensor location errors that are similar to those observed in Figures 34 and 35. However, notice that the plume is still fairly accurately located.

## CONCLUSIONS

The 3-D inversion scheme has been successfully employed to image data collected in a crosswell EM experiment. The scheme has not only provided images of the site, and especially of the injected salt water plume, but also has been demonstrated to be of great use in defining the resolution of the experiment as well as what type of errors are present in the data. From this analysis we have determined that 1) the plume is fairly well resolved with this configuration and 2) the wells at the Richmond Field station are most likely not vertical, but rather are deviated with increasing depth. In addition the speed and versatility of the massively parallel computer platform has been demonstrated; jobs that only take 3 to 4 hours on the Intel Paragon could take as long as a week on a high end workstation.

In the near future we will be analyzing other data sets that employ different source and receiver configurations. Although we are currently limited by the number of sources and receivers that can be employed, we are currently looking at methods to remedy this situation as outlined in chapter III. Finally, we would like to suggest that any geophysical imaging experiment that includes measurements within boreholes should have the wells accurately surveyed in to determine if any deviations exist. As illustrated here, this can have a large impact on the accuracy of the resulting images.

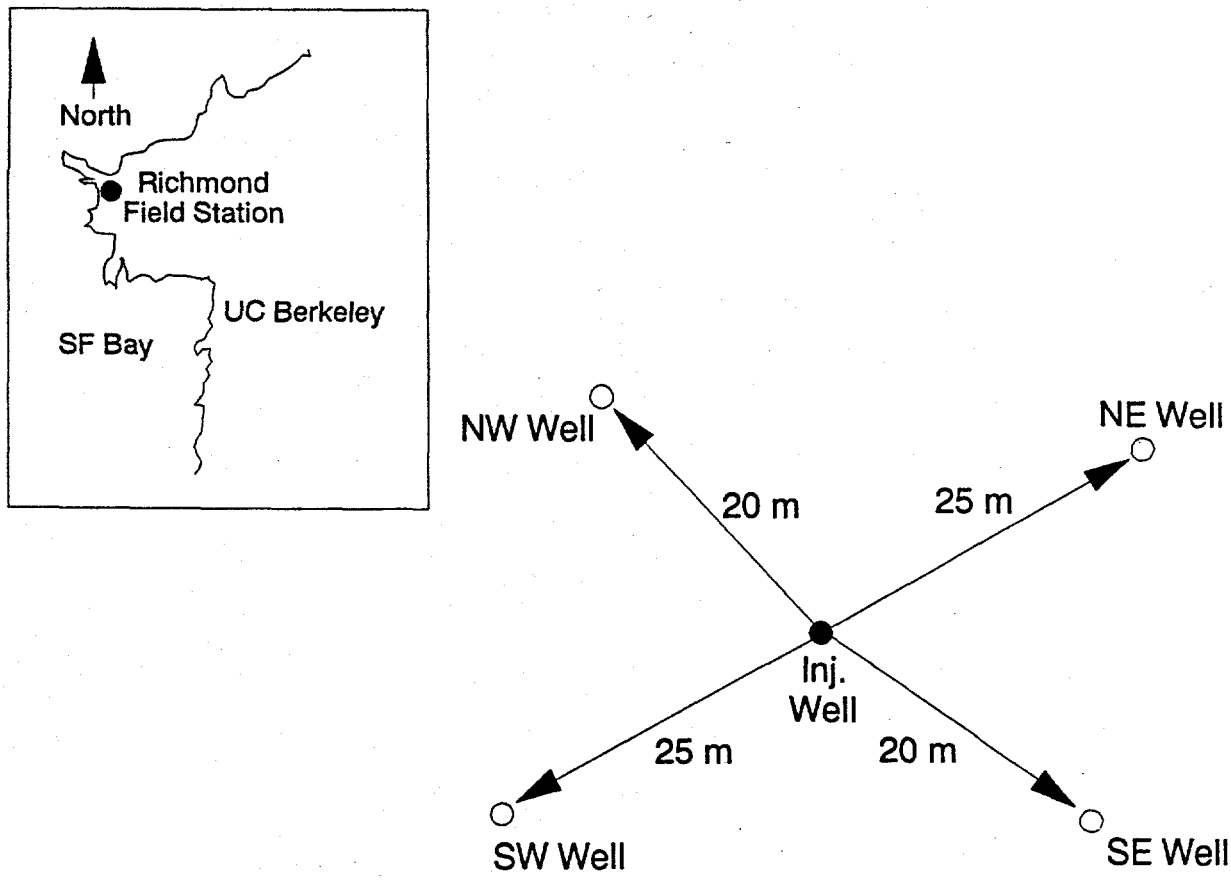


Figure 28. Layout of the Richmond-field site experiment.

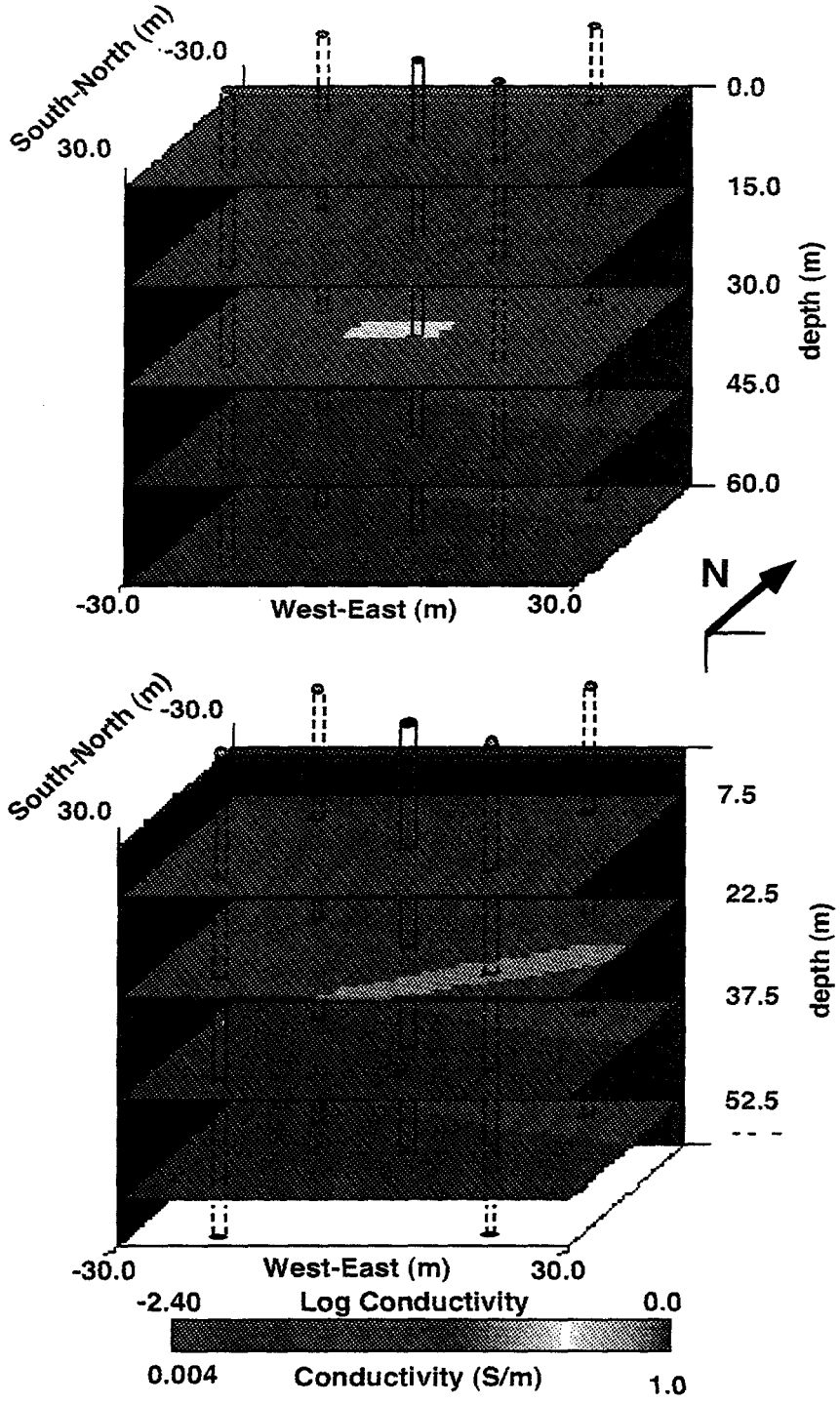


Figure 29. The five well Richmond test model used in the design experiment. Four observation wells and the injector well are indicated along with depth slices of the conductivity.

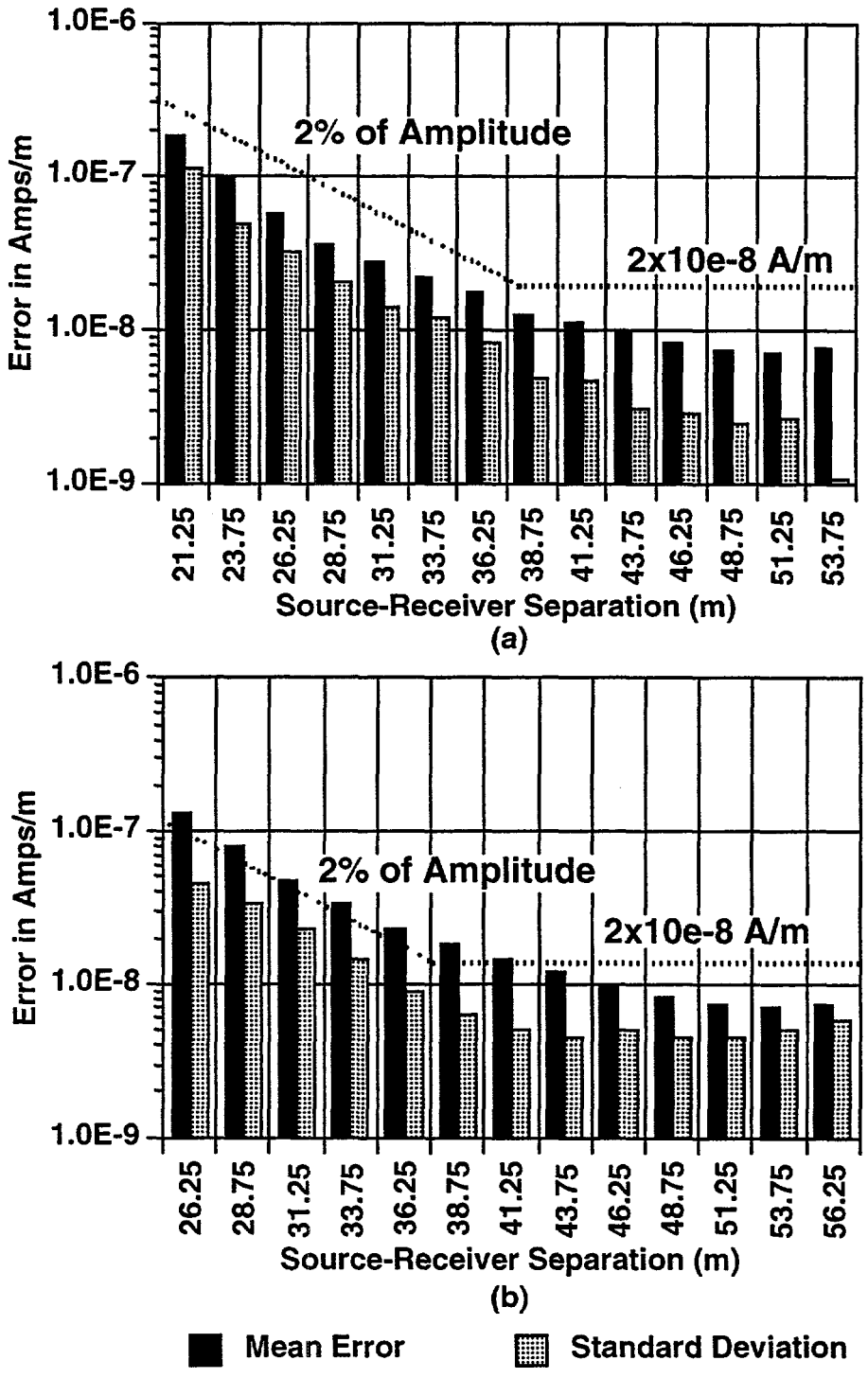


Figure 30. Mean error and standard deviations as a function of source-receiver separation for two data sets collected between a) the central and NW wells at an interval of one week, and b) the central and SW wells at a two week interval.

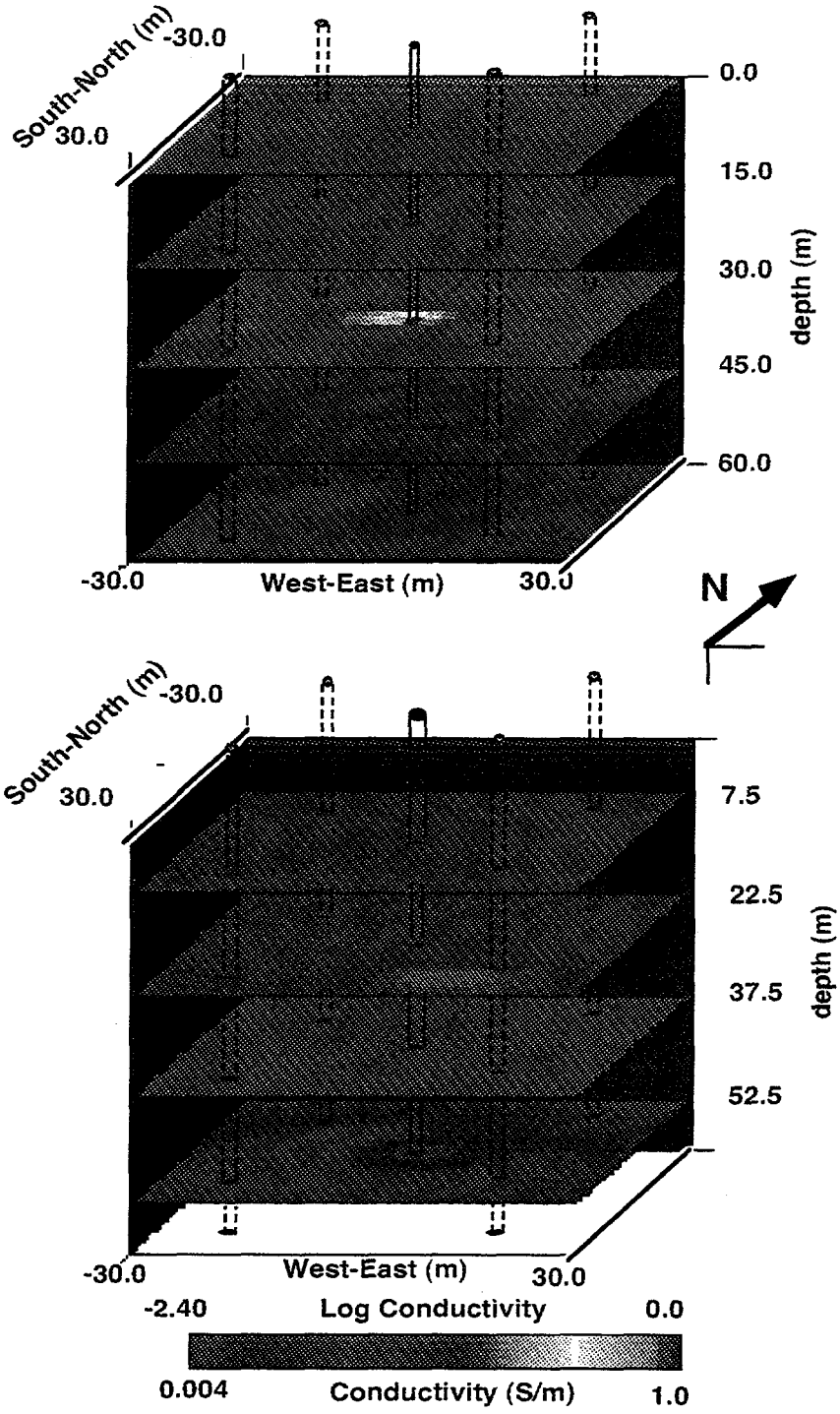


Figure 31. Conductivity reconstruction of the synthetic data generated from the model shown in Figure 29.

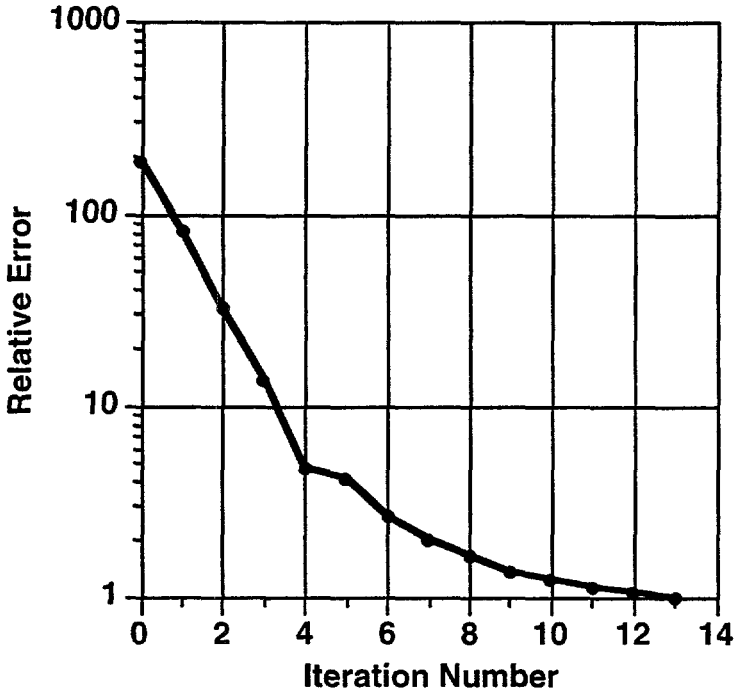


Figure 32. Normalized squared error plotted against iteration number for five well test model. Thirteen iterations were needed to obtain convergence.

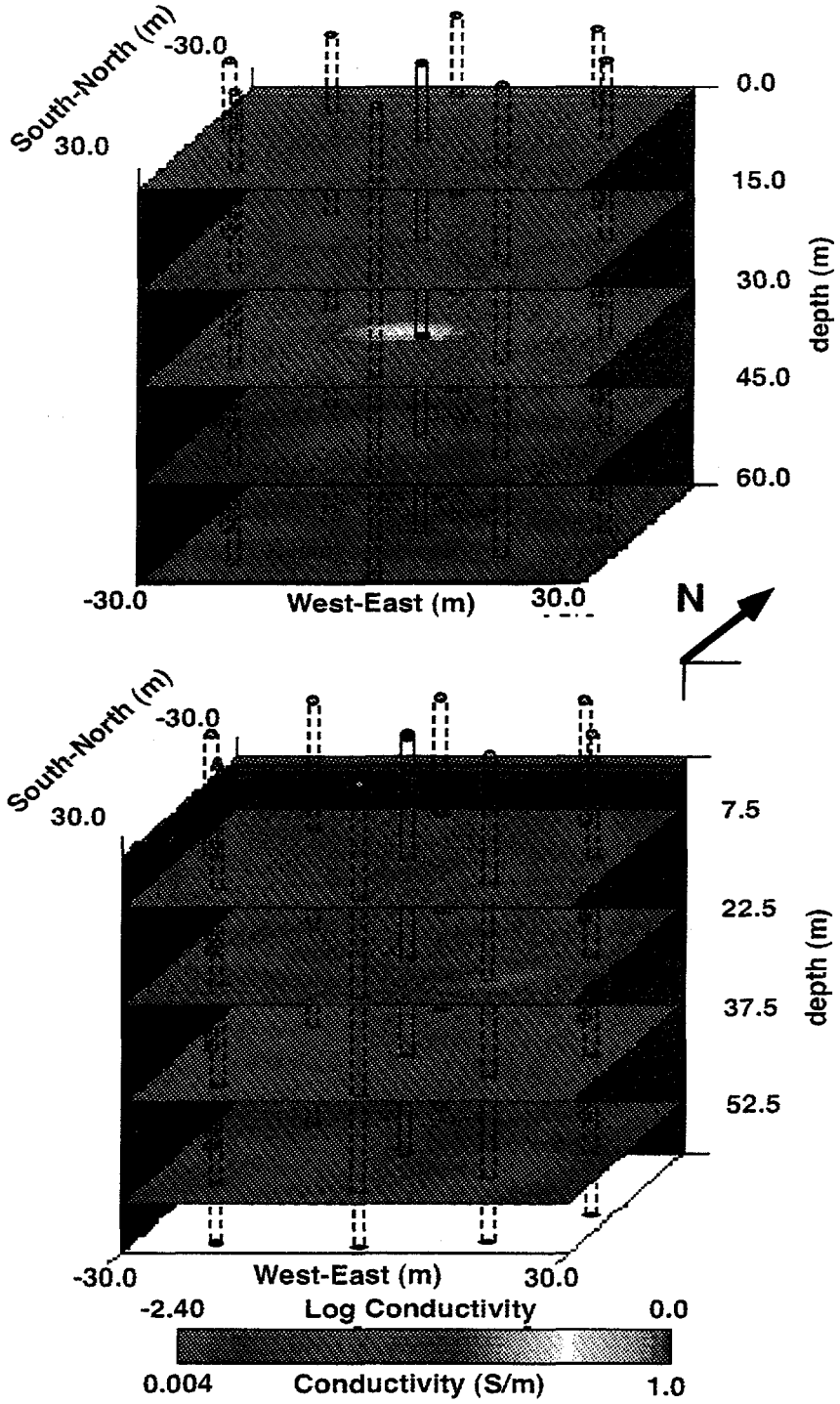


Figure 33. Conductivity reconstruction of the synthetic data generated from the model shown in Figure 29 employing eight wells.

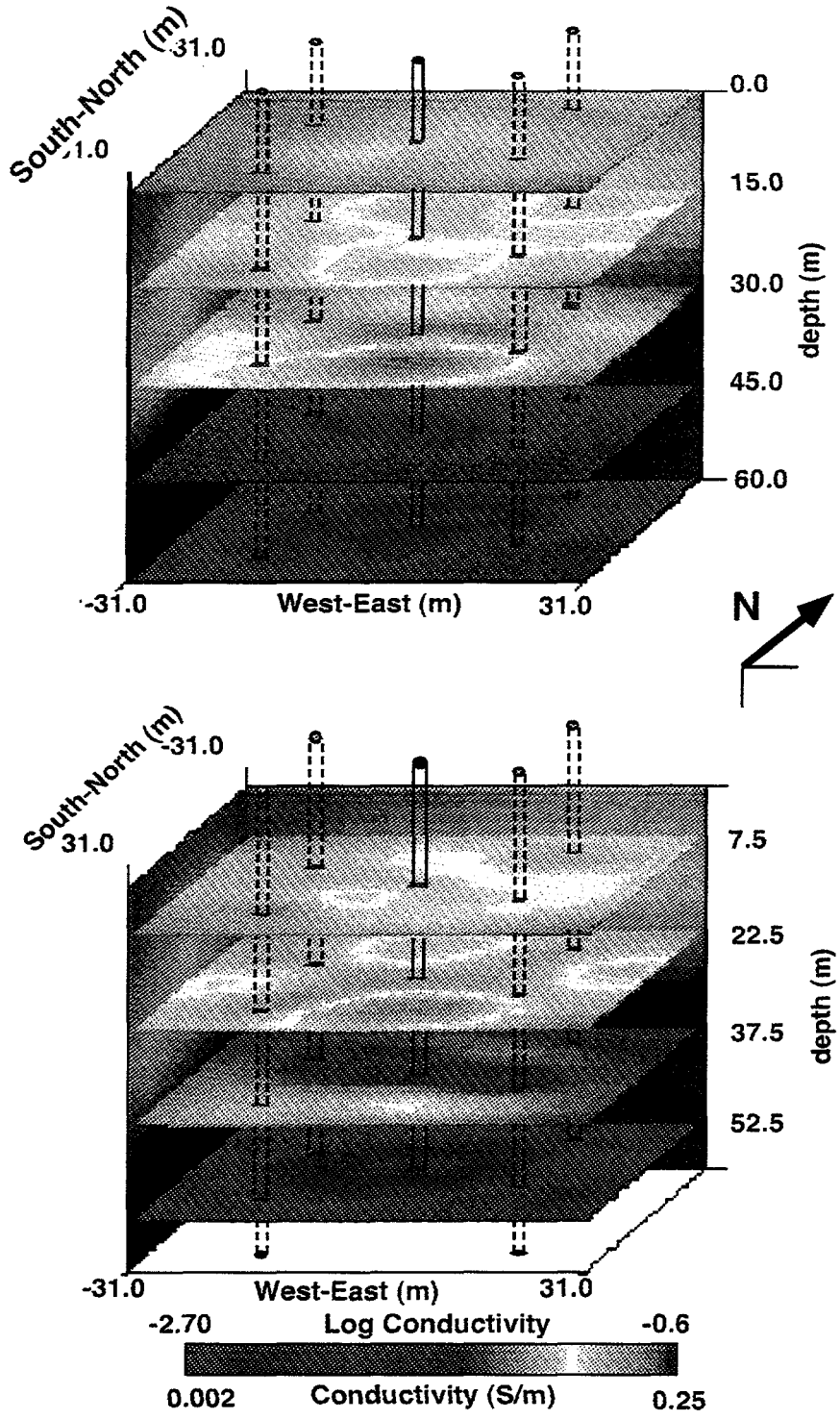


Figure 34. Conductivity reconstruction of the pre-injection data set for different depth slices.

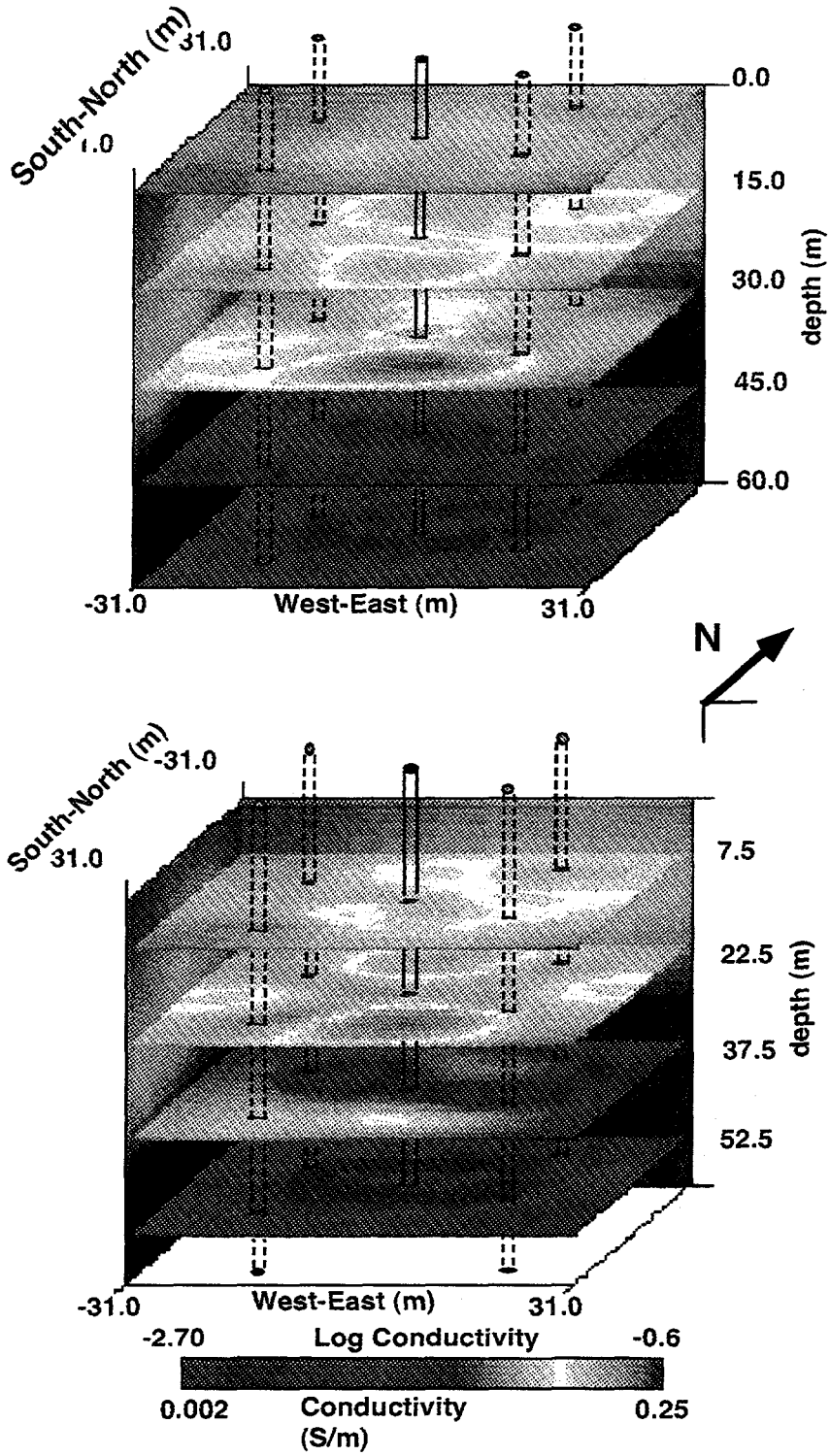


Figure 35. Conductivity reconstruction of the post-injection data set for different depth slices. The plume is indicated in the 30 m depth slice near the injector well.

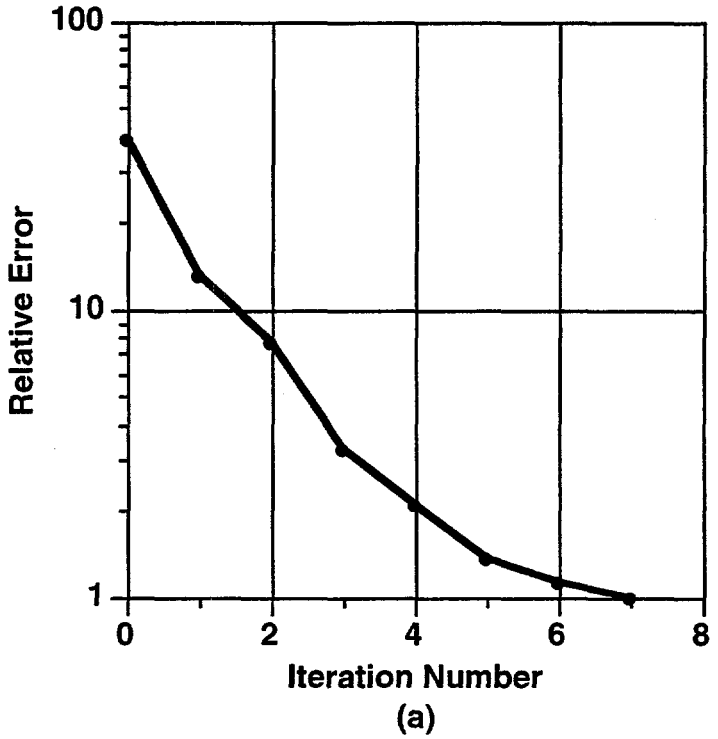


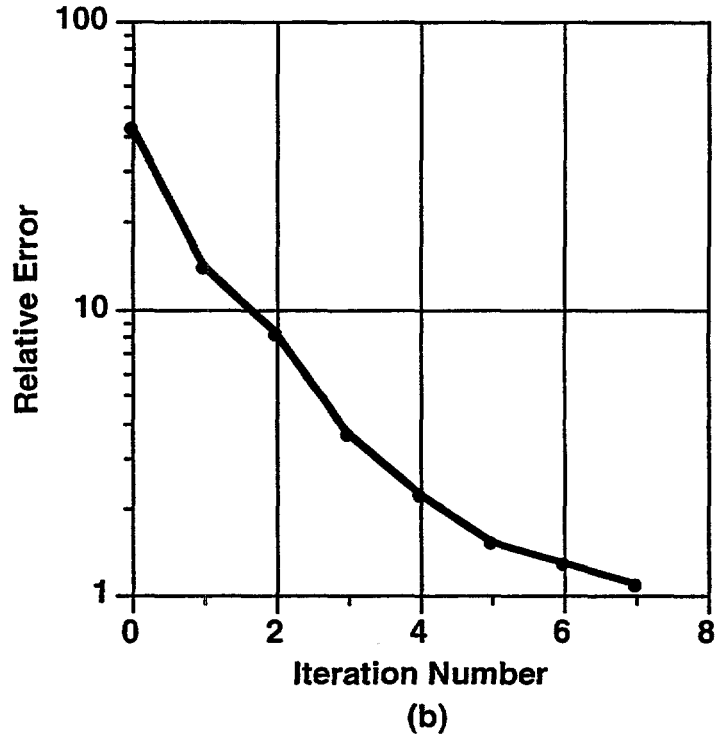


Figure 36. Normalized squared error plotted against iteration number for the (a) pre and (b) post injection data sets acquired at Richmond. The data were weighted by 2% of the maximum amplitude for each source relative to all receivers in a given observation well.

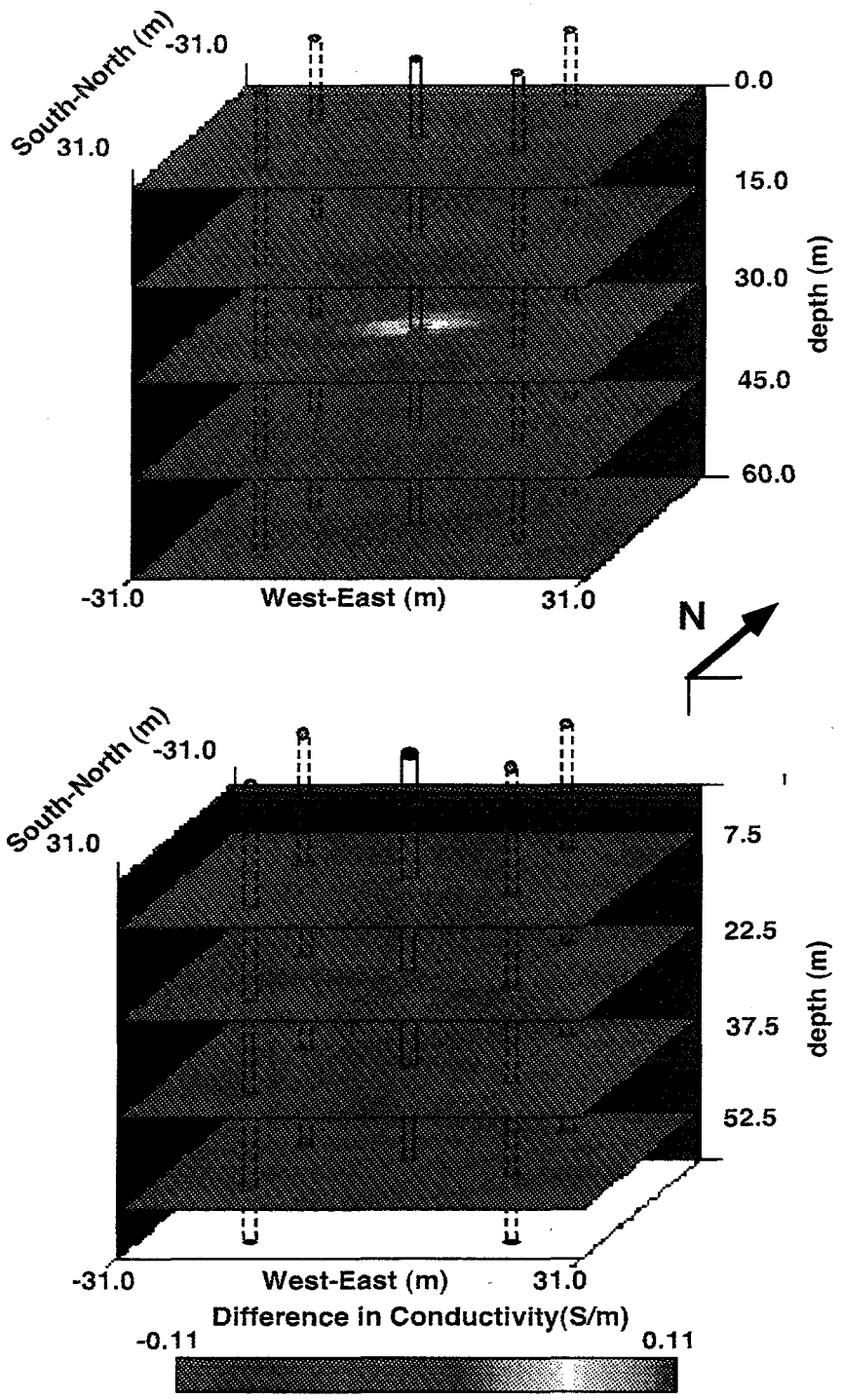


Figure 37. Difference image between the (a) pre and (b) post-injection reconstructions of the field data.

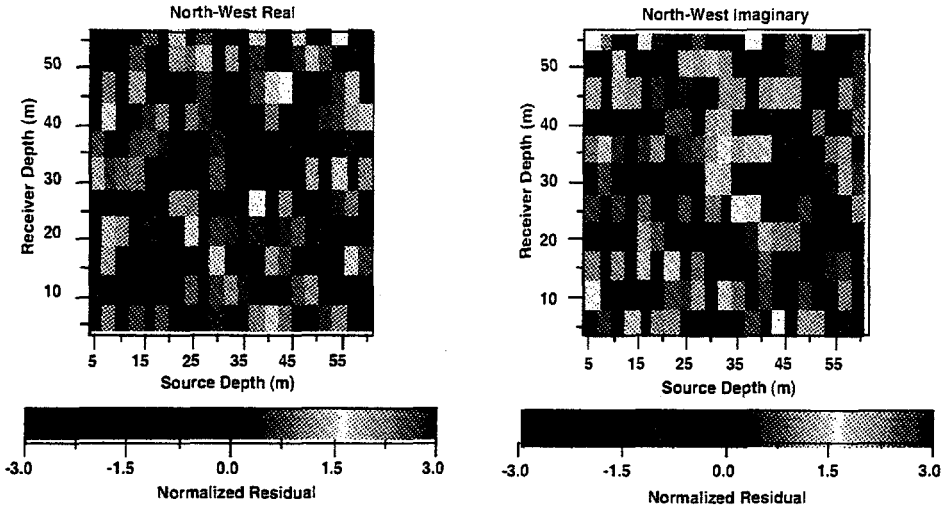


Figure 38. Residuals errors of synthetic data calculated for the image in Figure 31. Real and imaginary residuals are shown only for the northwest well.

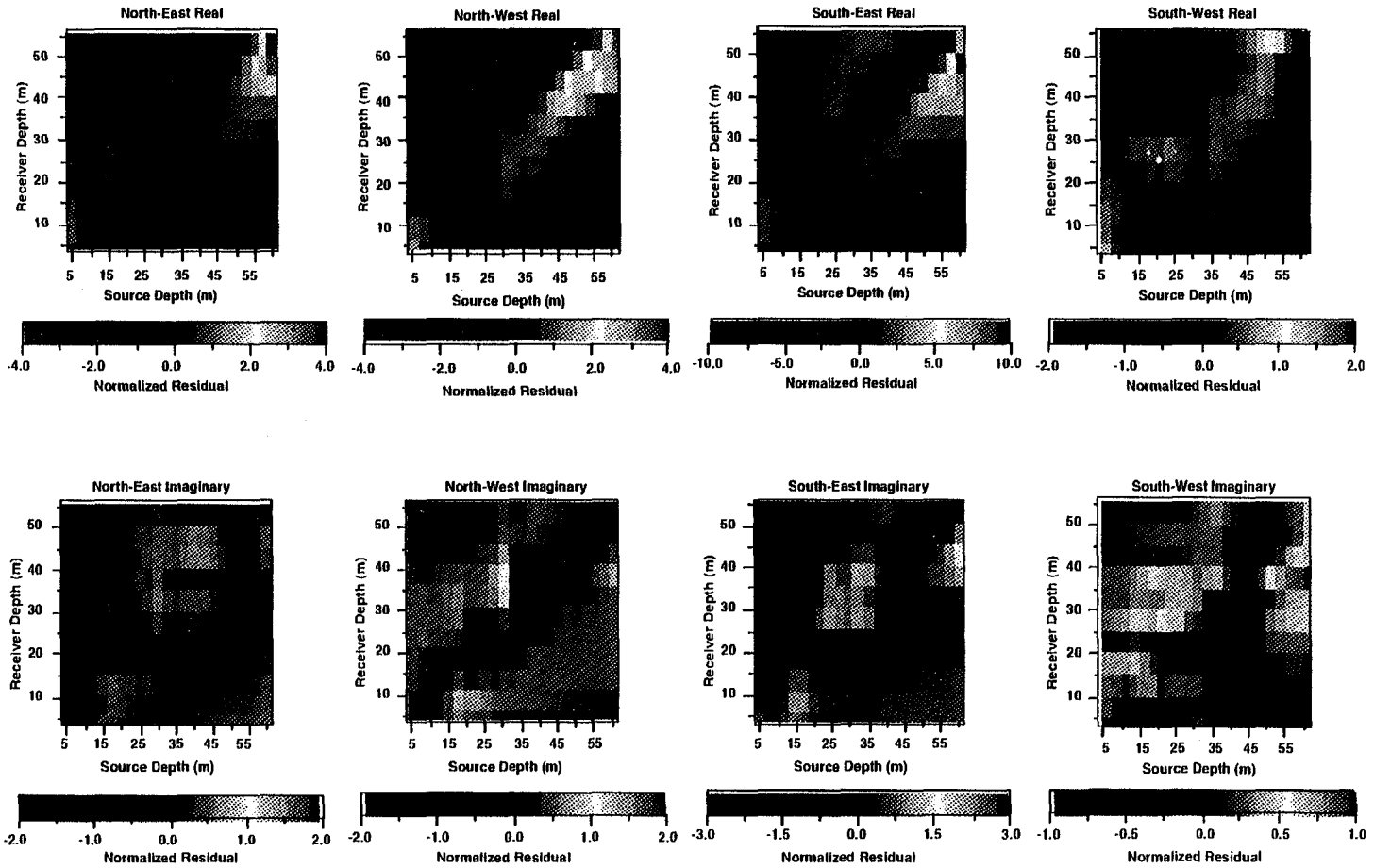


Figure 39. Residual errors for the post injection data. Results are shown for all four observation wells.

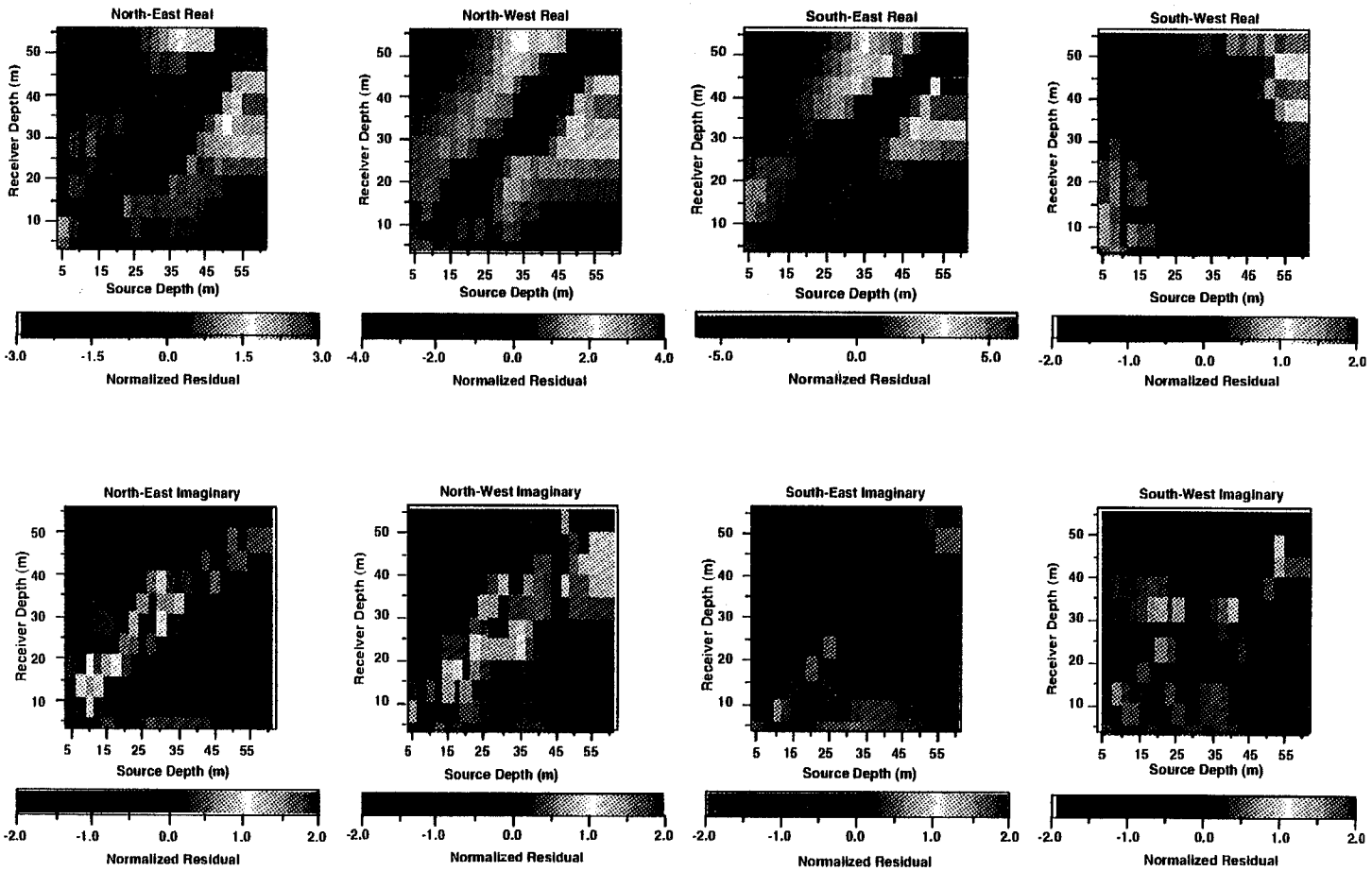


Figure 40. Residuals for a four well design experiment, where the observation wells are assumed to be deviated towards the injector.

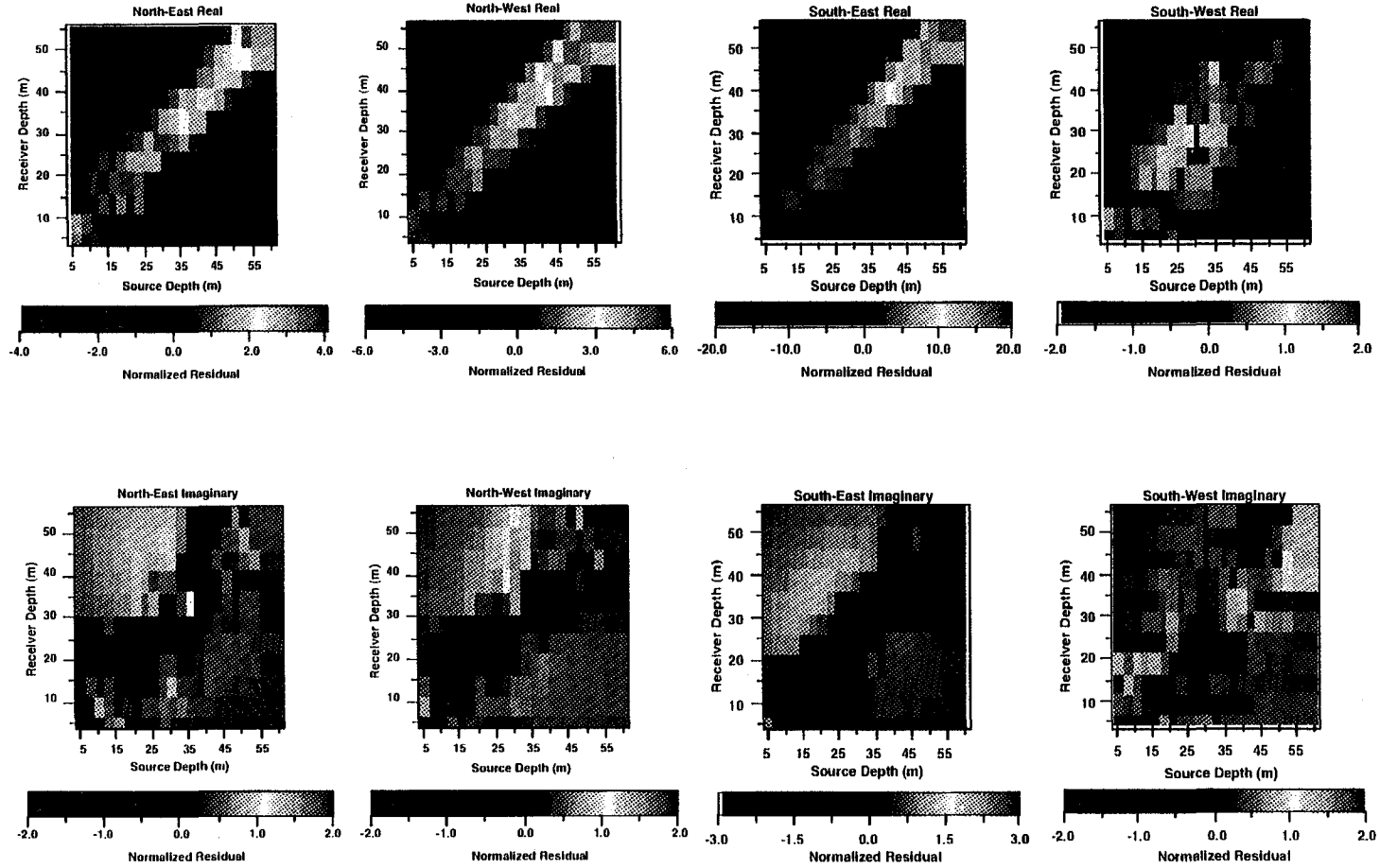


Figure 41. Residuals for a four well design experiment, where the observation wells are assumed to be deviated away from the injector.

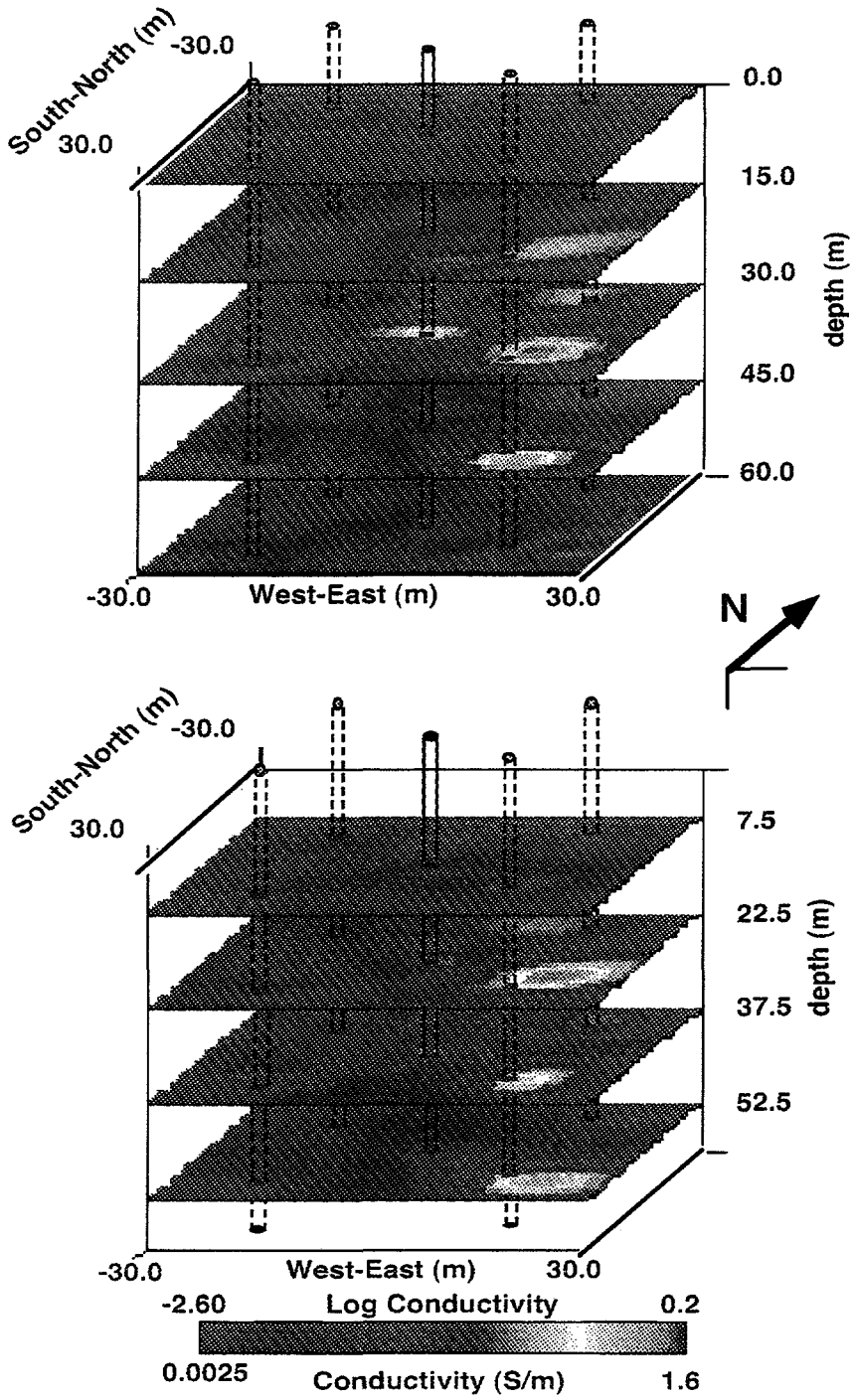


Figure 42. Conductivity reconstruction for the four well test model assuming the wells are deviated toward the injector.

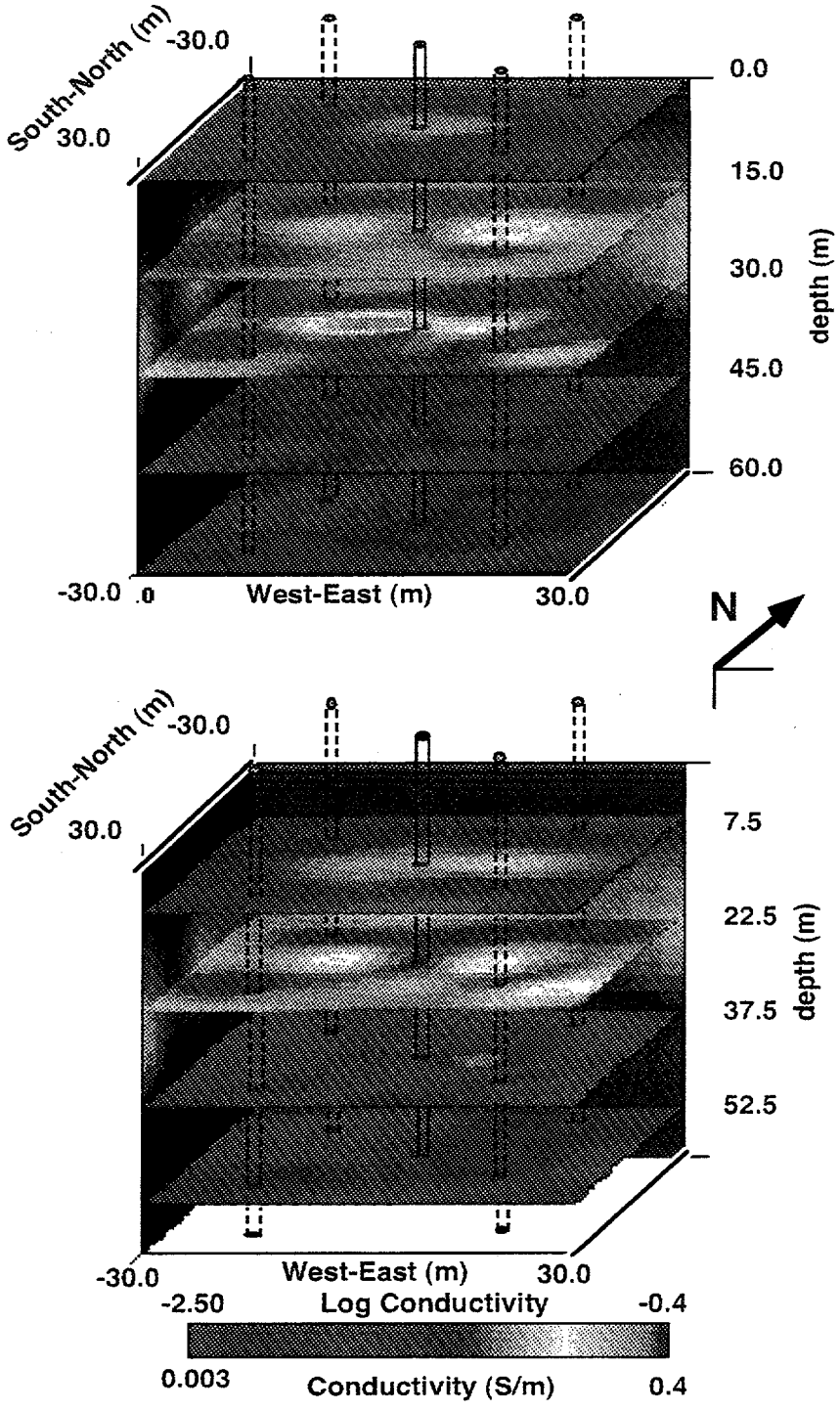


Figure 43. Conductivity reconstruction for the four well test model assuming the wells are deviated away from the injector.

# CHAPTER V

## CONCLUDING REMARKS

This report has demonstrated techniques that can be used to construct solutions to the 3-D electromagnetic inverse problem using full wave equation modeling. To this point great progress has been made in developing an inverse solution using the method of conjugate gradients which employs a 3-D finite difference solver to construct model sensitivities and predicted data. The forward modeling code has been developed to incorporate absorbing boundary conditions for high frequency solutions (radar), as well as complex electrical properties, including electrical conductivity, dielectric permittivity and magnetic permeability. In addition both forward and inverse codes have been ported to a massively parallel computer architecture which allows for more realistic solutions that can be achieved with serial machines.

While the inversion code has been demonstrated on field data collected at the Richmond-field site, techniques for appraising the quality of the reconstructions still need to be developed. Here it is suggested that rather than employing direct matrix inversion to construct the model covariance matrix which would be impossible because of the size of the problem, one can linearize about the 3-D model achieved in the inverse and use Monte-Carlo simulations to construct it.

Using these appraisal and construction tools, it is now necessary to demonstrate 3-D inversion for a variety of EM data sets that span the frequency range from induction sounding to radar: below 100 kHz to 100 MHz. Appraised 3-D images of the earth's electrical properties can provide researchers opportunities to infer the flow paths, flow rates and perhaps the chemistry of fluids in geologic mediums. It also offers a means to study the frequency dependence behavior of the properties in situ. This is of significant relevance to the Department of Energy, paramount to characterizing and monitoring of environmental waste sites and oil and gas exploration.

A key obstacle that must be overcome if 3-D inversion is to be practical is the availability of reliable parallel computing platforms. Unreliable and over-used platforms, such as the Intel Paragon, while good for designing and testing research software, are not feasible for production work. For example, typical waiting times in the queue for jobs to execute on the Paragon can be a week or more with a high probability of a system crash at any time.

## REFERENCES


Alumbaugh, D. L. and Newman G. A., 1994, Fast, frequency domain electromagnetic modeling using finite differences: 64th Ann. Intern. Mtg., Soc. Explor. Geophys., Los Angeles CA, Expanded Abstracts, 369-373.

Alumbaugh, D. L. and Morrison H. F., 1995a, Monitoring subsurface changes over time with cross-well electromagnetic tomography: Geop. Prosp., **43**, 873-902.

Alumbaugh, D.L. and Morrison, H.F., 1995b, Theoretical and practical considerations for crosswell electromagnetic tomography using a cylindrical geometry: Geophysics, **60**, 846-870.

Alumbaugh, D. L. and Newman G.A., 1995, Simulation of airborne electromagnetic measurements in three dimensional environments; proceedings of SAGEEP '95 (Symposium on the Application of Geophysics to Environmental and Engineering Problems ), Orlando, Florida, 319-328.

Barrett, R., Berry, M., Chan, T.F., Demmel, J., Donato, J., Dongarra, J., Eijkhout, V., Pozo, R., Romine, C., and van der Vorst, H., 1994, Templates for the Solution of Linear Systems: Building Blocks for Iterative Methods; Society for Industrial and Applied Mathematics.

Berenger, J., 1993, A perfectly matched layer for the absorption of electromagnetic waves: J. Comp. Phy., **114**, 185-200.

Chew, W. C., 1990, Waves and Fields in Inhomogeneous Media, Van Nostrand Reinhold International Company Limited.

Chew, W.C., and Weedon, W.H., 1994, A 3D perfectly matched medium from modified Maxwell's equations with stretched coordinates; Microwave and Optical Tech. Let.,**7**, 599-604.

Druskin, V. and Knizhnerman, L., 1988, A spectral semi-discrete method for the numerical solution of three-dimensional nonstationary problems of electric prospecting: Izvestiya, Earth Physics, **24**, 641-648.

Druskin, V. and Knizhnerman, L., 1994, A spectral approach to solving three-dimensional diffusion Maxwell's equations in the time and frequency domains: Radio Science, **29**, 937-953.

Dubois, D., Greenbaum, A., and Lewis, J., 1979, Approximating the inverse of a matrix for use in iterative algorithms on vector processors; Computing, **22**, 257-268.

Farquharson, C. G. and Oldenburg, D. W., 1995, Approximate sensitivities for the multi-dimensional electromagnetic inverse problem: Expanded abstracts of the Int. Symp. on Three-Dimensional Electromagnetics, Oct. 4-6, Schlumberger-Doll Research, Ridgefield, Connecticut, USA.

Freund, R., 1990, On conjugate gradient type methods and polynomial preconditioners for a class of complex non-Hermitian matrices; Numer. Math., **57**, 285-312.

Freund, R., 1992, Conjugate gradient type methods for linear systems with complex symmetric coefficient matrices: SIAM J. Sci. Statist. Comput., **13**, 425-448.

Habashy, T.M., Groom, R. W., and Spies, B.R., 1993, Beyond the Born and Rytov approximations: a nonlinear approach to electromagnetic scattering: J. Geophys. Res., **98**, 1759-1775.

Habashy, T. M., Torres-Verdin C. and Oristaglio M. L., 1995, An overview of recent advances in inversion of large-scale electromagnetic data: Expanded abstracts of the Int. Symp. on Three-Dimensional Electromagnetics, Oct. 4-6, Schlumberger-Doll Research, Ridgefield, Connecticut, USA.

Hestenes, M. R. and Stiefel, E., 1952, Methods of conjugate gradients for solving linear systems: J. Res. Nat. Bur. Standards, **49**, 409-435.

Katz. D.S., Thiele, E.T., and Taflove, A.,1994, Validation and extension to three dimensions of the Berenger PML absorbing boundary condition for FD-TD meshes; IEEE Micro. and Guided Wave Let., **4**, 268-270.

Lanczos, C., 1950, An iterative method for the solution of the eigenvalue problem of linear differential and integral operators; J. Res. Nat. Bur. Stand., **45**, 255 -282.

Liu, C., Shen, L.C., and Zhang, Y.C., Monitoring saltwater injection using conductivity images obtained by electromagnetic cross-hole measurements, Radio Science, **30**, 1405-1415.

McGillivray, P. R. and Oldenburg, D. W., 1990, Methods for calculating Fréchet derivatives and sensitivities for the non-linear inverse problem: Geophys. Prosp., **38**, 499-524.

Mackie, R. L. and Madden, T. R., 1993, Three-dimensional magnetotelluric inversion using conjugate gradients: Geophys. J. Int., **115**, 215-229.

Newman, G. A., Hohmann, G. W. and Anderson, W. L., 1986, Transient electromagnetic response of a three-dimensional body in a layered earth: Geophysics, **51**, 1608-1627.

Newman, G. A., 1995, Crosswell electromagnetic inversion using integral and differential equations: Geophysics, **60**, 899-911.

Newman, G. A., and Alumbaugh, D. L., 1995, Frequency-domain modeling of airborne electromagnetic responses using staggered finite differences:Geophysical Prospecting, **43**, 873-902.

Oldenburg, D. W., 1990, Inversion of electromagnetic data: an overview of new techniques: Surveys in Geophysics, **11**, 231-270.

Park, S. K., 1983, Three-dimensional magnetotelluric modeling and inversion: PhD. thesis, Mass. Inst. Tech.

Pellerin, L., Labson, V. F., and Pfeifer, M. C., 1995, VETEM - a very early time electromagnetic system; proceedings of SAGEEP '95 (Symposium on the Application of Geophysics to Environmental and Engineering Problems ), Orlando, Florida, 725-732.

Saad, Y., 1985, Practical use of polynomial preconditionings for the conjugate gradient method; SIAM J. Sci. Stat. Comput., **6**, 865-881.

Sarkar, T.K., 1987, On the application of the generalized biconjugate gradient method; J. Electro. Waves and App., **1**, 223-242.

Shadid, J.N., and Tuminaro, R.S., 1994, A comparison of preconditioned nonsymetric Krylov methods on a large-scale MIMD machine, SIAM J. Sci. Comput., **15**, 440-459.

Skjellum, A., Doss, N.E., and Bangalore, P.V., 1993, Writing libraries in MPI, *in* A. Skjellum and D. Reese, Ed., Proceedings of the Scalable Parallel Libraries Conference, IEEE Comput. Sci. Press, 166-173.

Smith, T. J., 1992, Conservative modeling of 3-D electromagnetic fields; International Association of Geomagnetism and Aeronomy, 11th Workshop on Electromagnetic Induction in the Earth, Wellington, New Zealand, Meeting Abstracts.

Stewart, D.C., Anderson, W.L., Grover, T.P., and Labson, V.F., 1994, Shallow subsurface mapping by electromagnetic sounding in the 300 khz to 30 Mhz range: model studies and prototype system assessment; Geophysics, **59**, 1201-1210.

Tikhonov, A. N. and Arsenin, V. Y., 1977, Solutions to ill-posed problems: John Wiley and Sons, Inc.

Torres-Verdín, C. and Habashy, T.M., 1994, Rapid 2.5-D forward modeling and inversion via a new nonlinear scattering approximation, Radio Science, **29**, 1051-1079.

Torres-Verdin, C. and Habashy, T, M., 1995, A two step linear inversion of two dimensional electrical conductivity: IEEE Trans. Antenna Propagat., **43**, 405-415.

Tripp, A. C. and Hohmann, G. W., 1984, Block diagonalization of the electromagnetic impedance matrix of a symmetric buried body using group theory: Inst. of Electr. and Electron. Eng., Trans. Geoscience and Remote Sensing, **GE-22**, 62-69.

Wilt, M. J, Alumbaugh, D. L., Morrison, H. F., Becker A., Lee K. H., and Deszcz-Pan M., 1995a, Crosshole electromagnetic tomography: design considerations and field results: Geophysics, **60**, 871-885.

Wilt, M., Morrison, H.F., Becker, A., Tseng, H.W., Lee, K.H., Torres-Verdin, C., and Alumbaugh, D., 1995b, Crosshole electromagnetic tomography: a new technology for oil field characterization; The Leading Edge, **14**, 173-177.

Wang T. and Hohmann, G. W., 1993, A finite difference time-domain solution for three-dimensional electromagnetic modeling: Geophysics, **58**, 797-809.

Xiong, Z., 1992, Electromagnetic modeling of 3-D structures by the method of system iteration using integral equations: Geophysics, **57**, 1556-1561.

Yee, K. S., 1966, Numerical solution of initial boundary problems involving Maxwell's equations in isotropic media: Inst. of Electr. and Electron. Eng., Trans. Ant. Prop, **AP-14**, 302-309.

Zhang, J. Mackie, R. L. and Madden, T. R., 1995, Three-dimensional resistivity forward modeling and inversion using conjugate gradients: Geophysics, **60**, 1313-1325.

Zhdanov, M. S. and Fang, S., 1995a, 3D electromagnetic inversion based on the quasi-linear approximation: Expanded abstracts of the Int. Symp. on Three-Dimensional Electromagnetics, Oct. 4-6, Schlumberger-Doll Research, Ridgefield, Connecticut, USA.

Zhdanov, M.S., and Fang, S., 1995b, Quasi linear approximation in 3-D electromagnetic modeling; Expanded abstracts of the Int. Symp. on Three-Dimensional Electromagnetics, Oct. 4-6, Schlumberger-Doll Research, Ridgefield, Connecticut, USA.

## APPENDIX A

The perfectly matched layer concept proposed in 2-D by Berenger (1993) and 3-D by Katz et al. (1994) was originally devloped for time domain simulation of Maxwell's equations. Here we demonstrate that this method is valid for the 3-D frequency domain Helmholtz equation for the scattered electric fields using the method of Chew and Weedon (1994). First we simplify equation (7) by assuming that we are at a boundary far away from any zones of anomalous electrical properties such that it can be written

$$\nabla_h \times \nabla_e \times \mathbf{E}^s + i\omega\mu_p\left(\sigma_p + i\omega\varepsilon_p\right)\mathbf{E}^s = 0. \tag{A-1}$$

Because we are far away from any anomalous zones, a possible plane wave solution to equation (A-1) along this particular boundary is given by

$$\mathbf{E}^s = \mathbf{E}_0^s e^{ik\cdot\mathbf{r}} \tag{A-2}$$

where $\boldsymbol{k} = k_x\hat{\mathbf{i}} + k_y\hat{\mathbf{j}} + k_z\hat{\mathbf{k}}$ and $\mathbf{r} = x\hat{\mathbf{i}} + y\hat{\mathbf{j}} + z\hat{\mathbf{k}}$. Because $\nabla \times \mathbf{E}_0^s e^{ik\cdot\mathbf{r}} = i\boldsymbol{k} \times \mathbf{E}_0^s e^{ik\cdot\mathbf{r}}$, it is easy to show that when equation (A-2) is substituted into (A-1), the resulting expression has the form

$$-\boldsymbol{k}_h \times \boldsymbol{k}_e \times \mathbf{E}^s + i\omega\mu_p\left(\sigma_p + i\omega\varepsilon_p\right)\mathbf{E}^s = 0 \tag{A-3}$$

where

$$\boldsymbol{k}_e = \frac{k_x}{e_x}\hat{\mathbf{i}} + \frac{k_y}{e_y}\hat{\mathbf{j}} + \frac{k_z}{e_z}\hat{\mathbf{k}} \tag{A-4}$$

and

$$\boldsymbol{k}_h = \frac{k_x}{h_x}\hat{\mathbf{i}} + \frac{k_y}{h_y}\hat{\mathbf{j}} + \frac{k_z}{h_z}\hat{\mathbf{k}}. \tag{A-5}$$

Using a vector identity, the left hand term in equation (A-3) can be expanded to yield

$$\left(\boldsymbol{k}_h \cdot \boldsymbol{k}_e\right)\mathbf{E}^s - \boldsymbol{k}_e\left(\boldsymbol{k}_h \cdot \mathbf{E}^s\right) + i\omega\mu_p\left(\sigma_p + i\omega\varepsilon_p\right)\mathbf{E}^s = 0. \tag{A-6}$$

Because we are in a homogenous region absent of any free 'secondary' charge,

$$\nabla_h \cdot \mathbf{E}^s = \boldsymbol{k}_h \cdot \mathbf{E}^s = 0 \tag{A-7}$$

and thus we are left with

$$(\boldsymbol{k}_h \cdot \boldsymbol{k}_e)\mathbf{E}^s + i\omega\mu_p(\sigma_p + i\omega\varepsilon_p)\mathbf{E}^s = 0 \tag{A-8}$$

or

$$\boldsymbol{k}_h \cdot \boldsymbol{k}_e = \frac{1}{e_x h_x}k_x^2 + \frac{1}{e_y h_y}k_y^2 + \frac{1}{e_z h_z}k_z^2 = \kappa^2 \tag{A-9}$$

where $\kappa^2 = -i\omega\mu_p(\sigma_p + i\omega\varepsilon_p)$.

Let us now assume that the plane wave is obliquely incident on an interface at z=c where c is constant. Chew and Weedon (1994) show that the solution to equation (A-9) is that of a 3-D ellipsoid which is satisfied by

$$k_x = \kappa\sqrt{e_x h_x}\sin\theta\cos\phi \tag{A-10}$$

$$k_y = \kappa\sqrt{e_y h_y}\sin\theta\sin\phi \tag{A-11}$$

and

$$k_z = \kappa\sqrt{e_z h_z}\cos\theta. \tag{A-12}$$

In addition they find the reflection coefficients for the TE and TM modes at the boundary to be

$$R^{TE} = \frac{k_{1z}e_{2z}\mu_2 - k_{2z}e_{1z}\mu_1}{k_{1z}e_{2z}\mu_2 + k_{2z}e_{1z}\mu_1} \tag{A-13}$$

and

$$R^{TM} = \frac{k_{1z}h_{2z}\hat{y}_2 - k_{2z}h_{1z}\hat{y}_1}{k_{1z}h_{2z}\hat{y}_2 + k_{2z}h_{1z}\hat{y}_1} \tag{A-14}$$

where the 1's represent the properties of medium the incident wave is traveling through, the 2's designates the medium it will be transmitted to, and $\hat{y}_i = \sigma_i + i\omega\varepsilon_i$.

Phase matching will occur if $k_{1x} = k_{2x}$ and $k_{1y} = k_{2y}$. To accomplish this we first set the material properties of the two media to be identical ($\kappa_1 = \kappa_2$)and then choose $h_x = e_x$ and $h_y = e_y$. If we now let $e_{1x} = e_{2x} = e_{1y} = e_{2y}$=1, and furthermore set $\theta_1 = \theta_2$ and $\phi_1 = \phi_2$, then the two reflection coefficients in (A-13) and (A-14) are zero and no reflections are generated at the interface. However by making $e_{2z}$ complex, we provide additional loss in $k_{2z}$ which causes the wave to more rapidly attenuate in medium 2 than it would otherwise.

It must be mentioned that three assumptions have been made in this analysis which can not be incoporated into the 3-D FD modeling scheme. The first assumption is that $e_x, e_y, h_x$ and $h_y$ do not vary along the 'z' interface. In the corners of the mesh these values are also varying to incoporate absorption along the x and y interfaces, and thus perfect matching can not occur in these locations and reflections will be generated. However we have not experienced any serious problems with regards to this phenomenon. The second assumption that we have made here is that the interface is located far away from any regions of anomalous electrical properties. Nevertheless as the results in Figure 10d and 10e indicate, the PML is valid even when the stretching occurs within these regions, for instance at the mesh boundary located at the bottom of the model shown in Figure 10a. Finally, it is assumed that $h_j = e_j$ for j=x,y,and z. As shown in Appendix C, $h_j$ is actually a weighted average of the $e_j$ values assigned to two adjacent cells where the weighting depends on the cell dimensions. However by using both a constant value of $e_j$ and a constant cell size throughout the PML region, any problems with this assumption can be avoided.

## APPENDIX B

To develop an expression for the modified Helmholtz equation for the scattered electric fields we start with the modified Maxwell's equations given in expressions (1) and (2) where the modified derivative operators are given by expressions (3) and (4). We now define the primary, or background fields that exist in the stretched system to be

$$\nabla_e \times \mathbf{E^p} = -i\omega\mu_p \mathbf{H^p} - i\omega \mathbf{M^p} \tag{B-1}$$

and

$$\nabla_h \times \mathbf{H^p} = \left(\sigma_p + i\omega\varepsilon_p\right)\mathbf{E^p} + \mathbf{J^p}. \tag{B-2}$$

Subtracting (B-1) from (1), (B-2) from (2), and adding and subtracting an arbitrary source term to each equation yields

$$\nabla_e \times \mathbf{E^s} = -i\omega\mu \mathbf{H^t} + i\omega\mu_p \mathbf{H^p} + \left(i\omega\mu \mathbf{H^p} - i\omega\mu \mathbf{H^p}\right) \tag{B-3}$$

and

$$\nabla_h \times \mathbf{H^s} = (\sigma + i\omega\varepsilon)\mathbf{E^t} - \left(\sigma_p + i\omega\varepsilon_p\right)\mathbf{E^p} + \left[(\sigma + i\omega\varepsilon)\mathbf{E^p} - (\sigma + i\omega\varepsilon)\mathbf{E^p}\right]. \tag{B-4}$$

Properly subtracting the source terms yields the modified versions of Maxwell's equations for the scattered fields:

$$\nabla_e \times \mathbf{E^s} = -i\omega\mu \mathbf{H^s} - i\omega\left(\mu - \mu_p\right)\mathbf{H^p} \tag{B-5}$$

and

$$\nabla_h \times \mathbf{H^s} = (\sigma + i\omega\varepsilon)\mathbf{E^s} + \left(\sigma - \sigma_p + i\omega(\varepsilon - \varepsilon_p)\right)\mathbf{E^p}. \tag{B-6}$$

To derive the modified Helmholtz equation from these two equations, for numerical stability we first multiply (B-5) by $\mu_p/\mu$ to yield

$$\frac{\mu_p}{\mu}\nabla_e \times \mathbf{E^s} = -i\omega\mu \mathbf{H^s} - i\omega\mu_p \frac{\left(\mu - \mu_p\right)}{\mu}\mathbf{H^p}. \tag{B-7}$$

Taking the curl of (B-7) results in the following expression;

$$\nabla_h \times \frac{\mu_p}{\mu} \nabla_e \times \mathbf{E}^s = -i\omega\mu \nabla_h \times \mathbf{H}^s - i\omega\mu_p \nabla_h \times \left[ \frac{(\mu - \mu_p)}{\mu} \mathbf{H}^p \right]. \qquad \text{(B-8)}$$

Finally, the right hand side of equation (B-6) is substituted for the $\nabla_h \times \mathbf{H}^s$ term in the above equation to arrive at the modified Helmholtz equation given in expression (7).

## APPENDIX C

To develop the finite difference equations we start with the modified Helmholtz equation as given if equation (7). First let us expand out the two first order curl operators, i.e.,

$$\nabla_e \times \mathbf{E}^s = \left(\frac{1}{e_y}\frac{\partial Ez^s}{\partial y} - \frac{1}{e_z}\frac{\partial Ey^s}{\partial z}\right)\hat{\mathbf{i}} + \left(\frac{1}{e_z}\frac{\partial Ex^s}{\partial z} - \frac{1}{e_x}\frac{\partial Ez^s}{\partial x}\right)\hat{\mathbf{j}} + \left(\frac{1}{e_x}\frac{\partial Ey^s}{\partial x} - \frac{1}{e_y}\frac{\partial Ex^s}{\partial y}\right)\hat{\mathbf{k}} \tag{C-1}$$

and

$$\nabla_h \times \left[\frac{(\mu - \mu_p)}{\mu}\mathbf{H}^p\right] = \left(\frac{1}{h_y}\frac{\partial}{\partial y}\frac{(\mu_z - \mu_p)Hz^p}{\mu_z} - \frac{1}{h_z}\frac{\partial}{\partial z}\frac{(\mu_y - \mu_p)Hy^p}{\mu_y}\right)\hat{\mathbf{i}} + \left(\frac{1}{h_z}\frac{\partial}{\partial z}\frac{(\mu_x - \mu_p)Hx^p}{\mu_x} - \frac{1}{h_x}\frac{\partial}{\partial x}\frac{(\mu_z - \mu_p)Hz^p}{\mu_z}\right)\hat{\mathbf{j}} + \left(\frac{1}{h_x}\frac{\partial}{\partial x}\frac{(\mu_y - \mu_p)Hy^p}{\mu_y} - \frac{1}{h_y}\frac{\partial}{\partial y}\frac{(\mu_x - \mu_p)Hx^p}{\mu_x}\right)\hat{\mathbf{k}}. \tag{C-2}$$

In this expression, $\mu_w$ for w=x,y,and z represents the magnetic permeability that is averaged across the face of two cells in the w'th direction. Next, expanding the second order curl on the left side of equation (7) we find that

$$\begin{aligned}\nabla_h \times \left[\frac{\mu_p}{\mu}\nabla_e \times \mathbf{E}^s\right] = {} & \left(\frac{1}{h_y}\frac{\partial}{\partial y}\left(\frac{\mu_p}{\mu_z e_x}\frac{\partial Ey^s}{\partial x}\right) - \frac{1}{h_y}\frac{\partial}{\partial y}\left(\frac{\mu_p}{\mu_z e_y}\frac{\partial Ex^s}{\partial y}\right) - \right. \\ & \left. \frac{1}{h_z}\frac{\partial}{\partial z}\left(\frac{\mu_p}{\mu_y e_z}\frac{\partial Ex^s}{\partial z}\right) + \frac{1}{h_z}\frac{\partial}{\partial z}\left(\frac{\mu_p}{\mu_y e_x}\frac{\partial Ez^s}{\partial x}\right)\right]\hat{\mathbf{i}} + \\ & \left[\frac{1}{h_z}\frac{\partial}{\partial z}\left(\frac{\mu_p}{\mu_x e_y}\frac{\partial Ez^s}{\partial y}\right) + \frac{1}{h_z}\frac{\partial}{\partial z}\left(\frac{\mu_p}{\mu_x e_z}\frac{\partial Ey^s}{\partial z}\right) - \right. \\ & \left. \frac{1}{h_x}\frac{\partial}{\partial x}\left(\frac{\mu_p}{\mu_z e_x}\frac{\partial Ey^s}{\partial x}\right) + \frac{1}{h_x}\frac{\partial}{\partial x}\left(\frac{\mu_p}{\mu_z e_y}\frac{\partial Ex^s}{\partial y}\right)\right]\hat{\mathbf{j}} + \\ & \left[\frac{1}{h_x}\frac{\partial}{\partial x}\left(\frac{\mu_p}{\mu_y e_z}\frac{\partial Ex^s}{\partial z}\right) + \frac{1}{h_x}\frac{\partial}{\partial x}\left(\frac{\mu_p}{\mu_y e_x}\frac{\partial Ez^s}{\partial x}\right) - \right. \\ & \left. \frac{1}{h_y}\frac{\partial}{\partial y}\left(\frac{\mu_p}{\mu_x e_y}\frac{\partial Ez^s}{\partial y}\right) + \frac{1}{h_y}\frac{\partial}{\partial y}\left(\frac{\mu_p}{\mu_x e_z}\frac{\partial Ey^s}{\partial z}\right)\right]\hat{\mathbf{k}}.\end{aligned} \tag{C-3}$$

Now let us examine the parts of the Helmholtz equation corresponding to $\hat{\mathbf{i}}$, $\hat{\mathbf{j}}$, and $\hat{\mathbf{k}}$ separately since these are the three equations that we are going to be solving at each node. For the $\hat{\mathbf{i}}$ component we have

$$\frac{1}{h_y}\frac{\partial}{\partial y}\left(\frac{\mu_p}{\mu_z e_x}\frac{\partial Ey^s}{\partial x}\right)-\frac{1}{h_y}\frac{\partial}{\partial y}\left(\frac{\mu_p}{\mu_z e_y}\frac{\partial Ex^s}{\partial y}\right)-\frac{\mu_p}{h_z}\frac{\partial}{\partial z}\left(\frac{1}{\mu_y e_z}\frac{\partial Ex^s}{\partial z}\right)+ \tag{C-4}$$

$$\frac{1}{h_z}\frac{\partial}{\partial z}\left(\frac{\mu_p}{\mu_y e_x}\frac{\partial Ez^s}{\partial x}\right)+i\omega\mu_p(\sigma+i\omega\varepsilon)Ex^s=-i\omega\mu_p\left(\sigma-\sigma_p+i\omega\left(\varepsilon-\varepsilon_p\right)\right)Ex^p-$$

$$\frac{i\omega\mu_p}{h_y}\frac{\partial}{\partial y}\frac{\left(\mu_z-\mu_p\right)Hz^p}{\mu_z}-\frac{i\omega\mu_p}{h_z}\frac{\partial}{\partial z}\frac{\left(\mu_y-\mu_p\right)Hy^p}{\mu_y}.$$

Approximating equation (C-4) with finite differences yields

$$\left\{\frac{\mu_p}{\mu_{z_{i+\frac{1}{2},j+\frac{1}{2},k}}}\left[\frac{1}{\left(e_{xi}\Delta x_i\right)}\left(Ey^s_{i+1,j+\frac{1}{2},k}-Ey^s_{i,j+\frac{1}{2},k}\right)-\frac{1}{\left(e_{yj}\Delta y_j\right)}\left(Ex^s_{i+\frac{1}{2},j+1,k}-Ex^s_{i+\frac{1}{2},j,k}\right)\right]-\right.$$

$$\left.\frac{\mu_p}{\mu_{z_{i+\frac{1}{2},j-\frac{1}{2},k}}}\left[\frac{1}{\left(e_{xi}\Delta x_i\right)}\left(Ey^s_{i+1,j-\frac{1}{2},k}-Ey^s_{i,j-\frac{1}{2},k}\right)-\frac{1}{\left(e_{yj-1}\Delta y_{j-1}\right)}\left(Ex^s_{i+\frac{1}{2},j,k}-Ex^s_{i+\frac{1}{2},j-1,k}\right)\right]\right\}\frac{1}{\left(h_{yj}\Delta\bar{y}_j\right)}+$$

$$\left\{\frac{\mu_p}{\mu_{y_{i+\frac{1}{2},j,k+\frac{1}{2}}}}\left[\frac{1}{\left(e_{xi}\Delta x_i\right)}\left(Ez^s_{i+1,j,k+\frac{1}{2}}-Ez^s_{i,j,k+\frac{1}{2}}\right)-\frac{1}{\left(e_{zk}\Delta z_k\right)}\left(Ex^s_{i+\frac{1}{2},j,k+1}-Ex^s_{i+\frac{1}{2},j,k}\right)\right]-\right.$$

$$\left.\frac{\mu_p}{\mu_{y_{i+\frac{1}{2},j,k-\frac{1}{2}}}}\left[\frac{1}{\left(e_{xi}\Delta x_i\right)}\left(Ez^s_{i+1,j,k-\frac{1}{2}}-Ez^s_{i,j,k-\frac{1}{2}}\right)-\frac{1}{\left(e_{zk-1}\Delta z_{k-1}\right)}\left(Ex^s_{i+\frac{1}{2},j,k}-Ex^s_{i+\frac{1}{2},j,k-1}\right)\right]\right\}\frac{1}{\left(h_{zk}\Delta\bar{z}_k\right)}+$$

$$i\omega\mu_p\hat{y}_p Ex^s_{i+\frac{1}{2},j,k}=-i\omega\mu_p\left(\hat{y}_{i+\frac{1}{2},j,k}-\hat{y}_p\right)Ex^p_{i+\frac{1}{2},j,k}- \tag{C-5}$$

$$i\omega\mu_p\left\{\left[\frac{\left(\mu_{y_{i+\frac{1}{2},j,k+\frac{1}{2}}}-\mu_p\right)}{\mu_{y_{i+\frac{1}{2},j,k+\frac{1}{2}}}}Hy^p_{i+\frac{1}{2},j,k+\frac{1}{2}}-\frac{\left(\mu_{y_{i+\frac{1}{2},j,k-\frac{1}{2}}}-\mu_p\right)}{\mu_{y_{i+\frac{1}{2},j,k-\frac{1}{2}}}}Hy^p_{i+\frac{1}{2},j,k-\frac{1}{2}}\right]\frac{1}{\left(h_{zk}\Delta\bar{z}_k\right)}-\right.$$

$$\left.\left[\frac{\left(\mu_{z_{i+\frac{1}{2},j+\frac{1}{2},k}}-\mu_p\right)}{\mu_{z_{i+\frac{1}{2},j+\frac{1}{2},k}}}Hz^p_{i+\frac{1}{2},j+\frac{1}{2},k}-\frac{\left(\mu_{z_{i+\frac{1}{2},j-\frac{1}{2},k}}-\mu_p\right)}{\mu_{z_{i+\frac{1}{2},j-\frac{1}{2},k}}}Hz^p_{i+\frac{1}{2},j-\frac{1}{2},k}\right]\frac{1}{\left(h_{yj}\Delta\bar{y}_j\right)}\right\}$$

where now $\hat{y} = \sigma + i\omega\varepsilon$. In this expression $\Delta w_l$ for w=x,y,z and l=i,j,k represents the width of the l'th cell in the w'th direction. Similarly $\Delta\overline{w}_l$ is the distance in the w'th direction between the centers of cells l and l-1. Notice in this expression how the finite differences and the stretching parameters conveniently group together. It is also apparent that because $\Delta\overline{w}_l$ is essentially the weighted average of the widths of cells l and l-1, $h_{wl}$ is the weighted average of $e_{wl}$ and $e_{wl-1}$.

We can similarly expand the equations for the $\hat{\mathbf{j}}$ and $\hat{\mathbf{k}}$ terms which yields

$$\left\{\frac{\mu_p}{\mu_{x_{i,j+\frac{1}{2},k+\frac{1}{2}}}}\left[\frac{1}{\left(e_{yj}\Delta y_j\right)}\left(Ez^s_{i,j+1,k+\frac{1}{2}} - Ez^s_{i,j,k+\frac{1}{2}}\right) - \frac{1}{\left(e_{zk}\Delta z_k\right)}\left(Ey^s_{i,j+\frac{1}{2},k+1} - Ey^s_{i,j+\frac{1}{2},k}\right)\right] - \right.$$

$$\left.\frac{\mu_p}{\mu_{x_{i,j+\frac{1}{2},k-\frac{1}{2}}}}\left[\frac{1}{\left(e_{yj}\Delta y_j\right)}\left(Ez^s_{i,j+1,k-\frac{1}{2}} - Ez^s_{i,j,k-\frac{1}{2}}\right) + \frac{1}{\left(e_{zk-1}\Delta z_{k-1}\right)}\left(Ey^s_{i,j+\frac{1}{2},k} - Ey^s_{i,j+\frac{1}{2},k-1}\right)\right]\right\}\frac{1}{\left(h_{zk}\Delta\overline{z}_k\right)} +$$

$$\left\{\frac{\mu_p}{\mu_{z_{i+\frac{1}{2},j+\frac{1}{2},k}}}\left[\frac{1}{\left(e_{yj}\Delta y_j\right)}\left(Ex^s_{i+\frac{1}{2},j+1,k} - Ex^s_{i+\frac{1}{2},j,k}\right) - \frac{1}{\left(e_{xi}\Delta x_i\right)}\left(Ey^s_{i+1,j+\frac{1}{2},k} - Ey^s_{i,j+\frac{1}{2},k}\right)\right] - \right.$$

$$\left.\frac{\mu_p}{\mu_{z_{i-\frac{1}{2},j+\frac{1}{2},k}}}\left[\frac{1}{\left(e_{yj}\Delta y_j\right)}\left(Ex^s_{i-\frac{1}{2},j+1,k} - Ex^s_{i-\frac{1}{2},j,k}\right) - \frac{1}{\left(e_{xi-1}\Delta x_{i-1}\right)}\left(Ey^s_{i,j+\frac{1}{2},k} - Ey^s_{i-1,j+\frac{1}{2},k}\right)\right]\right\}\frac{1}{\left(h_{xi}\Delta\overline{x}_i\right)} +$$

$$i\omega\mu_p\hat{y}_p Ey^s_{i,j+\frac{1}{2},k} = -i\omega\mu_p\left(\hat{y}_{i,j+\frac{1}{2},k} - \hat{y}_p\right)Ey^p_{i,j+\frac{1}{2},k} - \tag{C-6}$$

$$i\omega\mu_p\left\{\left[\frac{\left(\mu_{x_{i,j+\frac{1}{2},k+\frac{1}{2}}} - \mu_p\right)}{\mu_{x_{i,j+\frac{1}{2},k+\frac{1}{2}}}}Hx^p_{i,j+\frac{1}{2},k+\frac{1}{2}} - \frac{\left(\mu_{x_{i,j+\frac{1}{2},k-\frac{1}{2}}} - \mu_p\right)}{\mu_{x_{i,j+\frac{1}{2},k-\frac{1}{2}}}}Hx^p_{i,j+\frac{1}{2},k-\frac{1}{2}}\right]\frac{1}{\left(h_{zk}\Delta\overline{z}_k\right)} - \right.$$

$$\left.\left[\frac{\left(\mu_{z_{i+\frac{1}{2},j+\frac{1}{2},k}} - \mu_p\right)}{\mu_{z_{i+\frac{1}{2},j+\frac{1}{2},k}}}Hz^p_{i+\frac{1}{2},j+\frac{1}{2},k} - \frac{\left(\mu_{z_{i-\frac{1}{2},j+\frac{1}{2},k}} - \mu_p\right)}{\mu_{z_{i-\frac{1}{2},j+\frac{1}{2},k}}}Hz^p_{i-\frac{1}{2},j+\frac{1}{2},k}\right]\frac{1}{\left(h_{xi}\Delta\overline{x}_i\right)}\right\}$$

and

$$\left\{\frac{\mu_p}{\mu_{y_{i+\frac{1}{2},j,k+\frac{1}{2}}}}\left[\frac{1}{(e_{zk}\Delta z_k)}\left(Ex^s_{i+\frac{1}{2},j,k+1}-Ex^s_{i+\frac{1}{2},j,k}\right)-\frac{1}{(e_{xi}\Delta x_i)}\left(Ez^s_{i+1,j,k+\frac{1}{2}}-Ez^s_{i,j,k+\frac{1}{2}}\right)\right]-\right.$$

$$\left.\frac{\mu_p}{\mu_{y_{i-\frac{1}{2},j,k+\frac{1}{2}}}}\left[\frac{1}{(e_{zk}\Delta z_k)}\left(Ex^s_{i-\frac{1}{2},j,k+1}-Ex^s_{i-\frac{1}{2},j,k}\right)-\frac{1}{(e_{xi-1}\Delta x_{i-1})}\left(Ez^s_{i,j,k+\frac{1}{2}}-Ez^s_{i-1,j,k+\frac{1}{2}}\right)\right]\right\}\frac{1}{(h_{xi}\Delta\bar{x}_i)}+$$

$$\left\{\frac{\mu_p}{\mu_{x_{i,j+\frac{1}{2},k+\frac{1}{2}}}}\left[\frac{1}{(e_{zk}\Delta z_k)}\left(Ey^s_{i,j+\frac{1}{2},k+1}-Ey^s_{i,j+\frac{1}{2},k}\right)-\frac{1}{(e_{yj}\Delta y_j)}\left(Ez^s_{i,j+1,k+\frac{1}{2}}-Ez^s_{i,j,k+\frac{1}{2}}\right)\right]-\right.$$

$$\left.\frac{\mu_p}{\mu_{x_{i,j-\frac{1}{2},k+\frac{1}{2}}}}\left[\frac{1}{(e_{zk}\Delta z_k)}\left(Ey^s_{i,j-\frac{1}{2},k+1}-Ey^s_{i,j-\frac{1}{2},k}\right)-\frac{1}{(e_{yj-1}\Delta y_{j-1})}\left(Ez^s_{i,j,k+\frac{1}{2}}-Ez^s_{i,j-1,k+\frac{1}{2}}\right)\right]\right\}\frac{1}{(h_{yj}\Delta\bar{y}_j)}+$$

$$i\omega\mu_p\hat{y}_p Ez^s_{i,j,k+\frac{1}{2}}=-i\omega\mu_p\left(\hat{y}_{i,j,k+\frac{1}{2}}-\hat{y}_p\right)Ez^p_{i,j,k+\frac{1}{2}}- \tag{C-7}$$

$$i\omega\mu_p\left\{\left[\frac{\left(\mu_{x_{i,j+\frac{1}{2},k+\frac{1}{2}}}-\mu_p\right)}{\mu_{x_{i,j+\frac{1}{2},k+\frac{1}{2}}}}Hx^p_{i,j+\frac{1}{2},k+\frac{1}{2}}-\frac{\left(\mu_{x_{i,j-\frac{1}{2},k+\frac{1}{2}}}-\mu_p\right)}{\mu_{x_{i,j-\frac{1}{2},k+\frac{1}{2}}}}Hx^p_{i,j-\frac{1}{2},k+\frac{1}{2}}\right]\frac{1}{(h_{yj}\Delta\bar{y}_j)}-\right.$$

$$\left.\left[\frac{\left(\mu_{y_{i+\frac{1}{2},j,k+\frac{1}{2}}}-\mu_p\right)}{\mu_{y_{i+\frac{1}{2},j,k+\frac{1}{2}}}}Hy^p_{i+\frac{1}{2},j,k+\frac{1}{2}}-\frac{\left(\mu_{y_{i-\frac{1}{2},j,k+\frac{1}{2}}}-\mu_p\right)}{\mu_{y_{i-\frac{1}{2},j,k+\frac{1}{2}}}}Hy^p_{i-\frac{1}{2},j,k+\frac{1}{2}}\right]\frac{1}{(h_{xi}\Delta\bar{x}_i)}\right\}$$

respectively. Unfortunately the above equations will not produce a symmetric matrix. Thus symmetric scaling must be applied with equation (C-5) being multiplied by $(e_{xi}\Delta x_i)(h_{yj}\Delta\bar{y}_j)(h_{zk}\Delta\bar{z}_k)$, equation (C-6) by $(h_{xi}\Delta\bar{x}_i)(e_{yj}\Delta y_j)(h_{zk}\Delta\bar{z}_k)$, and (C-7) by $(h_{xi}\Delta\bar{x}_i)(h_{yj}\Delta\bar{y}_j)(e_{zk}\Delta z_k)$.

## APPENDIX D

The inverse problem can be formulated to allow for positive parameters with a lower bounding constraint by using a log parameterization. To accomplish this we first define a perturbation in the model as

$$\delta(\mathbf{m}^{(i)}) = (\mathbf{m}-\mathbf{m}^{(i)}) \tag{D1}$$

and then use the differential form of the natural log function to write

$$\delta(\mathbf{m}^{(i)}) = (\mathbf{m}^{(i)}-\epsilon)\, \delta\ln(\mathbf{m}-\epsilon), \tag{D2}$$

where

$$\delta\ln(\mathbf{m}-\epsilon) = \ln((\mathbf{m}-\epsilon)) - \ln(\mathbf{m}^{(i)}-\epsilon)), \tag{D3}$$

with $\mathbf{m}$ and $\mathbf{m}^{(i)} > \epsilon$, and $\epsilon > 0$. Following the form of equation (20) and using equations (D1), (D2) and (D3) we can define a new functional,

$$S' = [(\mathbf{D}((\mathbf{d}-\mathbf{d}^{p(i)})-\mathbf{A}'^{p(i)}\delta\ln(\mathbf{m}-\epsilon)))^t\, (\mathbf{D}((\mathbf{d}-\mathbf{d}^{p(i)})-\mathbf{A}'^{p(i)}\delta\ln(\mathbf{m}-\epsilon))) - \chi^2] + \lambda(\mathbf{W}\ln(\mathbf{m}-\epsilon))^t(\mathbf{W}\ln(\mathbf{m}-\epsilon)), \tag{D4}$$

where the modified Jacobian matrix $\mathbf{A}'^{p(i)}$ is obtained by multiplying by columns of the original matrix with elements of the vector $(\mathbf{m}^{(i)}-\epsilon)$. Minimizing the above expression with respect to $\ln((\mathbf{m}-\epsilon))$, enforces the lower bound positivity constraint, where

$$\ln(\mathbf{m}-\epsilon) = [(\mathbf{D}\mathbf{A}'^{p(i)})^t\, (\mathbf{D}\mathbf{A}'^{p(i)}) + \lambda(\mathbf{W})^t(\mathbf{W})]^{-1}\, (\mathbf{D}\mathbf{A}'^{p(i)})^t\, (\mathbf{D}\delta\mathbf{d}'^{(i)}) \tag{D5}$$

and

$$\delta\mathbf{d}'^{(i)} = (\mathbf{d} - \mathbf{d}^{p(i)} + \mathbf{A}'^{p(i)}\ln(\mathbf{m}^{(i)}-\epsilon)). \tag{D6}$$

Once $\ln(\mathbf{m}-\epsilon)$ is determined, the parameters themselves follow from the expression

$$\mathbf{m} = e^{\ln(\mathbf{m}-\epsilon)} + \epsilon. \tag{D7}$$

With this new formulation, the inversion process is designed to deliver smooth estimates of $\ln(\mathbf{m}-\epsilon)$. Nevertheless, with a prudent selection of the regularization parameter, we can also expect smooth reconstructions for the model parameters, $\mathbf{m}$, themselves.

## APPENDIX E

Computational efficient and compact forms of the two matrix-vector multiplies are necessary if the inversion is to be practical. Consider fully expressing the matrix vector multiply in equation (28) as,

$$y_j = \sum_{k=1}^{M} D_{jj} A_{jk} u_k, \tag{E1}$$

where the summation is over M electrical parameters. The entry $D_{jj}$ is the jth entry of the data weighting matrix and $A_{jk}$ is an element of the Jacobian matrix. These elements are assumed to be real valued, where real and imaginary components are treated as separate elements. Because the real and imaginary components of the Jacobian matrix are jointly expressed in equation (27) as

$$\partial d_j/\partial m_k = \mathbf{g}_j^t \mathbf{K}^{-1}(\partial s/\partial m_k - \partial \mathbf{K}/\partial m_k \mathbf{E}_s), \tag{E2}$$

we can redefine the data weighting matrix, **D**, to be complex to arrive at the following expression for the first matrix-vector multiply:

$$y_j = \mathrm{Cmplx}(\mathrm{Re}(\mathbf{g}_j^t \mathbf{K}^{-1} \sum_{k=1}^{M} u_k(\partial s/\partial m_k - \partial \mathbf{K}/\partial m_k \mathbf{E}_s))\mathrm{Re}(D_{jj}),$$

$$\mathrm{Im}(\mathbf{g}_j^t \mathbf{K}^{-1} \sum_{k=1}^{M} u_k(\partial s/\partial m_k - \partial \mathbf{K}/\partial m_k \mathbf{E}_s))\mathrm{Im}(D_{jj})), \tag{E3}$$

where $y_j$ is now assumed to be complex instead of real.

The second matrix-vector multiply in equation (29) can be expressed as

$$z_k = \sum_{j=1}^{2N} A_{jk} D_{jj} y_j, \qquad \text{(E4)}$$

where 2N is the number of data used in the inversion and where components subscripts j=1,N correspond to real entries while components j=N+1,2N correspond to imaginary ones; note quantities, $D_{jj}$ and $y_j$ are regarded as real valued by this splitting. By associating real and imaginary components as a joint term in the above summation, we can also express equation (E4) as

$$z_k = \sum_{j=1}^{N} (A_{jk} D_{jj} y_j + A_{j+N\,k} D_{j+N\,j+N} y_{j+N}). \qquad \text{(E5)}$$

Next combining elements as cmplx($A_{jk}$,$A_{j+N\,k}$), cmplx($D_{jj}$,$D_{j+N\,j+N}$) and cmplx($y_j$,$y_{j+N}$) and because $z_k$ must always be real, we find

$$z_k = \mathrm{Re} \sum_{j=1}^{N} \mathrm{cmplx}(D_{jj} y_j, D_{j+N\,j+N} y_{j+N})^* \, \mathrm{cmplx}(A_{jk}, A_{j+N\,k}), \qquad \text{(E6)}$$

where '*' stands for complex conjugation. By treating $A_{jk}$, $D_{jj}$ and $y_j$ as complex and using equation (E2), we finally arrive at

$$z_k = \mathrm{Re}(\sum_{j=1}^{N} \mathrm{Cmplx}(\mathrm{Re}(D_{jj})\,\mathrm{Re}(y_j), \mathrm{Im}(D_{jj})\,\mathrm{Im}(y_j))^* (g_i^t K^{-1} (\partial s/\partial m_k - \partial K/\partial m_k E_s))). \qquad \text{(E7)}$$

## APPENDIX F

To show that the vector $\partial s/\partial m_k$ and matrix $\partial K/\partial m_k$ each has 12 non-zero entries, we start with the vector Helmholtz equation for the scattered electric field, $\mathbf{E}_s$, (equation (7)), but we will modify it such that magnetic permeability changes from free space, $\mu_0$, are minimal. Thus,

$$\nabla \times \nabla \times \mathbf{E}_s(\mathbf{r}) + i\omega\mu_0(\sigma(\mathbf{r})+i\omega\epsilon(\mathbf{r}))\mathbf{E}_s(\mathbf{r}) = -i\omega\mu_0\mathbf{J}_s(\mathbf{r}), \tag{F1}$$

with the source of the scattering given by

$$\mathbf{J}_s(\mathbf{r})=\{(\sigma(\mathbf{r})-\sigma^b(\mathbf{r})) +i\omega(\epsilon(\mathbf{r})-\epsilon^b(\mathbf{r}))\}\mathbf{E}^b(\mathbf{r}). \tag{F2}$$

Here we have assumed an $e^{i\omega t}$ time dependence with $i=\sqrt{-1}$, where $\omega$ represents the angular frequency. In equations (F1) and (F2) the 3-D conductivity and permittivity variations are given by $\sigma(\mathbf{r})$ and $\epsilon(\mathbf{r})$, with $\sigma^b(\mathbf{r})$ and $\epsilon^b(\mathbf{r})$ representing the corresponding background properties, which for purposes here are either a whole space or a layered space. The electric field of the background media, $\mathbf{E}^b(\mathbf{r})$, drives the source vector, and arises from an impressed dipole source.

The scattered fields are determined by imposing a staggered finite difference approximation on equation (F1), using a rectangular grid with a Dirichlet boundary condition. Each cell in this grid has a conductivity and dielectric permittivity assigned to it, where the scattered and source fields are sampled at the edges of the cell as illustrated in Figure 20. Because of this sampling scheme the averaged electrical properties have to be determined at the cell edges (refer to Chapter II for the details). These averages can be evaluated by tracing out a line integral of the magnetic field centered on the midpoint of the cell edge. The resulting average conductivity and permittivity are simply a weighted sum of the conductivities and permittivities of the four adjoining cells, where the weighting is based on the area of each cell that is bounded by the line integral. This is simple application of Ampere's Law. A study of Figure 20 shows that with the twelve field samples, equations (F1) and (F2) will require 12 averages of conductivity and permittivity, with each average involving the conductivity and permittivity of the indicated cell. Since with every field sample, we have one equation in the linear system, $\mathbf{KE}_s = \mathbf{s}$, where $\mathbf{s} = \mathbf{J}_s$, it follows that $\partial s/\partial m_k$ and the matrix $\partial K/\partial m_k$ each have 12 non-zero entries.

**Distribution:**

1 University of Arizona
MGE Dept. Bldg. #12
Attn: Douglas J. LaBreque
Tucson, AZ 85721

1 Jim Wait
[redacted]

2 University of California
Engineering Geoscience Division
Attn: Frank Morrison
Alex Becker
567 Evans Hall, MS-1760
Berkeley, CA 94720

1 UC Berkeley
Dept. of Material Science and Mining Engineering
Attn: Michael Hoversten
577 Evans Hall
Berkeley, CA 94720

2 University of California
Earth Sciences Div. MS 50E 4237
Lawrence Berkeley National Laboratory
Attn: Ki Ha Lee
Louise Pellerin
1 Cyclotron Road
Berkeley, CA 94720

1 Electromagnetic Instruments Inc.
Attn: Edward Nichols
P.O. Box 463
El Cerrito, CA 94530-04631

2 Newmont Exploration Ltd.
Attn: Perry Eaton
Misac Nabigihian
1700 Lincoln St.
Denver, CO 80203

**Distribution (continued):**

1 Colorado School of Mines
Department of Geophysics
Attn: Gary Olhoeft
Golden, CO 80401-1887

4 Schlumberger Doll Research
Attn: Vladimir Druskin
Tarek Habashy, Michael Oristaglio
and Brian R. Spies
Old Quarry Road
Ridgefield, CT 06877-4108

2 Department of Energy
Office of Research and Development, NN-20
Attn: Michael O'Connell and Karl Veith
1000 Independence Ave. SW
Washington, D.C. 20585-0420

1 Idaho National Engineering Laboratory
LITCO
Attn: Cathy Pfeifer
P.O. Box 1625
Idaho Falls, ID 83415

1 US DOE Idaho Operations
Attn: George J. Schneider
785 DOE Place
MS 1119
Idaho Falls, ID 83402

1 University of Illinois
Dept. of Electrical and Computer Engineering
Electromagnetics Laboratory
Attn: Weng Chew
Urbana, IL 61801

1 US Environmental Protection Agency
Environmental Monitoring Systems Lab
Attn: Aldo T. Mazzella
Box 93478
Las Vegas, NV 89193-3478

**Distribution (continued):**

1 U.S. Department of Energy
Office of Energy Research
Attn: William C. Luth
ER-622
9901 Germantown Road
Germantown, MD 20874-1290

1 Earth Resources Laboratory
Department of Earth, Atmospheric and Planetary Sciences
Attn: Randall L. Mackie
42 Carelton Street
Cambridge, MA 02142

1 Geodynamics Research Institute
Texas A&M University
Attn: Mark E, Evertt
College Station, TX 77843-3114

1 Haliburton Energy Services Inc.
Attn: Mark Haugland
2135 Highway 6 South
Houston, TX 77077

1 Schlumberger LWD
Attn: John R. Lovell
200 Schlumberger Blvd. #110
Sugarland, TX 77478-3129

2 Western Atlas Inc.
Atlas Wireline Services
Attn: Kurt Strack
Lev Tabarovsky
P.O. Box 1407
Houston, TX 77251-1407

1 University of Utah
Dept. Geology and Geophysics
Attn: Michael Zhdanov
717 Browning Bldg.
Salt Lake City, UT 84112

**Distribution (continued):**

1 Stanley H. Ward
[redacted]

1 Noranda Technology Centre
Attn: John McGaughey
240 Hymus Blvd.
Point-Claire, Quebec
CANADA H9R 1G5

1 Department of Geophysics and Astronomy
University of British Columbia
Attn: Douglas W. Oldenburg
129-2219 Main Mall
Vancouver, B.C.,
CANADA V6T 1Z4

1 Ricardo Fernandez
Geodatos S.A.I.C
Roman Diaz Nx 773
Providencia
Santiago
Chile

1 Andreas Hoerdt
University of Cologne
Institute for Geophysics and Meteorology
Godesberger Str. 10
50968 Cologne
Germany

1 Mark Goldman
IPRG
P.O. Box 2286
Holon 58122
Israel

**Distribution (continued):**

1 Evert Slob
Delft University of Technology
Fac. of Mining and Petroleum Engineering
Section of Applied Geophysics
Mijnbouwstraat 120
2628 RX Delft
The Netherlands

MS 1111 Scott Hutchinson, 1421
MS 1111 John Shadid,1421
MS 1110 Lydie Prevost, 1422
MS 1110 Ray Tuminaro, 1422
MS 0828 Paul Hommert, 1503
MS 0533 Billy Brock, 2343
MS 0533 William Schaedla, 2343
MS 0865 Kimball Merewether, 2753
MS 0865 Larry Warne, 2753
MS 0701 Richard Lynch, 6100
MS 0705 Lew Bartel, 6114
MS 0705 Thurlow Caffey, 6114
MS 0483 Bob Glass, 6115
5 MS 0750 David L. Alumabugh, 6116
5 MS 0750 Gregory A. Newman, 6116
MS 0843 Daniel Cress, 9131
MS 1110 David Womble, 1422
MS 1166 Doug Riley, 9352

1 MS 9018 Central Technical Files, 8523-2,
5 MS 0899 Technical Library, 4414,
1 MS 0619 Print Media, 12615
2 MS 0100 Document Processing, 7613-2
For DOE/OSTI (2)